SYNTHESIS AND CHARACTERIZATION OF REUSABLE MAGNETIC TiO_2/CHITOSAN/Fe_3O_4 NANOCOMPOSITE FOR THE PHOTOCATALYTIC DEGRADATION OF ORTHO NITROPHENOL POLLUTANT

SABA AFZAL

INSTITUTE OF GRADUATE STUDIES
UNIVERSITY OF MALAYA
KUALA LUMPUR

2019

SYNTHESIS AND CHARACTERIZATION OF REUSABLE MAGNETIC TiO_2/CHITOSAN/Fe_3O_4 NANOCOMPOSITE FOR THE PHOTOCATALYTIC DEGRADATION OF ORTHO NITROPHENOL POLLUTANT

SABA AFZAL

THESIS SUBMITTED IN FULFILMENT OF THE REQUIREMENTS FOR THE DEGREE OF DOCTOR OF PHILOSOPHY

INSTITUTE OF GRADUATE STUDIES
UNIVERSITY OF MALAYA
KUALA LUMPUR

2019

UNIVERSITY OF MALAYA

ORIGINAL LITERARY WORK DECLARATION

Name of Candidate: Saba Afzal

Registration/Matric No: HHC140005

Name of Degree: Doctor of Philosophy

Title of Thesis ("this Work"): Synthesis and Characterization of Reusable Magnetic TiO_2/Chitosan/Fe_3O_4 Nanocomposite for the Photocatalytic Degradation of Ortho Nitrophenol Pollutant.

Field of Study: Chemistry

I do solemnly and sincerely declare that:

(1) I am the sole author/writer of this Work;
(2) This Work is original;
(3) Any use of any work in which copyright exists was done by way of fair dealing and for permitted purposes and any excerpt or extract from, or reference to or reproduction of any copyright work has been disclosed expressly and sufficiently and the title of the Work and its authorship have been acknowledged in this Work;
(4) I do not have any actual knowledge nor do I ought reasonably to know that the making of this work constitutes an infringement of any copyright work;
(5) I hereby assign all and every rights in the copyright to this Work to the University of Malaya ("UM"), who henceforth shall be owner of the copyright in this Work and that any reproduction or use in any form or by any means whatsoever is prohibited without the written consent of UM having been first had and obtained;
(6) I am fully aware that if in the course of making this Work I have infringed any copyright whether intentionally or otherwise, I may be subject to legal action or any other action as may be determined by UM.

Candidate's Signature Date:

Subscribed and solemnly declared before,

Witness's Signature Date:

Name:

Designation:

SYNTHESIS AND CHARACTERIZATION OF REUSABLE MAGNETIC TiO_2/CHITOSAN/Fe_3O_4 NANOCOMPOSITE FOR THE PHOTOCATALYTIC DEGRADATION OF ORTHO NITROPHENOL POLLUTANT

ABSTRACT

Designing a Titanium Oxide (TiO_2) nanoparticles based catalyst with improved photocatalytic activity in visible region of light with efficient recycling ability is desirable. As TiO_2 is one of the most attractive materials in nanotechnology due to its superior photo-catalytic oxidation ability, non-photo-corrosive and nontoxic nature. Despite of its excellent properties, the problems of rapid electron hole pair recombination, wide band gap and poor catalyst reusability narrows the applications of TiO_2 nano particles. The present research aims to synthesize titanium dioxide-chitosan-magnetite (TiO_2/CS/Fe_3O_4) nano composite with enhanced adsorption characteristics, minimize electron hole pair recombination of TiO_2, improves activity in visible region of light and efficient recycling of catalyst after wastewater treatment. CS is an excellent adsorbent with functional groups (NH_2, OH) which are responsible of adsorbing organic pollutants. It served as a linker between TiO_2 and Fe_3O_4 to facilitate the overall photocatalysis. Recycling of TiO_2 by using traditional methods produce secondary pollutants to the environment, however, separation techniques by applying magnetic adsorbent are an alternative way. Fe_3O_4 nano particles are useful in biological and environmental applications because of their large surface area, nano size dimension and strong response to external magnetic field. Thus, Fe_3O_4 give efficient separation of catalyst after wastewater treatment. Presence of Fe_3O_4 shows significant reduction in the band gap of TiO_2 (from 3.19 eV to 2.85 eV) which shifts the photoactivity of composite in visible region. Fe_3O_4/CS core was synthesized by Co-precipitation as it is a simple and an economical method give well dispersed Fe_3O_4 nano particles with the success rate from 96 to 99.9%. Effect of concentration of each individual component (TiO_2, CS and Fe_3O_4) on the physicochemical and photocatalytic properties of TiO_2/CS/Fe_3O_4

(TCF) nancomposite has been studied. The effectiveness of the optimize TCF nanocomposite was then be assessed using ortho-nitrophenol (ONP) which is considered as the most toxic and persistent organic pollutant (POP) of industrial wastewater. By using 0.02 g of optimized TCF nanocomposite >90% degradation of ONP was achieved within 180 minutes in visible region. The percent photodegradation of ONP was studied by using UV-vis spectrophotometer while the degradation pathway of ONP was studied by using liquid chromatography mass spectroscopy (LC-MS). The superior photocatalytic performance of ternary system (TiO_2/CS/Fe_3O_4) along with the advantage of easy recoverability could make it a new appealing catalyst for wastewater treatment applications.

Keywords: Photocatalysis, nanocomposite, band gap engineering, magnetic separation, Wastewater

SINTESIS DAN PENCIRIAN MAGNETIK NANOKOMPOSIT TiO_2/CS/Fe_3O_4 UNTUK PEMEROSOTAN CAHAYA NITROPHENOL PENCEMAR

ABSTRAK

Merekabentuk pemangkin berasaskan nanopartikel titanium dioksida (TiO_2) yang mempunyai aktiviti foto pemangkinan yang lebih baik di dalam spektrum cahaya boleh dilihat dengan keupayaan kitaran semula yang cekap adalah wajar memandangkan TiO_2 adalah salah satu bahan yang paling menarik dalam bidang nanoteknologi berdasarkan keupayaan pengoksidaan foto pemangkinnya yang unggul, dengan sifat bukan foto-menghakis dan bukan toksik. Disebalik sifat-sifat ini,, masalah penggabungan pesat pasangan elektron dan lubang, jurang jalur yang lebar dan kadar kegunaan semula pemangkin yang buruk menyebabkan penggunaannya yang terhad. Projek ini bertujuan untuk mensintesis komposit nano titanium dioksida-chitosan-magnetit (TiO_2/CS/Fe_3O_4) dengan ciri-ciri penjerapan yang lebih baik, meminimumkan penggabungan pasangan elektron dan lubang, meningkatkan aktiviti di dalam spektrum cahaya yang boleh dilihat dan

kadar kitaran semula pemangkin yang berkesan selepas proses rawatan air kumbahan. CS adalah bahan penjerapan unggul yang memiliki kumpulan berfungsi (NH_2, OH) yang bertanggungjawab atas penyerapan bahan pencemar organik. Kumpulan tersebut bertindak sebagai penghubung antara TiO_2 dan Fe_3O_4 untuk memudahkan proses keseluruhan fotopemangkinan. Kadar kitaran semula TiO_2 yang menggunakan cara tradisional menghasilkan pencemaran sekunder, namun, teknik pemisahan menggunakan penyerap magnet adalah cara alternatif. Nanopartikel Fe_3O_4 adalah sangat berguna dalam aplikasi biologi dan alam sekitar kerana mempunyai kawasan permukaannya yang luas, dimensi ukuran bersaiz nano dan tindak balas yang tinggi terhadap medan magnet luar. Oleh itu, Fe_3O_4 memberikan pemisahan pemangkin yang berkesan selepas rawatan air kumbahan. Kehadiran Fe_3O_4 menunjukkan penyempitan yang ketara dalam jurang jalur TiO_2 (dari 3.19 eV hingga 2.85 eV) yang mengalihkan

aktivi foto pemangkinan ke arah spektrum cahaya . Teras Fe_3O_4/CS disintesis dengan kaedah pemendakan bersama kerana ia adalah kaedah yang mudah dan ekonomik. Kaedah ini memberikan kadar penyebaran baik nanopartikel Fe_3O_4 dengan kadar kejayaan 96 hingga 99.9%. Kesan kepekatan setiap komponen individu (TiO_2, CS dan Fe_3O_4) terhadap sifat fizikokimia dan aktivi foto pemangkinan komposit nano TiO_2/CS/ Fe_3O_4 (TCF) telah dikaji. Kadar keberkesanan komposit nano TCF yang optimum kemudiannya akan dinilai menggunakan kaedah ortho-nitrophenol (ONP) yang dianggap sebagai bahan pencemar organik (POP) yang paling toksik dan sukar untuk diatasi dalam industri rawatan air. Dengan menggunakan 0.02 g komposit nano TCF, lebih dari 90% degradasi ONP dicapai dalam tempoh 180 minit dalam spektrum cahaya boleh dilihat. Peratusan fotodegradasi ONP telah dikaji dengan menggunakan spektrofotometer UV-vis manakala mekanisma pemerosotan ONP dikaji dengan menggunakan liquid chromatography mass spectroscopy (LC-MS). Prestasi aktiviti foto pemangkin yang lebih baik oleh sistem gabungan (TiO_2/CS/Fe_3O_4) dan kelebihan mudah pulih sistem ini boleh menjadikannya sebagai pemangkin menarik baru untuk aplikasi rawatan air kumbahan.

Kata kunci : Fotokatalis, nanocomposite, kejuruteraan jurang band, pemisahan, magnetik, air kumbahan

ACKNOWLEDGEMENT

All praises to be Allah who has given me opportunity and strength to fulfill this challenging journey of PhD. I would like to express my sincere gratitude to my supervisors Dr. Nurhidayatullaili Mohd Jalkupli and late Prof. Sharifah Bee Abd Hamid for their guidance, encouragement and valuable discussion throughout my work. I gained a lot of research experience such as laboratory techniques, scientific thinking and writing under their mentorship.

I would also like to express my deepest regards to Dr. Lee Kian Mun for his constant support throughout my work. I really respect and appreciate your guidance. I would also like to thank all the NANOCAT staff for their assistance.

I am also indebted to my laboratory colleagues especially Dr. Emy marlina, Nur Iman Amir and Ahmed Khalil for their valuable discussion and emotional support. I am also grateful to all my friends specially Dr. Munazza Saeed, Dr. Anam Asghar, Dr. Rabia Naeem and Dr. Bibi Sherino for their help and encouragement throughout my studies.

I would like to acknowledge the University Malaya Research Grant (UMRGA), IPPP (PG074-2014B) and Higher Education Commission of Pakistan (HEC) for their financial support. I am really thankful to the staff and officials of Sardar Bahadur Khan Women's University, Quetta for considering me for this scholarship and their continuous support.

Most importantly, none of this would have been possible without the love and patience of my family particularly my husband Ahmed Zeeshan. Your love and support is the source of strength which has never let me loose courage throughout this period. I would also like to express my heartfelt gratitude to my parents whose unconditional love, constant concern and prayers make me able to fulfill this degree.

TABLE OF CONTENTS

Abstract iii

Abstrak v

Acknowledgment vii

Table of Contents viii

List of Figures xiv

List of Tables xviii

List of Symbols and Abbreviation xx

List of Appendices xxiii

CHAPTER 1: INTRODUCTION 1

1.1 Global Wastewater scenario 1

1.2 Phenolic compounds as persistent organic pollutants (POP's) 2

1.2.1 Nitrophenol 3

1.3 Current Water treatment technologies 4

1.3.1 Semiconductor TiO_2 photocatalysis 5

1.4 Problem statement 5

1.5 Research Objective 6

1.5.1 Specific objectives 6

1.6 Strategies to modify the physico-chemical and photocatalytic properties of TiO_2 7

1.6.1 Magnetic TiO_2 photocatalyst 7

1.7 Scope of research 8

1.8 Research Novelty 9

1.9 Thesis organization 9

CHAPTER 2: LITERATURE REVIEW 12

2.1 Photocatalysis 12

2.1.1 Mechanism of photocatalysis 13

2.2 Semiconductor photocatalyst 15

2.2.1 TiO_2 15

2.2.2 Applications of TiO_2 15

2.2.3 Other Semiconductors 16

2.2.4 Limitations of TiO_2 17

2.3 Strategies to overcome limitations of TiO_2 19

2.3.1 Doping 19

2.3.2 Dye sensitization 22

2.3.3 Composites 24

2.4 Magnetite nanoparticles 25

2.4.1 Methods for the synthesis of Fe_3O_4 nanoparticles 27

2.4.1.1 Microemulsion 27

2.4.1.2 Thermal decomposition 28

2.4.1.3 Hydrothermal 29

2.4.1.4 Sol gel 30

2.4.1.5 Co-precipitation 30

2.5 TiO_2/Fe_3O_4 nanocomposite system 32

2.5.1 Fe_3O_4 with support as passive layer 34

2.5.1.1 Silica (SiO_2) 34

2.5.1.2 Carbon 35

2.5.1.3 Graphene 36

2.5.1.4 Chitosan (CS) 37

2.6 Applications of TiO_2 based composites in wastewater treatment 40

2.6.1 Persistent organic pollutant (POP's) 41

2.6.1.1 Nitrophenol 42

2.7 Effects of operating parameters on degradation rate 45
2.7.1 Catalyst loading 45
2.7.2 Initial concentration of pollutant 46
2.7.3 pH of reaction medium 46
2.7.4 Light Intensity 47
2.7.5 Effect of oxidants 47
2.7.6 Effect of temperature 48
2.8 Summary of Literature review 49

CHAPTER 3: METHODOLOGY 51

3.1 Materials 53
3.2 Synthesis of TiO_2/CS/Fe_3O_4 nanocomposite 53
3.2.1 Synthesis of Fe_3O_4/CS 53
3.2.2 Synthesis procedure for TiO_2/CS/Fe_3O_4 54
3.2.3 Synthesis of TiO_2/CS/Fe_3O_4 on varying concentration of TiO_2, CS and Fe_3O_4 54
3.3 Characterization techniques 55
3.3.1 Field emission scanning electron microscopy (FESEM) 56
3.3.2 Energy dispersive x-ray spectroscopy (EDX) 56
3.3.3 High resolution transmission electron microscopy (HR-TEM) 57
3.3.4 Brunner-Emmet-Teller (BET) 57
3.3.5 X-Ray powder diffraction (XRD) 58
3.3.6 Vibrating-sample magnetometer (VSM) 59
3.3.7 Fourier transform infrared (FTIR) spectroscopy 59
3.3.8 Photoluminescence spectroscopy (PL) 60
3.3.9 UV-vis Diffuse reflectance spectroscopy (UV-vis DRS) 60
3.3.10 X-ray photoelectron spectroscopy (XPS) 61

3.4 Photocatalytic degradation experiments 62
3.4.1 Reactor setup and photocatalytic activity test 62
3.4.2 Response surface methodology (RSM) and experimental design 63
3.5 Chemical Analysis 64
3.5.1 pH Adjustment 64
3.5.2 ONP degradation analysis 64
3.6 Reaction Kinetics 66
3.7 Catalyst Reusability study 66
3.8 Mechanistic studies 66
3.9 Total Organic Carbon (TOC) Analysis 67

CHAPTER 4: RESULTS AND DISCUSSION 68
4.1 Synthesis of TiO2/CS /Fe3O4 68
4.1.1 Morphological and textural properties 68
4.1.2 Crystal properties 73
4.1.3 Magnetic properties 75
4.1.4 Chemical composition 76
4.1.5 Optical properties 79
4.1.6 Surface chemical state 83
4.2 Photocatalytic activity on the degradation of ONP 86
4.3 TCF nanocomposite under varying concentrations (TiO_2, CS, Fe_3O_4) 87
4.3.1 Effect of TiO_2 content 87
4.3.1.1 Morphology 87
4.3.1.2 Crystal properties 89
4.3.1.3 Magnetic properties 90
4.3.1.4 Chemical composition 91
4.3.1.5 Optical properties 93

4.3.1.6 Photocatalytic degradation of ONP 96
4.3.2 Effect of CS loading 99
4.3.2.1 Morphology 99
4.3.2.2 Crystal properties 100
4.3.2.3 Magnetic properties 102
4.3.2.4 Chemical composition 103
4.3.2.5 Optical properties 104
4.3.2.6 Photocatalytic degradation of ONP 106
4.3.3 Effect of Fe3O4 concentration 108
4.3.3.1 Morphology 108
4.3.3.2 Crystal properties 110
4.3.3.3 Magnetic properties 111
4.3.3.4 Chemical composition 112
4.3.3.5 Optical properties 114
4.3.3.6 Photocatalytic degradation of ONP 116
4.4 Effect of operating parameters on photocatalytic degradation of ONP 118
4.5 Model results for photocatalytic degradation of ONP 120
4.5.1 Model fitting and analysis of variance (ANOVA) 120
4.6 Response surface and 3D contour plots for the photocatalytic degradation of ONP 123
4.6.1 Effect of catalyst loading 123
4.6.2 Effect of initial ONP concentration 124
4.6.3 Effect of pH 126
4.7 Confirmation studies 129
4.8 Reusability of TCF nanocomposite 130
4.9 Photocatalytic degradation intermediates and degradation pathway of ONP 132

4.10 Mineralization of ONP 136

CHAPTER 5: CONCLUSION ANS FUTURE RECOMMENDATIONS 137

5.1 Conclusion 137

5.2 Suggestions and Recommendations 139

5.3 Significance of Research 140

References 141

List of Publications and Paper Presented 159

Appendices 160

LIST OF FIGURES

Figure 1.1: Fresh water withdrawal, consumption and wastewater production globally 2

Figure 1.2: Molecular structure of O-nitrophenol, $C_6H_5O_3N$ 4

Figure 2.1: Advantages of photocatalysis 13

Figure 2.2: Basic mechanism of photocatalysis on the surface of semiconductor..... 14

Figure 2.3: Applications of TiO_2 photocatalysis. 16

Figure 2.4: Limitation of TiO_2 in application of photocatalytic degradation reactions. . 18

Figure 2.5: Proposed photocatalytic degradation mechanism by cationic dopant on TiO_2 surface 20

Figure 2.6: Photocatalytic degradation mechanism by Anionic dopant on TiO_2 surface. 21

Figure 2.7: Mechanism of dye sensitization on the surface of TiO_2 23

Figure 2.8 : The band structure of a composite photocatalyst, prepared by a mixture of narrow and wide band gap photocatalysts 25

Figure 2.9: Schematic diagram of photoinduced charge transfer for TiO_2 (a) without intermediate layer and (b) with intermediate layer. 33

Figure 2.10: Structure of Chitosan. 37

Figure 2.11: Persistent organic pollutant with their distinctive features..... 41

Figure 3.1: An overview of research work..... 52

Figure 3.2: Synthesis of TiO_2/CS/Fe_3O_4 nanocomposite..... 55

Figure 3.3: Schematic diagram for photocatalytic reactor setup..... 62

Figure 3.4: Flow chart for central composite design 65

Figure 4.1: High magnification FESEM images of (a) TiO_2 (b) Fe_3O_4 (c) Fe_3O_4/CS and (d) TCF2 nanocomposite..... 69

Figure 4.2: (a) Elemental mapping and (b) EDX spectrum and composition of TCF2 nanocomposite..... 70

Figure 4.3: HRTEM images of (a) TiO_2 and (c) TCF2 nanocomposite. Lattice fringes

and the assessed d-spacing of (b) TiO_2 and (d) TiO_2 and Fe_3O_4 in TCF2 nanocomposite 71

Figure 4.4: Nitrogen adsorption-desorption linear isotherm plot of (a) TiO_2 (b) Fe_3O_4 (c) Fe_3O_4/CS and (d) TiO_2/CS/Fe_3O_4 73

Figure 4.5: XRD patterns of (a) TiO_2 (b) Fe_3O_4 (c) Fe_3O_4/CS and (d) TCF2 74

Figure 4.6: VSM curves of (a) Fe_3O_4, (b) Fe_3O_4/CS and (c) TCF2 nanocomposite 76

Figure 4.7: FTIR spectra of (a) TiO_2, (b) Fe_3O_4, (c) Fe_3O_4/CS and (d) TCF2 nanocomposite 78

Figure 4.8: PL spectrum of (a) TiO2 and (b) TCF2 nanocomposite 80

Figure 4.9: Full range absorption spectrum and calculated band gap (inset) of (a) TiO_2 and (b) Fe_3O_4, (c) Fe_3O_4/CS and (d) TCF2 composite 82

Figure 4.10: XPS spectrum of (a) survey spectra of TiO_2/CS/Fe_3O_4 nanocomposite and narrow scan of TiO_2/CS/Fe_3O_4 (b) Ti 2p, (c) O1s, (d) Fe 2p3, (e) N1s. 85

Figure 4.11: Degradation of ONP under (a) pure visible light, (b) Fe_3O_4 (c) Fe_3O_4/CS (d) TiO_2 and (e) TCF2 nanocomposite 87

Figure 4.12: FESEM images of TCF nanocomposite on varying concentrations of TiO_2 88

Figure 4.13: Elemental mapping of (a) TCF-T1 and (b) TCF-T3 89

Figure 4.14: XRD spectra of (a) TCF-T1, (b) TCF2 and (c) TCF-T3 nanocomposite ... 90

Figure 4.15: VSM spectra showing (a) TCF-T1 (b) TCF2 and (c) TCF-T3 nanocomposite 91

Figure 4.16: FTIR spectra of (a) TCF-T1 (b) TCF2 and (c) TCF-T3 nanocomposites .. 92

Figure 4.17: PL spectra showing effect of concentration of TiO_2 on optical properties and respective e+- h- recombination of nanocomposites 94

Figure 4.18: UV absorption spectra and calculated band gap of (a) TCF-T1 and (b) TCF-T3 95

Figure 4.19: Photocatalytic activity of TCF nanocomposites for ONP degradation on different concentration of TiO_2 97

Figure 4.20: First order kinetics for composite samples synthesized on varying TiO2 concentration on the degradation of ONP 98

Figure 4.21: FESEM imanges of TCF nanocomposite on varying CS loading (a) TCF-C1 and (b) TCF-C3 99

Figure 4.22: Elemental mapping of (a) TCF-C1 and (b) TCF-C3 100

Figure 4.23: XRD spectra of (a)TCF-C1 (b) TCF2 and (c) TCF-C3 101

Figure 4.24: VSM spectra of (a) TCF-C1 (b) TCF2 and (c) TCF-C3 102

Figure 4.25: FTIR spectra showing effect of (a) TCF-C1, (b) TCF2 and (c) TCF-C3 . 103

Figure 4.26: PL spectra showing effect of concentration of CS on optical properties and respective e+-h- recombination of resultant nanocomposites 105

Figure 4.27: UV absorption spectra and calculated band gap of (a) TCF-C1 and (b) TCF-C3 106

Figure 4.28: Photocatalytic activity of composite samples synthesized on varying CS concentration for ONP degradation 107

Figure 4.29: First order kinetics for composite samples synthesized on varying CS concentration on the degradation of ONP 108

Figure 4.30: FESEM images of TCF nanocomposite on varying Fe_3O_4 concentration (a) TCF-F1 and (b) TCF-F3 109

Figure 4.31: Elemental mapping of (a) TCF-F1 and (b) TCF-F3 110

Figure 4.32: XRD spectra of (a) TCF-F1 (b) TCF2 and (c) TCF-F3 111

Figure 4.33: VSM spectra of (a) TCF-F1 (b) TCF2 and (c) TCF-F3 112

Figure 4.34: FTIR spectra of (a) TCF-F1 (b) TCF2 and (c) TCF-F3 113

Figure 4.35: PL spectra showing effect of concentration of Fe_3O_4 on optical properties and respective e+-h- recombination of resultant nanocomposites 115

Figure 4.36: UV absorption spectra and calculated band gap of (a) TCF-F1 and (b) CF-F3 116

Figure 4.37: Photocatalytic activity of composites samples synthesized on varying concentration of Fe_3O_4 for ONP degradation 117

Figure 4.38: First order kinetics for the degradation of ONP by TCF nanocomposites synthesized on different concentrations of Fe_3O_4 118

Figure 4.39: Predicted Vs Actual values for ONP degradation by TCF2 121

Figure 4.40: (a) 2D and (b) 3D contours for the degradation of ONP showing combined effects of catalyst (TCF2) loading and ONP concentration 125

Figure 4.41: (a,c) 2D and (b,d) 3D contours for the degradation of ONP showing combined effects of catalyst (TCF2) loading and ONP concentration on pH respectively. 128

Figure 4.42: Perturbation plot for ONP degradation (a) catalyst loading, (b) ONP concentration and (c) pH 129

Figure 4.43: Reusability data over TCF2 nano composite in degradation of ONP in visible light. 131

Figure 4.44: Schematic illustration of photocatalytic degradation of ONP by TiO_2/CS/Fe_3O_4 core-shell nanocomposite under visible light. 132

Figure 4.45: (a) 3-nitrocatechol (b) nitrohydroquinone 134

Figure 4.46: Proposed degradation pathway of ONP. Dotted arrows show undefined pathways. 135

Figure 4.47: Percentage removal of TOC of ONP by TCF2 nanocomposite. 136

LIST OF TABLES

Table 2.1: Basic principle of photocatalysis and radical formation 14

Table 2.2: Dye sensitize TiO_2 for photocatalytic degradation of pollutants 23

Table 2.3: Summary of comparison of synthesis methods to produce Fe_3O_4 nanoparticles 32

Table 2.4: CS based materials for the degradation of dyes (Nithya et al., 2014) 38

Table 2.5: Different coating Molecules/polymers to stabilize Fe_3O_4 NP's 39

Table 2.6: Applications of TiO_2 with various support system for the degradation of textile dyes and organic pollutants 40

Table 2.7: The type of POP's and their sources 42

Table 2.8: Photocatalytic treatment of NP's using TiO_2 and TiO_2 based composites 44

Table 3.1: The amount of chemicals required during synthesis of nanocomposite 55

Table 3.2: Operational parameter and experimental ranges for ONP degradation 64

Table 4.1: Crystallite size, BET surface area, pore volume and average pore width of Fe3O4/CS and core-shell TiO_2/CS/Fe_3O_4 nanocomposite 73

Table 4.2: Magnetic properties of Fe_3O_4, Fe_3O_4/CS and TiO_2/CS/Fe_3O_4 nanocomposite 76

Table 4.3: EDX elemental composition (weight %) of Ti, O, C and Fe in TCF nanocomposites 88

Table 4.4: Average crystallite size of TCF nanocomposites on varying concentration of TiO_2, CS and Fe_3O_4 90

Table 4.5: Saturation magnetization, coercivity and magnetic remanence of all the synthesized nanocomposites 91

Table 4.6: Rate constants for the degradation of ONP by composite samples synthesized on varying TiO_2 concentration 98

Table 4.7: EDX elemental composition (weight %) of Ti, O, C and Fe in TCF nanocomposites 100

Table 4.8: Average crystallite size of TCF nanocomposites on varying concentration of CS 101

Table 4.9: Saturation magnetization, coercivity and magnetic remanence of composite samples synthesized on varying CS concentration 102

Table 4.10: Rate constants for the degradation of ONP by composite samples synthesized on varying CS concentration 108

Table 4.11: EDX elemental composition (weight %) of Ti, O, C and Fe in composite sample synthesized on varying Fe_3O_4 concentration 109

Table 4.12: Average crystallite size of TCF nanocomposites on varying concentration of Fe_3O_4 111

Table 4.13: Saturation magnetization, coercivity and magnetic remanence of composite samples synthesized on varying Fe_3O_4 concentration..... 112

Table 4.14: Rate constants for the degradation of ONP by TCF nanocomposites synthesized on different concentrations of Fe_3O_4 118

Table 4.15: Experimental ranges and levels of independent variables for photocatalytic degradation of ONP..... 119

Table 4.16: Experimental design matrix and location of points on CCD surface..... 119

Table 4.17: Central composite design with predictive values and experimental results 121

Table 4.18: Analysis of variance (ANOVA) for derived quadratic model 123

Table 4.19: Experimental values for model verification conducted at predicted conditions from CCD 130

Table 4.20: Possible photocatalytic degradation intermediate products of ONP..... 134

LIST OF SYMBOLS AND ABBREVIATIONS

POP's	:	Persistent organic pollutant
UN	:	United nation
FAO	:	Food and agriculture organization of the United Nations
USEPA	:	United State Environmental Protection Agency
NPs	:	Nitro phenols
ppb	:	Parts per billion
ONP	:	Ortho-nitro phenol
AOT	:	Advanced oxidation technologies
VB	:	Valence band
CB	:	Conduction band
$e^- – h^+$	:	electron-hole
$OH^\bullet$	:	Hydroxyl radical
FESEM	:	Field Emission Scanning Electron Microscopy
HR-TEM	:	High Resolution Transmission Electron Microscopy
BET	:	Brunauer–Emmett–Teller
XRD	:	X-ray Diffraction
VSM	:	Vibrating Sample Magnetometer
PL	:	Photoluminescence
UV-DR	:	UV-vis Diffuse Reflectance spectroscopy
FTIR	:	Fourier Transform Infra-red spectroscopy
XPS	:	X-ray photoelectron spectroscopy
CS	:	Chitosan

TOC	:	Total Organic Carbon
LC-MS	:	Liquid chromatography mass spectroscopy
COD	:	Chemical oxygen demand
$^{\cdot}OOH$	:	Hydroperoxyl radical
$O_2^{\bullet-}$	:	Superoxide anion
H_2O_2	:	Hydrogen peroxide
HOMO	:	Highest occupied molecular orbital
LUMO	:	Lowest unoccupied molecular orbital
Rhodamine B	:	RhB
Methylene blue	:	MB
Magnetic resonance imaging	:	MRI
nm	:	nanometer
MPa	:	Megapascal
SiO_2	:	Silica
AC	:	Activated carbon
TMAC	:	TiO_2 coated magnetic activated carbon
GO	:	Graphene oxide
PEG	:	Polyethylene glycol
PVA	:	Polyvinyl alcohol
PCB's	:	Polychlorinated biphenyles
HCH	:	Hexachlorocyclohexans
EDTA	:	Ethylenediaminetetraacetic acid
RSM	:	Response surface methodology

CCD	:	Central composite design
TCF	:	TiO_2/Chitosan/magnetite
JCPDS	:	Joint Committee for Powder Diffraction Standards
FWHM	:	Full width at half maximum
LED	:	Light emitting diode
ppm	:	Parts per million
EDX	:	Energy-dispersive X-ray spectroscopy
Ms	:	Saturation magnetization
kOe	:	Kilooersted
Hci	:	Coercivity
Mr	:	Magnetic remanence
eV	:	Electron volt
ANOVA	:	Analysis of variance
C.V	:	Coefficient of variation
2D	:	2 dimensional
3D	:	3 dimensional
IEP	:	Isoelectric point
PZC	:	Point of zero charge
IM	:	Intermediate product
WWDR	:	World Water Development Report

LIST OF APPENDICES

Appendix A: Kinetics of ONP degradation 160

Appendix B: Rate constant for ONP degradation 161

Appendix C: XRD pattern of recycled TCF2 nanocomposites……..... 162

Appendix D: LCMS chromatograms 163

CHAPTER 1: INTRODUCTION

This chapter delivers a concise introduction of nitro phenols as POP's in wastewater and the role of semiconductor TiO_2 catalysis in their removal. The current limitations of TiO_2 and strategies to improve its performance, in which the research topic is concerned, are detailed.

1.1 Global Wastewater scenario

The quality of water resources is declining continuously due to rapid industrialization, agricultural activities, population growth, and other environmental changes. This has become a serious source of concern globally. Numerous organic, inorganic, and biological pollutants are found in the environment. These pollutants are not only hazardous for the aquatic environment, but also for the whole ecosystem of the Earth (Ali, 2012). Progress in industrialization and agriculture has led to the disposal of many toxic pollutants in water bodies, which are difficult to be degraded by natural means. It is estimated that in developing countries, about 70% of industrial wastes are discharge without any treatment, which consequently contaminate existing water supplies (Qureshi et al., 2015). High discharges of inadequately treated wastewater cause further degradation of surface and groundwater water quality. The approximate wastewater production per year is about 1,500 km^3 according to UN (United Nations). This is about six times more than the water that exists in all the rivers of the world. Globally, around 4 billion people have little or no access to sanitized water supply, and about 5 million people died annually due to severe waterborne diseases. These statistical figures are expected to rise in the near future, due to increasing water pollution by overwhelming discharge of contaminants into the natural water cycle (Qureshi etal., 2015; Chong et al., 2010). The FAO'S AQUASTAT database estimates the annual withdrawal of fresh water globally and the release of wastewater as industrial effluents, municipal and

agricultural drainage water (Figure 1.1). Thus, the subject of wastewater needs to be properly managed as it critically affects the availability of water.

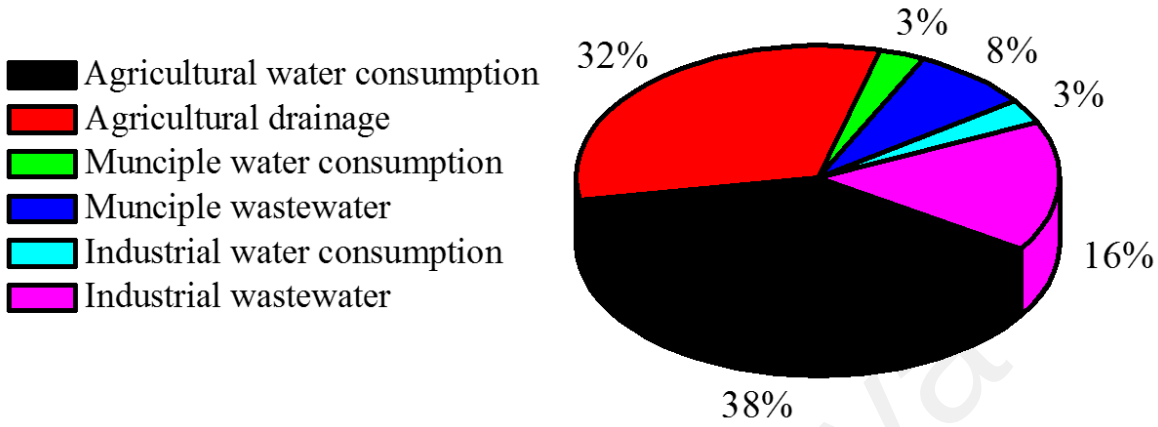

Figure 1.1: Fresh water withdrawal, consumption and wastewater production globally (WWDR, 2017)

1.2 Phenolic compounds as persistent organic pollutants (POP's)

Among the wastewater pollutants, phenols and their derivatives are the most resistant class of potential pollutants (Aslam et al., 2015). Their presence in the aquatic environment is due to their extensive use in various industrial processes such as wood processing, manufacture of plastics, drugs, antioxidants, dyes, petrochemical and petroleum refineries, polymer product, coal, cooking, pharmaceuticals and pesticides (Shirsath & Shrivastava, 2015; Shamar, 2013). Phenolic compounds are used as antiseptics and in pesticides since they can be toxic to many bacterial species (Stefanakis & Thullner, 2016). Phenol substituted compounds include halogenated (e.g., chlorophenol), ether (e.g, methoxyphenol) and nitrated (e.g., 2-nitrophenol) (Shamar, 2013). The toxicity of these derivatives is dependent on the number of atoms and their position with respect to the hydroxyl group (Aslam et al., 2015). Over the past decades, the industrial uses of phenolic derivatives have resulted in severe environmental pollution. Furthermore, about 190 tons of phenolic waste is disposed monthly, mainly by polymer, pharmaceuticals, and petrochemicals industries (Shokri, 2015).

Phenolic compounds can cause adverse health effects, including irregular breathing, skin and eye irritation, and muscle weakness. However, chronic exposure at higher concentrations poses even greater effects. They are considered as priority pollutants according to the United State Environmental Protection Agency (USEPA), and are characterized as toxic, carcinogenic, mutagenic, and teratogenic compounds. Their persistence and accumulation in the environment are threatening to human health and the entire ecosystems (Stefanakis & Thullner, 2016).

1.2.1 Nitrophenol

Nitrophenols (NPs) are phenolic derivatives which are the most common toxic persistent pollutants in agricultural and industrial wastewater (Nie et al., 2016). NPs are anthropogenic (Shokri, 2015) and formed during production and degradation of pesticides such as 4,6-dinitro-2-methylphenol (DNoc) and 2-buthyl-4,6-dinitrophenol (Dinoseb). These compounds are also used as components and precursors for the production of drugs and polymers, solvents, dyes, explosives and employed as preservatives and photographic developers (Michałowicz & Duda, 2007). Therefore, their release as industrial waste introduced them as water pollutants (Shokri, 2015).

The high solubility and stability of NPs in water make them of serious concern to the environment. Their treatment becomes even more difficult due to their resistance towards traditional techniques (Jinzhang et al., 2004). They are carcinogenic, highly toxic and display mutagenic effects and are notified as priority pollutants by the USEPA (Assi et al., 2015; Yuan et al., 2008). Thus, their maximum permitted concentrations in water ranged from 1 to 20 ppb (Kavitha & Palanivelu, 2005).

Among these derivatives, those substituted at the ortho position (Figure 1.2) of aromatic ring (e.g, O-nitrophenol) are stabilized additionally by intra-molecular hydrogen bonding (Aslam et al., 2015). O-Nitro phenol (ONP) have several biochemical and

morphological effects on plants and animals (Shirsath, & Shrivastava, 2015). Water polluted with ONP is difficult to purify, as the nitro (NO_2) group on the aromatic ring enhances the stability of the nitrophenolic compounds to chemical and biological degradation (Nie et al., 2016).

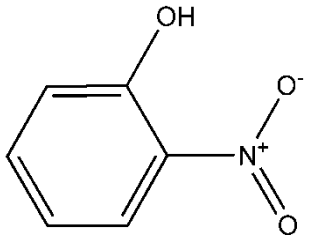

Figure 1.2: Molecular structure of O-nitrophenol, $C_6H_5O_3N$

The USEPA restrict their limit in natural waters to less than 4.8 µg/ L (Ammar et al., 2007). The maximum concentration of ONP reported in densely populated and highly industrialized Malaysian Klang river basin in 1990 and 1991 was 7.2 µg/L (Tan & Chong, 1993).

1.3 Current Water treatment technologies

To overcome the shortage of clean water, development of highly efficient, advanced and low-cost wastewater treatment technologies is desirable (Chong et al., 2010). Conventional methods for the treatment of NPs are physico-chemical processes (e.g. nano-filtration, activated carbon adsorption, and coagulation–flocculation) and biological oxidation. Physico-chemical processes only transform the contaminant from one phase to another and thus, additional treatments are necessary for the secondary wastes (Zhao et al., 2010). On the other hand, degradation by biological processes requires long incubation time since the nitro-group confers chemical stability and resistance to the aromatic compound towards microbial degradation (Yuan et al., 2008). Consequently, a more promising technology is heterogeneous photocatalysis: a discipline which contains a large variety of reactions including water detoxification and

gaseous pollutant removal. Therefore, it can be considered as one of the new advanced oxidation technologies (AOT) for air and water purification (Herrmann, 1999). Photocatalytic reactions employing semiconductor catalyst (TiO_2, ZnO, Fe_2O_3, CdS, ZnS) have been shown to be potentially advantageous and useful in the treatment of wastewater as it allows the complete mineralization of pollutant (Dai et al., 2014; Chong et al., 2010; Paola et al., 2003).

1.3.1 Semiconductor TiO_2 photocatalysis

Amongst various semiconductor materials used in photocatalysis, titanium dioxide (TiO_2) is the most widely used due to its high activity, chemical stability, low pollution load, non-toxicity and availability at low cost (Dai et al, 2014; Zhao et al., 2010). TiO_2 has attracted significant interests in various environmental applications, including sunscreen, coating industry, micromechanical, and electro-optical and sensor devices (Ananpattarachai et al., 2016; Lim et al., 2010). They are also utilized for the removal of variety of organic water pollutants. When TiO_2 is irradiated with light of wavelength λ = 390 nm, an electron from valence band (VB) jumps to the conduction band (CB), leaving behind a hole. These electron–hole pairs ($e^- – h^+$) further produce highly active $OH^\bullet$ which can oxidize organic pollutants (Nevim San & glu, 2002).

1.4 Problem statement

The critical issues which limit the practical applications of nanoTiO_2 are fast charge carrier recombination rate, wide band gap (3.2 eV), (Hameed., et al., 2015; Zhao et al., 2010), poor affinity towards hydrophobic pollutants and difficulty in recovery after the wastewater treatment (Kalan et al., 2016; Dong et al., 2015). Films of TiO_2 have also been used on glass, paper, and tile to negate its post-treatment limitation. However, as their surface area is much smaller than that of particles, a low photocatalytic activity is

expected in the former (Marbán et al., 2014; Cheng et al., 2012). There are several reports on the removal of ONP including the use of αBi_2O_3 (Hameed et al., 2015), ZnO (Assi et al., 2015), V_2O_5 (Aslam et al., 2015), CoO/CoS (Pouretedal & Kiyani, 2014), TiO_2-ionic liquid (Dai et al., 2014), Copper oxide Alumina (Atta et al., 2012), and TiO_2-P25 (Di Paola et al., 2003). However, the common disadvantage of using these catalytic systems is their recovery after treatment.

Hence, there is a necessity to design a solar driven photocatalyst that possesses superior adsorption for organic contaminants and efficient recycling properties with enhance photodegradation activity.

1.5 Research Objective

The general objectives of the research are as follows:

I. To design and synthesize $TiO_2/CS/Fe_3O_4$ nanocomposite with efficient e^-– h^+ separation and recycling properties.

II. To evaluate the performance of $TiO_2/CS/Fe_3O_4$ for POP's degradation under visible light.

1.5.1 Specific objectives

I. To synthesize and characterize Fe_3O_4/CS by co-precipitation method and the ternary $TiO_2/CS/Fe_3O_4$ nano composite.

II. To prepare six more $TiO_2/CS/Fe_3O_4$ nanocomposite by varying concentration of TiO_2, CS and Fe_3O_4.

III. To evaluate the physical and chemical properties of $TiO_2/CS/Fe_3O_4$ nanocomposites by FESEM, EDX, HR-TEM, BET, XRD, VSM, PL, UV-DR, FTIR and XPS.

IV. To study the photocatalytic performance of synthesized nano composite for the photodegradation of ONP under visible light.

1.6 Strategies to modify the physico-chemical and photocatalytic properties of TiO_2

1.6.1 Magnetic TiO_2 photocatalyst

To overcome the recovery hurdle of TiO_2, magnetically separable photocatalyst consisting of both TiO_2 and magnetic material can be used (Kang et al., 2014). Thus, TiO_2 layer immobilized on magnetic particles, particularly with core shell structure, can be recycled back from the system by magnetic field. Magnetic iron oxide, mostly magnetite (Fe_3O_4), is frequently used as a core as it is nontoxic and economical in preparation (Cheng et al., 2012). Furthermore, the presence of iron in Fe/TiO_2 catalysts enhances the photocatalytic activity of TiO_2 by acting both as hole and electron traps (Zhao et al., 2010). However, a direct deposition Fe_3O_4 on to the surface of TiO_2 would decrease the photocatalytic activity of TiO_2 due to the photo-dissolution of Fe_3O_4 by the migration of $e^- – h^+$ from TiO_2 to the core particle (Fe_3O_4). Thus, an intermediate passive layer is mandatory between Fe_3O_4 and TiO_2 to avoid their direct contact and the subsequent Fe_3O_4 photo-dissolution (Cheng et al., 2012). The undercoat between Fe_3O_4 and TiO_2 can provide an insulated layer and also trap the holes to prevent the $e^- – h^+$ recombination in the TiO_2 (Kalan et al., 2016). Previous studies have reported the use of Al_2O_3 (Zhang et al., 2015), SiO_2 (Kang et al., 2014; Pang, et al., 2012) and graphene (Lu et al., 2013) as passive layers for the synthesis of TiO_2/Fe_3O_4. However, these materials are expensive, and their adsorptive capacity is also not as high as expected (Du et al., 2014).

Conversely, Chitosan (CS) has gained some interest due to its chemical and inherent properties (Haldorai & Shim, 2014). In recent years, the magnetite/CS (Fe_3O_4/CS)

nanoparticles have been extensively used for the purification of water due to their rapidity, simple operation process and high separation efficiency (Fu, 2014). CS is also harmless to humans and is widely employed for the removal of various environmental pollutants due to its promising biological characteristics and excellent adsorption properties (Mohseni al., 2015). The high adsorption is due to the presence of amine (–NH_2) and hydroxyl groups (–OH) on its surface. In comparison to other magnetic adsorbents, the cost of Fe_3O_4/CS is about 1/2 of amino-functionalized SiO_2-coated Fe_3O_4 and 1/3 of amine-modified SiO_2/Fe_3O_4 (Du et al., 2014).

1.7 Scope of research

In order to suppress the fate of e^-– h^+ recombination of TiO_2, enhance the performance under visible light and effective recovery after wastewater treatment, TiO_2 is modified with Fe_3O_4/CS. The research involves three phases. **Phase I** involves the preparation of Fe_3O_4/CS via co-precipitation method. Then TiO_2 nanoparticles are coated over Fe_3O_4/CS to form TiO_2/CS/ Fe_3O_4 nanocomposite. To evaluate the effect of each individual component (TiO_2, CS, and Fe_3O_4) on physicochemical and photocatalytic properties, the composites were prepared by varying concentrations of TiO_2, CS and Fe_3O_4.

Phase II involves the characterization of nancomposites to assess their physicochemical properties. The characterization includes Field emission scanning electron microscope (FESEM), Energy-dispersive X-ray spectroscopy (EDX), High resolution transmission-electron microscope (HR-TEM), Brunner-Emmet-Teller (BET), X-ray powder diffractogram (XRD), Vibrating sample magnetometer (VSM), Fourier transformed infrared spectroscopy (FTIR), Photoluminescence spectroscopy (PL), Diffuse-reflectance ultraviolet spectroscopy (DR-UV vis) and X-ray photoelectron spectroscopy (XPS).

Phase III involves the assessment of photocatalytic activity of core-shell nanocomposite for the degradation of ONP under visible light irradiation. Mineralization of ONP was assessed by Total Organic Carbon (TOC) analyzer. The percent degradation and degradation products were analyzed by UV-Vis spectrophotometer and Liquid chromatography-mass spectroscopy (LC-MS). The degradation pathway for ONP phenol was proposed.

1.8 Research Novelty

The present approach provides a more sustainable and feasible route for the synthesis of magnetically separable TiO_2/CS/Fe_3O_4, which overcomes the currently faced charge recombination and separation limitation of bare TiO_2. The modification improves the photocatalytic activity of TiO_2 under visible region of light. The current study introduces synthesis of ternary system by using 2 steps, in situ generation of Fe_3O_4/CS followed by coating it with a TiO_2. This provides more effective interactions between the individual components as in situ method allows the growth of nanoparticles inside the polymer matrix. To the best of our knowledge, magnetically separable TiO_2 nanocomposite system has not been synthesized using this strategy. TiO_2/CS/Fe_3O_4 nanocomposite not only has a high adsorptive capacity but can also be effectively recycled after wastewater treatment process. This approach can provide a more sustainable and feasible route for the treatment of wastewater.

1.9 Thesis organization

This thesis comprises five (5) chapters describing different aspects of the studies.

Chapter 1: Introduction

This chapter provides detailed current environmental issues related to wastewater treatment, especially water polluted with POP's such as ONP. The limitations of TiO_2 photocatalysis has been clearly described with a special emphasis on charge carrier recombination and recycling issues. Based on the problem statement, objectives of the study are described, and the scope of work and research novelty were explained.

Chapter 2: Literature review

This chapter critically reviews the previous and latest research scenarios of photocatalytic treatment of wastewater. The concepts, advantages and research gaps of TiO_2 photocatalysis for wastewater treatment in general and for POP's, were identified and explicitly explained.

Chapter 3: Methodology

This chapter includes the methodology adopted to fulfill the scope of work and research targets. The method of preparing nanocomposites by varying concentrations of TiO_2, CS and Fe_3O_4 was explained. Co-precipitation method was chosen for the in situ generation of Fe_3O_4/CS core nanoparticles, followed by the coating of TiO_2 shell. The equipment used such as FESEM, EDX, HR-TEM, BET, XRD, VSM, FTIR, PL, XPS, TOC analyzer, UV-vis spectrophotometer, LC-MS and the analysis parameters were clearly explained. The procedure for the photocatalytic degradation activity of ONP such as instrumental setup, and sampling were discussed. The performance of response surface methodology to optimize the process parameter was explained. The analysis procedure and instruments used for analyzing the degradation products were described.

Chapter 4: Results and discussion

This chapter consists of results and discussions of the physicochemical properties of synthesized TiO_2/CS/Fe_3O_4 nanocomposite, TiO_2/CS/Fe_3O_4 (varying concentration of TiO_2), TiO_2/CS/Fe_3O_4 (varying concentration of CS), and TiO_2/CS/Fe_3O_4 (varying concentration of Fe_3O_4). Characterizations of individual prepared nanocomposite are discussed separately in this section and their photocatalytic activities are detailed.

Chapter 5: Conclusion and future recommendation

This chapter summarizes the research findings, followed by a list of recommendations for future studies. Among the synthesized nanocomposites, the most active nanocomposite for the photodegradation of ONP is highlighted and the parameters influencing the photocatalytic activity are discussed.

CHAPTER 2: LITERATURE REVIEW

This chapter reviews the photocatalysis by TiO_2, the currently faced limitations, strategies to modify its properties and applications towards degradation of various pollutants. The influence of operating parameters on the photoactivity of TiO_2 is also detailed.

2.1 Photocatalysis

Photocatalysis is a process to speed up a chemical reaction by employing catalyst (photocatalyst) in the presence of light (ultraviolet, visible or infrared). The photocatalyst absorbs light, produces e^-– h^+ pair and promote chemical conversions of reaction participants and then regenerate its chemical composition. Oxides of metals such as vanadium, titanium, chromium, zinc, cerium and tin have photocatalytic characteristics involving light absorption, followed by a charge separation process with the formation holes that are capable of oxidizing organic substrates (Khan et al., 2015).

The key applications of photocatalysis include the reduction of COD (chemical oxygen demand), degradation of dyes and harmful herbicides, fungicides and pesticides, mineralization of organic pollutants, destruction of inorganic hazardous materials such as cyanides; treatment of heavy metals and malodorous compounds, purification and decontamination of indoor air and soil, destruction of viruses and cancer cells, purification and disinfection of water (Kabra et al., 2004) (Figure 2.1).

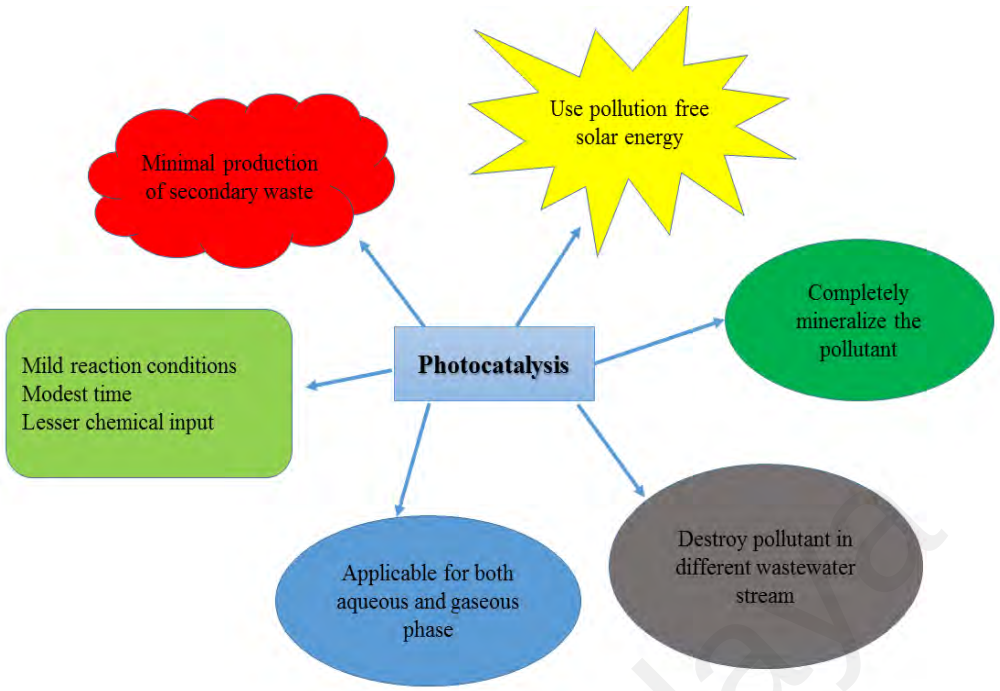

Figure 2.1: Advantages of photocatalysis

2.1.1 Mechanism of photocatalysis

The primary reactions in semiconductor photocatalysis are electrochemical oxidation or reduction reactions, involving the transfer of e^- and h^+ from the photo-excited semiconductor (Byrne et al., 2015). Semiconductors possess a void energy region that extends from top of the filled VB to the bottom of the empty CB, called the band gap. When a semiconductor absorbs a photon of energy (hυ) equal or higher than its band gap, an electron (e^-) excites from the valence band to the CB. This transition creates a positive hole/electron vacancy in the VB. The generated e^-– h^+ pair thus migrate to the surface of photocatalyst where it can either recombine, produce thermal energy, or participates in redox reactions with the adsorb compounds on the photocatalyst surface (Kabra et al., 2004) (Table 2.1).

Table 2.1: Basic principle of photocatalysis and radical formation

Step	Description	Mechanism
1	Photoexcitation of semiconductor molecule (e^- – h^+ pair generation)	Semiconductor + hv → e^-_{cb} + h^+_{vb}
2	Recombination of e^- – h^+ pair	e^-_{cb} + h^+_{vb} → heat + semiconductor
3	The CB electron can migrate to the semiconductor surface and directly reduced the absorbed organic pollutant	Pollutant + e^-_{cb} → Reduced species
4	The CB electron can migrate to the semiconductor surface and reduce absorb oxygen molecule to form superoxide anion radicals	O_2 + e^-_{cb} → $O_2^{\bullet-}$ Organic pollutant + $O_2^{\bullet-}$ → Reduced species
5	Hydroxyperoxyl radical is formed from superoxide anion via reductive path way	$OO_2^{\bullet-}$ + H^+ → $^{\bullet}OOH$
6	Formation of hydrogen peroxide and oxygen molecules	$^{\bullet}OOH$ + H^+ → H_2O_2 $^{\bullet}OOH$ + $^{\bullet}OOH$ → H_2O_2 + O_2
7	Formation of hydroxyl radical and its attack on organic pollutant	H_2O_2+ e^-_{cb} → OH^- + $OH^{\bullet}$ Pollutant + $OH^{\bullet}$ → Reduced species
8	A VB hole can migrate to the catalyst surface and directly oxidize the absorb organic pollutant	Pollutant + h^+_{vb} → Oxidized species
9	A hole can migrate to the surface water molecules to generate hydroxyl radicals	H_2O + h^+_{vb} → $OH^{\bullet}$+ H^+
10	The generated hydroxyl radical on catalyst surface oxidize pollutant molecule	Pollutant + $OH^{\bullet}$ → Oxidized species

The hydroxyl radicals ($OH^{\bullet}$) which are generated during this process are considered as the primary oxidant in the photocatalytic reactions (Figure 2.2) (Kabra et al., 2004).

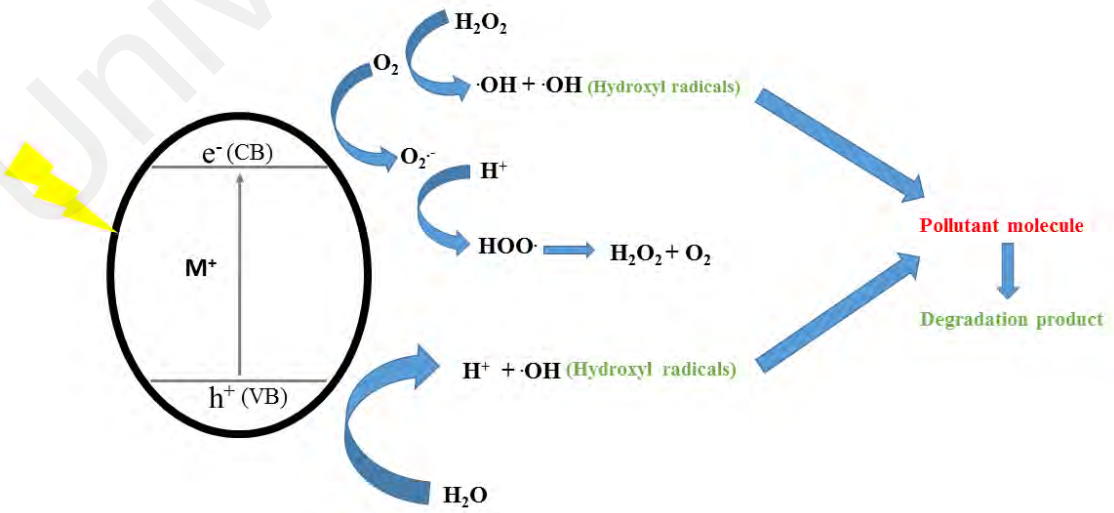

Figure 2.2: Basic mechanism of photocatalysis on the surface of semiconductor

2.2 Semiconductor photocatalyst

2.2.1 TiO_2

The photoactivity of TiO_2 was first observed in 1929 when it was used in buildings as a white pigment. The TiO_2 building pigment was found to be bleached under long term exposure to solar radiation. A well-founded report on the photocatalytic activity of TiO_2 was published in 1938, which stated that the TiO_2 surface produces active oxygen species by the absorption of UV, responsible photo bleaching of dyes (Lan et al., 2013). An intensive research began when Formenti et al., and Fujishima and Honda in early 1970's revealed the possibility of hydrogen production through water splitting by photocatalysis in electrochemical cell supported TiO_2 set up. Subsequently, tremendous research starts on TiO_2 photocatalysis in the academic and industrial sectors.

2.2.2 Applications of TiO_2

After the renowned work of Fujishima and Honda, the interest in TiO_2 as a photocatalyst increased exponentially both in the academia and industry (Hernández-Alonso et al., 2009). It can be easily synthesized in laboratory as a colloidal dispersion in liquid phase and often obtain as a thin film on a substrate. The ease of applying these forms highlights their potential applications. It can maintain its water solubility and having a strong resistance towards alkalis and acids. As charge pair on the surface of TiO_2 directly reacts with the solid lattice under irradiation, it does not undergo any photo-corrosion.

As a photocatalyst, TiO_2 have widespread applications including hydrogen production, self-purification, air cleaning and metal anticorrosion (Lee & Park, 2013) (Figure 2.3). It remains a remarkable material owing to high oxidation efficiency, photostability and nontoxicity. Furthermore, due to its large abundance in earth crust (0.44%), it is low

cost, chemically inert and capable of mineralizing large number of refractory organic pollutants including herbicides and dyes (Daghrir et al., 2013).

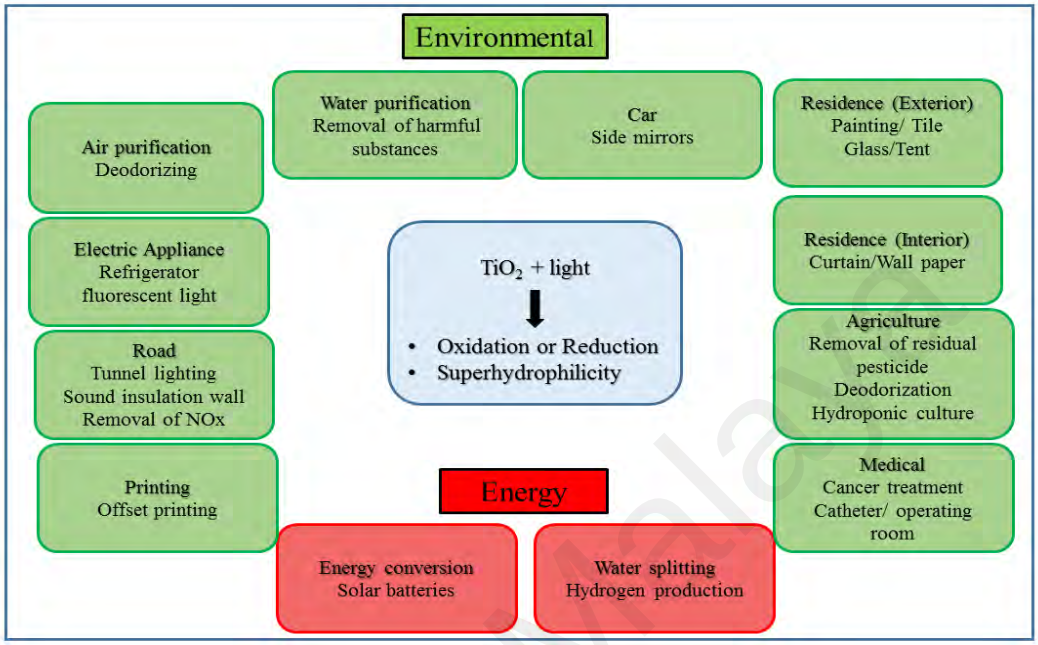

Figure 2.3: Applications of TiO_2 photocatalysis (Lee & Park, 2013)

2.2.3 Other Semiconductors

Various photoactive semiconductors have been developed in the last few years as alternative to TiO_2. These include mix oxides of transition metals such as Vanadium (V), Niobium (Nb) or Tantalum (Ta) and main group elements like Gallium (Ga), Indium (In), Antimony (Sb) and Bistmuth (Bi) (Hernández-Alonso et al., 2009).

ZnO is a close competitor in this respect as it shows similar activity under certain conditions, but unlike TiO_2, it suffers from anodic photo-corrosion and the reaction cannot be retarded by oxidation of H_2O. Its solubility in strong acids and alkalis limits the operational pH range. Moreover, it readily dissolves in H_2O and produce $Zn(OH)_2$ on the surface of ZnO which decline its activity over time (Gupta & Tripathi, 2011).

CeO_2, with its property of strong absorption of UV and visible light, can also be considered as an attractive photocatalyst. It is stable under illumination; however, it is found to be less active under UV light.

SnO_2 and WO_3 have been extensively utilized as additive to enhance the photocatalytic activity of TiO_2. Bare SnO_2 have a band gap of 3.88 eV which makes it completely inactive as a photocatalyst. WO_3 has remarkable electronic properties, but its degradation rate towards organic pollutants is usually low due to high e^-– h^+ recombination rate. The low degradation rate might be due to over potential effect, which makes it difficult to photo reduce oxygen (Hernández-Alonso et al., 2009).

Unlike TiO_2, other semiconductors like GaP, CdS and ZnO cannot be used for environmental purification as they produce toxic by-products during photocatalysis due to their solubility in the solution (Lee & Park, 2013). Similarly, PbS, GaAs and CdS are toxic and undergo photo corrosion and thus, cannot be used as catalyst in aqueous media (Gupta & Tripathi, 2011).

2.2.4 Limitations of TiO_2

As the band gap of TiO_2 is ~3.2 eV (anatase), it can be photo activated by absorbing irradiation in UV region which constitutes only 5% of the sun's energy in comparison to visible light (45%). This is one of the major limitations of TiO_2 which restrict its application on a large scale. The shift in the optical response of TiO_2 from the UV to the visible light has profound effect on its practical applications (Dong et al., 2015). Besides the utilization of solar spectrum efficiently, another factor which declines the photocatalytic performance of TiO_2 is the high tendency recombination of charge carriers (e^- and h^+) generated during the excitation of TiO_2. Photocatalytic process is productive only when e^- and h^+ recombination is suppressed (Anandan, et al., 2010).

Meanwhile TiO_2 has a poor affinity towards organic pollutants (especially hydrophobic), which results in low photocatalytic degradation rates due to low adsorption of these pollutants on TiO_2 surface. Therefore, the targeted organic pollutant should concentrate on the TiO_2 surface to minimize this mass transfer limitation. Furthermore, the nanosized particles can aggregated during photocatalysis, which hindered the incident light to the active sites of the photocatalyst and consequently, decreasing its overall photocatalytic activity (Dong et al., 2015; Gupta & Tripathi, 2011).

TiO_2 nanoparticles can diffuse into the aquatic environment and are released to surface water during photocatalysis. As nanoparticles themselves are emerging class of contaminants, the higher concentration of TiO_2 nanoparticles could pose bad impacts on the ecological ecosystem (Daghrir et al., 2013). Therefore, the recovery of TiO_2 nanoparticles from the reaction medium after the photocatalytic process is another challenge. The limitations of TiO_2 based particles for the degradation of organic pollutants are summarized in Figure 2.4 (Dong et al., 2015).

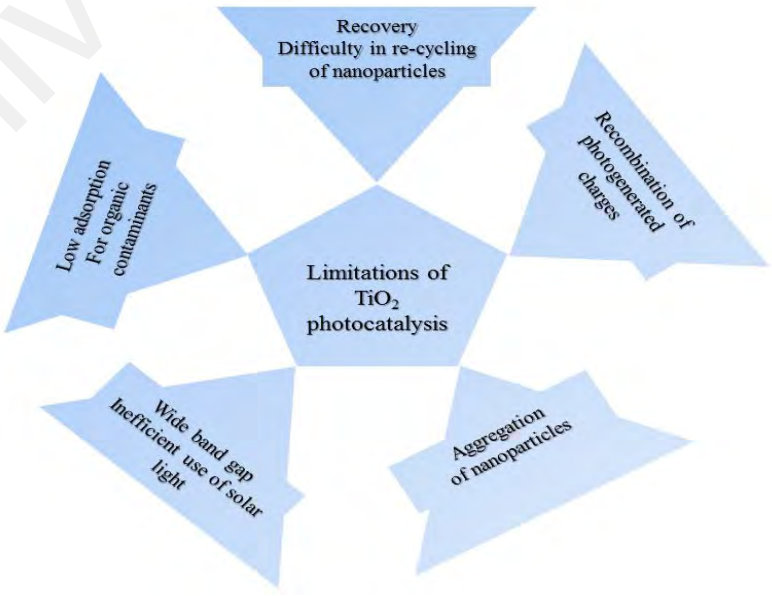

Figure 2.4: Limitation of TiO_2 in application of photocatalytic degradation reactions

2.3 Strategies to overcome limitations of TiO_2

To date, the major concern about TiO_2 is to modify its physicochemical properties to overcome its limitations. The modifications could be through doping, dye sensitization, synthesis of composite catalyst and small band gap semiconductors (Pattanaik & Sahoo, 2014). These attempts may improve the photocatalytic performance of TiO_2 by shifting its absorption in the visible region of spectrum, with efficient charge carrier separation and recycling properties.

2.3.1 Doping

Doping is an approach of band gap engineering to improve the optical response of photocatalyst. In doping, an intra-band gap state is introduced to shift the absorption towards visible light (Gupta & Tripathi, 2011). In TiO_2, doping modifies its micro and electronic structure, prevent the anatase to rutile transformation and generate defects. Doping could be done using cations (metal) or anions (non-metals). In doping, alteration in the electronic structure occurs, however, the structural integrity of the photocatalyst should be maintained. Like in TiO_2, it is feasible to substitute Ti^{4+} with cation than O^{2-} with anion due to the difference ionic radii and oxidation states (Pattanaik & Sahoo, 2014).

Metal doping introduces a new energy level within the band gap of TiO_2, which results in the red shift in the absorption from UV to visible region. Additionally, metal doping trap electron and inhibit the recombination of e^-– h^+ while the available holes take part in oxidative pollutant degradation (Figure 2.5).

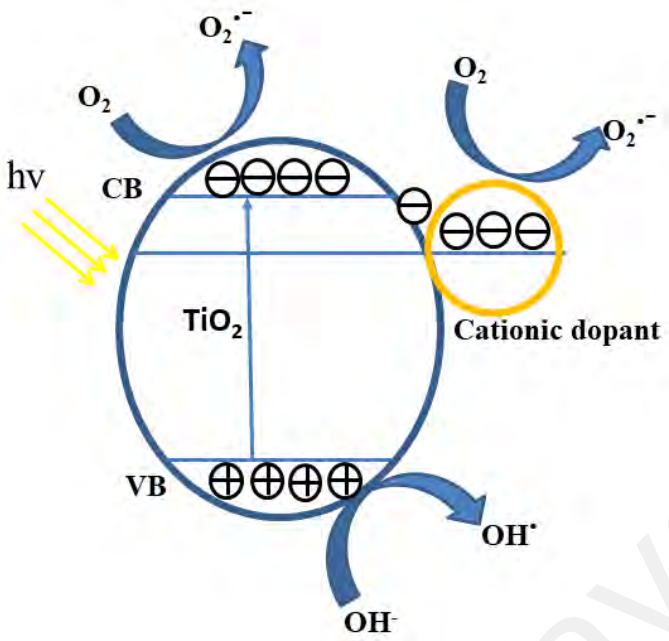

Figure 2.5: Proposed photocatalytic degradation mechanism by cationic dopant on TiO_2 surface (Mun et al., 2016)

Several metal ions have been examined as potential candidates to induce visible light photocatalysis, including Vanadium (V), iron (Fe), chromium (Cr), cobalt (Co), nickel (Ni), ruthenium (Ru), cerium (Ce), lanthanum (La) and platinum (Pt) (Pattanaik & Sahoo, 2014). Investigation of 21 metal ions including V (V), Fe (III), Ru (III), Mo (V), Os (III) and Re (V) as dopant to study the photocatalytic activity of TiO_2 was reported in literature. These dopants significantly enhanced the photoactivity of TiO_2 for the reduction of CCl_4 and oxidation of $CHCl_3$ (Gupta & Tripathi, 2011; Choi et al., 1994).

Transition metals with more than one oxidation states, such as Iron (Fe^{4+}, Fe^{3+}, Fe^{2+}), facilitates the photocatalytic activity of TiO_2 because they can trap the e^-– h^+ pair to prevent their recombination (Daghrir et al., 2013). However, by metal doping, an impurity energy level is induced which cause to increase the recombination rate of e^-–h^+ pair (Pattanaik & Sahoo, 2014). Furthermore, at high metal concentration during doping, metal ion can act as a recombination center (Gupta & Tripathi, 2011).

Nonmetal doping in TiO_2 shows more profound effects in shifting the absorption into visible light region as the induced impurity level is closer to the VB maximum (Figure.2.6). There is extensive literature on the use of nitrogen (N), Carbon (C), and Sulphur (S) to produce visible light active TiO_2 photocatalyst. N and C are the most extensively studied dopants for solar light driven TiO_2 photocatalysis. However, the C doping in comparison to other nonmetal dopants is reported to show the best photo-response and assume to behave as sensitizer in photocatalytic reactions.

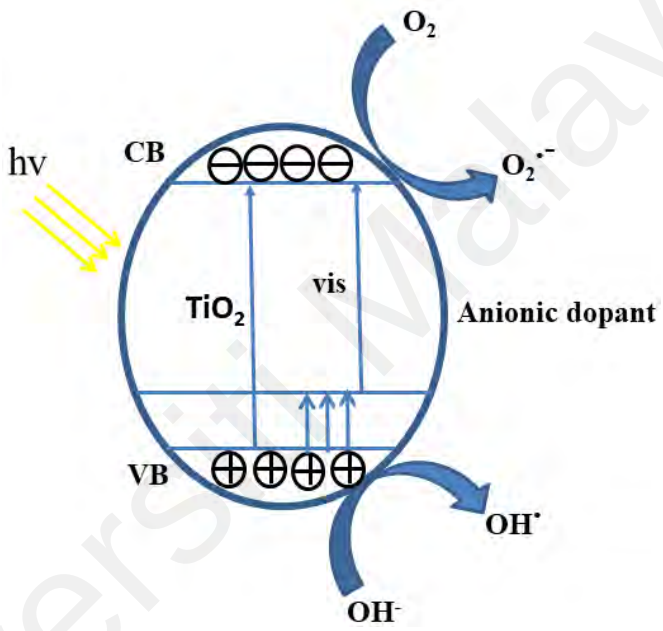

Figure 2.6: **Photocatalytic degradation mechanism by Anionic dopant on TiO_2 surface (Mun et al., 2016)**

Ohno et al. (2004) reported the degradation of 2-propanol, methylene blue (MB) and partial oxidation of adamantine by using S doped TiO_2 and observed high efficiencies in visible region (Ohno et al., 2004). The degradation of phenol in visible light by using S-doped TiO_2 was also reported in the literature (Rockafellow et al., 2009). Gurkan et al. (2013) investigated the improved photodegradation of 4-nitrophenol with Se (IV)-doped TiO_2 under sunlight and UV-A (Gurkan et al., 2013). In contrast to metal ions, the

nonmetal dopant substitute lattice oxygen and rarely causes e^{-}– h^{+} recombination (Pattanaik & Sahoo, 2014).

2.3.2 Dye sensitization

Dye sensitization is another approach to achieve the photocatalytic applications of TiO_2 in the visible light region. Dye sensitized TiO_2 can be synthesize in ambient environment by adsorption of dye molecule on its surface (Pattanaik & Sahoo, 2014). The mechanism is based on the excitation of electron of dye molecule from highest occupied molecular orbital (HOMO) to lowest unoccupied molecular orbital (LUMO) by the absorption of visible light. The dye molecule is then converted to radical cation by the transfer of excited electron to the CB of TiO_2. For this transition, the LUMO of the dye molecules should be more negative than the CB of TiO_2. In the whole mechanism, the VB of TiO_2 remain unaffected and it behaves as facilitator for electron transfer. The transferred electron jumped to TiO_2 surface and reacted with molecular oxygen and give rise to superoxide radical ($O_2^{\bullet-}$) and hydrogen peroxide radical ($^{\bullet}OOH$), which further disproportionate to yield $OH^{\bullet}$ (Figure 2.7). These resultant radicals participate in the degradation of pollutant molecule (Pelaez et al., 2012). The use of dye sensitizer to enhance the visible light photocatalytic performance of TiO_2 is summarize in the table 2.2.

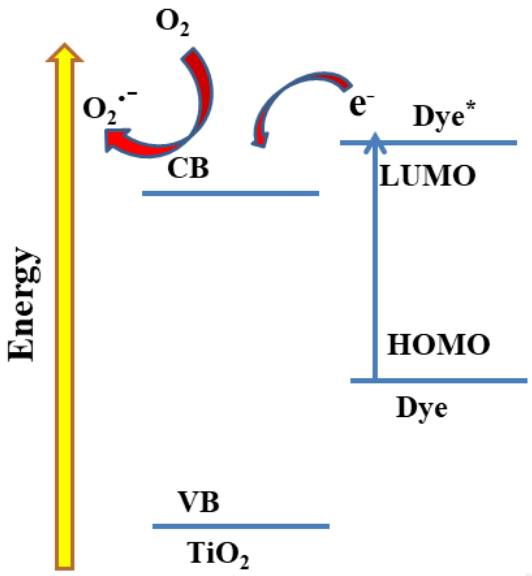

Figure 2.7: Mechanism of dye sensitization on the surface of TiO_2

Table 2.2: Dye sensitize TiO_2 for photocatalytic degradation of pollutants

Photocatalyst	Dye sensitizer	Pollutant	Reference
$(Ru^{II}L_3)Al_2O_3/TiO_2/Pt$	Ruthenium bipyridyl complexes ($Ru^{II}L_3$)	CCl_4	Kim et al., 2009
TiO_2/AZnPc	Zinc phthalocyanine	Rh-B	Flores et al., 2017
Eosin Y-TiO_2/Pt	Eosine Y	phenol	dye sensitize 3
TiO_2/PTCDI)-CuPcTs	Perylene tetracarboxylic diimide (PTCDI) and copper phthalocyanine tetrasulfonic acid (CuPcTs)	Rh-B	Shang et al., 2011
DCQ-TiO_2/SiO_2	2,9-dichloroquinacridone (DCQ)	4 imidazolium ILs	Huang et al., 2017

Despite the popular utilization of dyes as sensitizers, the quantity of the dye adsorbed on the TiO_2 surface is still crucial parameter because only this amount contributes to photocatalytic process. The extent of dye adsorption depends on the initial concentration of dye, the nature of dye, the surface of the photocatalyst and the pH of the solution. Besides, the photochemical properties of dyes and the interfacial transfers of electrons between dyes and TiO_2 are very important parameters to ensure superior

photoactivity. The frequent desorption of dye molecules reduces the potential use of this technique for practical applications (Daghrir et al., 2013).

2.3.3 Composites

Recently, multifunctional materials have gained great attention for their design and application in quantitative measurements (Janczak & Aspinwall, 2012). Variety of TiO_2 coupled semiconductors have been made including ZnO/TiO_2, Bi_2S_3/TiO_2 and CdS/TiO_2. These materials have improved photocatalytic efficiency and lower e^-–h^+recombination fate and show potential applications in photovoltaic devices, organic compound degradation and water splitting (Pelaez et al., 2012).

Nanocomposites have gained special interest due to their applications in catalysis, biomedical, industrial and many other fields (Kumar et al., 2013). Composite system particularly in a core-shell structures layer of one semiconductor deposited over another not only maintain the identity of individual component but also improves its selectivity as only one of the charge carriers is available at the surface (Pelaez et al., 2012; Gupta & Tripathi, 2011). The trap electron generated at the heterojunction as a result of electronic interactions enhances its photocatalytic efficiency. These photo-generated e^- and h^+ are utilized in redox reactions according to conduction and valence band's potential of semiconductors (Pelaez et al., 2012). These core-shell structures impart additional photoelectro chemical strength and stability to the system as many of semiconductors (particularly group II–VI compounds) in aqueous media are susceptible to anodic photo-corrosion (Gupta & Tripathi, 2011). In addition, the combination of large band gap with a small band gap semiconductor triggered by solar radiation is of great interest. A thin layer of wide band gap material onto small band gap dramatically enhances the photostability (Figure 2.8). CdS, for instance, is an ideal candidate for solar driven applications due to a small band gap (2.4 eV). However, it is sensitive to

photo-anodic corrosion in aqueous medium. The coupling of CdS with comparatively wide band gap semiconductor (ZnO and TiO_2) overcome the stability issue and enhances separation of charge carriers (Pelaez et al., 2012).

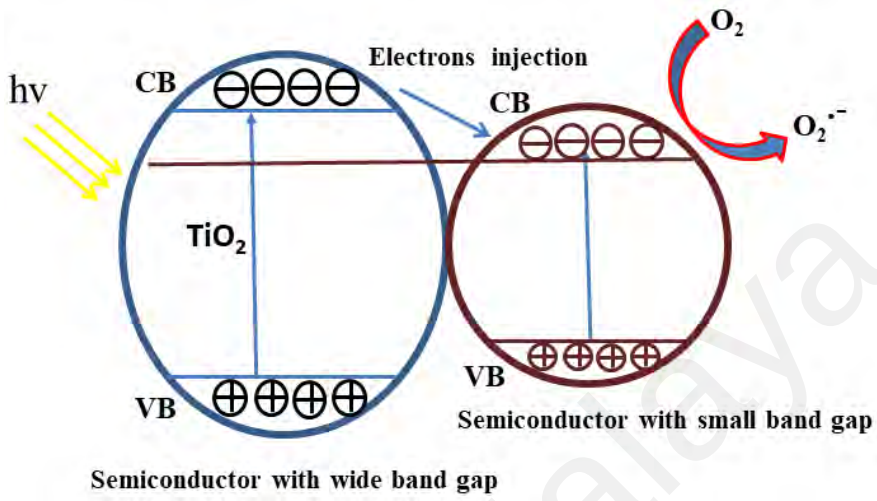

Figure 2.8 : The band structure of a composite photocatalyst, prepared by a mixture of narrow and wide band gap photocatalysts (Mun et al., 2016)

The above-mentioned strategies shift the photoactivity of TiO_2 to the visible region of light and help to facilitate the e^-– h^+ separation. However, the problem of recycling of catalyst from huge volume of water which needs additional cost is still a matter of concern.

2.4 Magnetite nanoparticles

The previously proposed solution for recycling limitation is the immobilization of TiO_2 nanoparticles on a support such as glass, carbon, SiO_2, quartz zeolite, alumina and others (Luan et al., 2014). However, this strategy results in the lowering of surface area, low mass transfer and hence, low photocatalytic activity.

An alternative solution for separation and reuse issue of TiO_2 is the use of composite system consisting of magnetic photocatalyst which can be efficiently separated from the

reaction medium by applying an external magnetic field. By using this approach, agglomeration of photocatalyst can be prevented in the recovery stage and cost associated with its separation is reduce or even eliminated and the long-term durability of the photocatalysts may be improved. The successful synthesis of separable Fe_3O_4/TiO_2 core-shell nanocomposite for Rhodamine B (RhB) degradation was reported in the literature (Xin et al., 2014). Recently, another separable core-shell photocatalyst ($Fe_3O_4@SiO_2@mTiO_2$) by using an outer layer of mesoporous TiO_2 ($mTiO_2$) for MB degradation was successfully applied (Wang et al., 2017a).

Magnetic nanoparticles with excellent magnetic properties and attractive features like plenty of reactive sites on their surface, high adsorption efficiency, large specific surface area and harmlessness make them suitable candidate for ferrofluids, magnetic storage media, drug delivery and catalysis (Pasandideh et al., 2016; Liu et al., 2008b). They have attracted researchers from various fields due to their unique magnetic and electrical properties not only in the field of magnetic recording media, but also in medical applications, including drug delivery systems, magnetic resonance imaging (MRI), cancer therapy, magneto-optic devices and others (Majidi et al., 2014). Fe_3O_4 nanoparticles are frequently used in photocatalytic processes as a core material due to their abundance and economical synthesis methods (Wei Wu et al., 2015).

However, they undergo leaching in acidic medium and tend to aggregate due to high surface energy, resulting in the decline in their adsorption and magnetic properties. Therefore, the surface coating (with organic or inorganic) is desirable to maintain their stability and dispersibility (Mohamed et al., 2015). Generally, a nonmagnetic coating material is used to maintain the stabilization and surface functionalization of the core (Liu et al., 2008b).

2.4.1 Methods for the synthesis of Fe_3O_4 nanoparticles

The synthesis method of Fe_3O_4 nanoparticles is an important consideration as it determines the shape, size distribution, surface chemistry and their magnetic properties. Moreover, the synthesis methods also express the degree of structural imperfections or impurities in the particle, as well as the distribution of such defects, hence defining its magnetic behavior (Majidi et al., 2014). Several methods have been developed for the synthesize Fe_3O_4 NPs as explained below.

2.4.1.1 Microemulsion

Microemulsions are liquid mixtures of oil, water and surfactant, commonly in combination with a co-surfactant. A monolayer is formed by surfactant molecules at the interface between the oil and water. The aqueous phase may compose of metal salts and/or other ingredients, and the oil may consist of complex mixture of different hydrocarbons and olefins. Microemulsions might be direct, that is oil dispersed in water (o/w) and reversed, water dispersed in oil (w/o), used in the synthesis of Fe_3O_4 nanoparticles (Wei Wu et al., 2015).

This method is very advantageous over other methods due to high degree of control over particle size and composition, nanoparticles with high crystallinity and specific surface area, the use of simple equipment, and the use of nearly ambient temperature and pressure.

Mono dispersed maghemite nanoparticles were reported by the one-vessel microemulsion method. The spherical shaped maghemite nanoparticles, covered with a monolayer coating of oleylamine (or oleic acid), indicated well crystallized with a narrow size distribution of 3.5±0.6 nm, and having saturation magnetization (Ms) values of 76.3 Am^2/ kg for uncoated nanoparticles, 35.2 Am^2/ kg for oleic acid-coated nanoparticles, and 33.2 Am^2 /kg for oleylamine coated NPs. As the oil and water phases

frequently contain several dissolved components, the selection of the surfactant therefore depends upon the physicochemical characteristics of the system (Majidi et al., 2014).

A room temperature synthesis of Iron oxide nanoparticles has been reported to produce crystalline nanoparticles with mean diameters of about 3, 6 and 9 nm. The use of capping agent (polyoxyethylene (5) nonylphenylether as surfactant) during synthesis prevents the particle agglomeration which can occur during direct particle contact.

The challenges in using microemulsion procedures are the adverse effects of the remaining surfactants on the properties of the nanoparticles. In addition to the presence of surfactants, the aggregation of the produced iron oxide nanoparticles usually requires several washing processes and further stabilization treatments (Wei Wu, 2015; Majidiet al., 2014).

2.4.1.2 Thermal decomposition

In this method, the decomposition of iron precursors occurs in the presence of hot organic surfactants, which yield a product with narrow size distribution, high crystallinity and dispersible iron oxide nanoparticles. The organometallic precursors include carbonyls (such as $Fe(CO)_5$), $[M^{n+}(acac)_n]$, (M= Fe, Mn, Co, Ni, Cr; n= 2 or 3, acac = acetylacetonate) or $M^{x}(cup)_x$ (cup =N-nitrosophenyl hydroxylamine). Organic solvents and surfactants such as fatty acids, oleic acid, and hexadecylamine are used commonly as stabilizers (Majidi et al., 2014). The stabilizer can slow down the nucleation process and favors the formation of small iron oxide nanoparticles. Furthermore, thermal decomposition is also used to obtain iron oxide with different shapes, such as nanospheres and nanocubes.

For instance, the synthesized Fe_3O_4 nanocubes and nanospheres using thermal decomposition of various mixtures of ferrocene and polyvinylpyrrolidone (PVP) was

reported. The described method offered a simple single step process for the generation of Fe_3O_4 nanocubes/spheres (Wei Wu et al., 2015). It has also been reported that monodisperse Fe_3O_4 NPs with sizes from 3 to 20 nm can be prepared at high temperature (265˚C) by reaction of iron (III) acetylacetonate in phenyl ether in the presence of alcohol, oleic acid, and oleylamine (Majidi et al., 2014). In thermal decomposition, however, surface treatments and laborious purification steps are necessary before the product can be used in biomedical applications. Moreover, the resulting nanoparticles are generally organic soluble and only dissolved in nonpolar solvents (Wu et al. 2008).

2.4.1.3 Hydrothermal

Hydrothermal method is one of the most successful ways to grow crystals and ultrafine powders of many different materials. This technique is based on crystallizing a material from aqueous solution in a sealed container at a high temperature ranging from130 °C to 250 °C, and at high vapor pressure (0.3 to 4 MPa). The size of particle and its distribution increased with the precursor concentration. By changing the precursor (ferric nitrate) concentration from 0.03 to 0.06 M, keeping all other variables constant, spherical particles with an average particle radius of 15.6 ± 4 .0 nm were obtained at the precursor concentration of 0.03 M.

However, hydrothermal approaches still fail to obtain nanocrystals smaller than 10 nm with hydrophilic surface properties. For instance, the synthesis of Fe_3O_4 NPs with a diameter of 27 nm using the hydrothermal method in the presence of a surfactant, sodium bis (2-ethylhexyl) sulfosuccinate was reported (Zheng et al., 2006). Similarly, Fe_3O_4 powder with a diameter of 40 nm was synthesized using the hydrothermal method at 140 °C for 6 hours. Another problem of using conventional hydrothermal method is the slow reaction kinetics at any given temperature. However, microwave

heating can increase the kinetics of crystallization during the hydrothermal synthesis (Majidi et al., 2014).

2.4.1.4 Sol gel

Sol-gel is a wet route for the synthesis of nanostructured metal oxides. This method is based on the hydroxylation and condensation of metal alkoxide precursors in solution, originating a "sol" of nanometric particles. Further condensation and inorganic polymerization lead to the formation of 3D metal oxide network, as a wet gel. As these are room temperature synthesis techniques, extra heat treatments are required to obtain the final crystalline state. The factors that influence the growth, hydrolysis and condensation reactions are the type of solvent, precursors, temperature, catalysts, pH, and mechanical agitation. The sol-gel process offers the synthesis of nanoparticles with mono dispersibility, pure amorphous phases, with good homogeneity and control of the particle size. Nanoparticles with a predetermined structure can be obtained by maintaining experimental conditions. For instance, synthesis of Fe_3O_4 nanoparticles via sol-gel technique combined with annealing at temperatures of 200 °C, 300 °C, and 400 °C was reported and the characterization results revealed that by changing the annealing temperature, the size of Fe_3O_4 nanoparticles could be changed (Shaker et al., 2013). However, the sol-gel method includes pollution from by-products of reactions, as well as the need for post-treatment of the products, which limits the application of this method (Majidi et al., 2014).

2.4.1.5 Co-precipitation

This is the most widely used method for the synthesis of iron oxide nanoparticles with controlled size and magnetic properties (Vashist, 2013). It is extensively used for biomedical applications as it requires less harmful materials and procedures. The synthesis of the iron oxide nanoparticles is carried out from aqueous salt solutions,

followed by the addition of a base at room temperatures or at high temperature (Faraji et al., 2010). The shape and size of the iron oxide nanoparticles depend on the type of salts used, such as chlorides, nitrates, sulfates, perchlorates and others. Other factors which play important roles in determining the overall properties are the ratio of ferric and ferrous ions, the pH value, the reaction temperature, and other reaction parameters such as stirring speed and dropping rate of basic solution. The synthesis of uniform monodisperse Fe_3O_4 nanoparticles with the diameter of 8.5±1.3 nm by co-precipitation without surfactants and with Fe^{2+} /Fe^{3+} molar ratio of 0.5 and a pH of 11 – 12 was reported in the literature (Wu et al., 2008). Similarly, the synthesis of Fe_3O_4 nanoparticles in an aqueous solution, including ferrous and ferric salts at various ratios, with 1,6-hexanediamine as a base was successfully reported. According to this study, the formation of large hydroxide particles as precursors of Fe_3O_4 was promoted at increased Fe^{2+} to Fe^{3+} ratio, resulting in an increase in the size of Fe_3O_4 nanoparticles from ∼9 to ∼ 37 nm. Moreover, the Ms of the iron oxide samples prepared with ferrous and ferric salts were 46.7 and 55.4 emu g^{-1} for sulfate and chloride, respectively (Iida et al., 2007). In the preparation of Fe_3O_4 nanoparticles, the temperature below 60 °C produced an amorphous hydrated oxyhydroxide that can be simply converted to Fe_2O_3, however, higher reaction temperatures (>80 °C) favor the formation of Fe_3O_4 (Govan et al., 2014). Conversely, in co-precipitation, the particles might to agglomerate due to extremely small size, high specific surface area and high surface energy. Moreover, the high pH value of the reaction mixture is also crucial and has to be adjusted during the synthesis and purification steps to produce uniform and monodisperse nanoparticles (Majidi et al., 2014). A summary of the synthesis methods is tabulated in Table 2.3.

Table 2.3: Summary of comparison of synthesis methods to produce Fe_3O_4 nanoparticles (Wei Wu et al., 2015)

Method	Reaction conditions	Reaction temperature (°C)	Reaction time	Size distribution	Yield
Co-precipitation	Very simple, ambient	20-150	Minutes	Relatively narrow	High/scalable
Thermal decomposition	Complicated, inert atmosphere	100-350	Hours-days	Very narrow	High/scalable
Hydro or solvothermal synthesis	Simple, high pressure	150-220	Hours-days	Very narrow	High/scalable
Sol-gel and polyol method	Complicated, ambient	25-200	Hours	Narrow	Medium
Microemulsion	Complicated, ambient	20-80	Hours	Narrow	Low
Sonolysis or sonochemical method	Very simple, ambient	20-50	Minutes	Narrow	Medium
Microwave-assisted synthesis	Very simple, ambient	100-200	Minutes	Medium	Medium
Biosynthesis	Complicated, ambient	Room temperature	Hours-days	Broad	Low
Electrochemical methods	Complicated, ambient	Room temperature	Hours-days	Medium	Medium
Aerosol/vapor method	Complicated, inert atmosphere	>100	Minutes-hours	Relatively narrow	High/scalable

2.5 TiO_2/Fe_3O_4 nanocomposite system

Magnetically separable photocatalyst consisting of both TiO_2 and magnetic material (Kang et al., 2014; Hu et al., 2011) in which TiO_2 immobilized layer on magnetic particles, particularly with core shell structure, could be recycled back from aqueous solution by an external magnetic field (Cheng et al., 2012).

For conventional Magnetic/TiO_2 binary nanocomposites, the photodissolution phenomenon occurs, resulting in loss of photoactivity. Lowering of the photoactivity of TiO_2/Fe_3O_4 than TiO_2 nanoparticles was observed in the literature for the destruction of sucrose. Owing to the direct contact of crystalline TiO_2 and iron oxide, the

photogenerated electrons from TiO_2 semiconductor feasibly transferred into the lower lying CB of magnetite and the holes transferred to the upper lying valance of this iron oxide resulting in an increase in the incidence of $e^- - h^+$ recombination as shown in Figure 2.9 (Yao et al., 2015). More importantly, these injected electrons also lead to the reduction of the iron oxide core with the Fe ions forming and migrating to the solution through the porous TiO_2 coating and cause photo-dissolution which may cause the loss of magnetism.

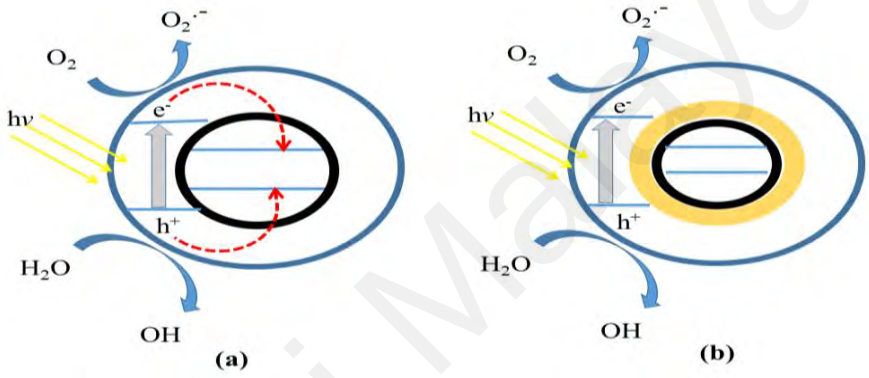

Figure 2.9: Schematic diagram of photoinduced charge transfer for TiO_2 (a) without intermediate layer and (b) with intermediate layer (Yao et al., 2015)

Therefore, an intermediate passive layer between Fe_3O_4 and TiO_2 is mandatory to avoid their direct contact and Fe_3O_4 photo-dissolution (Cheng et al., 2012). Due to these electronic interactions between TiO_2 and Fe_3O_4, alteration in their physicochemical properties would occur (Amir et al., 2015). Therefore, several attempts have been taken to maintain the photoactivity of TiO_2/Fe_3O_4 by applying different materials as intermediate layers between TiO_2 and Fe_3O_4. Compared with TiO_2/Fe_3O_4, a remarkable improvement in photocatalytic performance of this modified nanocomposite consisting of ternary system was observed.

2.5.1 Fe_3O_4 with support as passive layer

Suitable coating material such as, Au, polymer and SiO_2 might cover the magnetic dipole-dipole attractions between nanoparticles and helps in preventing their aggregation in addition to photo dissolution (Pasandideh et al., 2016).

2.5.1.1 Silica (SiO_2)

SiO_2 is traditionally used as coating material for magnetic nanoparticles as it is inert, highly stable, low cost, has easy processability and remains unaffected by the redox reactions of the core (Pasandideh et al., 2016; Liu, et al., 2008). These properties make SiO_2 an ideal coating material, which also maintains the physical integrity of the underlying core. Magnetic microspheres containing SiO_2 shell have been widely used for adsorption of protein and biomolecular separation (Hong et al., 2009). A nanocomposite powder Fe_3O_4:SiO_2 synthesized with improved oxidation resistance that linked to the oxidation protective effect by the SiO_2 matrix was reported (Lee et al., 2012). In another report, core-shell Fe_3O_4/SiO_2 nanoparticles were synthesized in which the thickness of the SiO_2 shell was controlled by modifying ratios and SiO_2 precursor, Fe_3O_4 and reaction time. These core shell nanoparticles can be used for bio-conjugation applications (Hui et al., 2011).

Composite system $TiO_2/SiO_2/Fe_3O_4$ displays remarkable improvement in photoactivity in comparison to TiO_2/Fe_3O_4. The percentage of iron oxide photo dissolution in $TiO_2/SiO_2/Fe_3O_4$ notably reached to nearly zero (Yao et al., 2015). In another report, the apparent degradation of Orange II improved by 8 times by $TiO_2/SiO_2/\gamma Fe_2O_3$ than that of $TiO_2/\ \gamma Fe_2O_3$. SiO_2 coating not only improves the acid resistance of $TiO_2/SiO_2/\gamma Fe_2O_3$ system, but also suppressed the $e^- – h^+$. However, the thickness of SiO_2 coat should be minimum enough, otherwise the photogenerated electron can transfer to the adjacent iron oxide core and the protection of photo-dissolution will

become inadequate (Yao et al., 2015). Furthermore, the attraction of SiO_2 towards oxygen due to its porosity and antioxidant ability is also a problem of concern (Liu et al., 2008b).

2.5.1.2 Carbon

Composite materials consisting of nanomaterial anchored on carbon matrix take great attention due to enlarge surface area, improvement in dispersion, stability and catalytic properties (Li et al., 2015). Carbon coating offers a perfect oxidation barrier to the Fe_3O_4 core material, hence preventing its corrosion. Consequently, carbon coating is considered as the most extensively used surface modification (Xia et al., 2013). Indeed, the hydrophilic nature of carbon helps to maintain dispersion and stabilization of nanocomposite (Bae et al., 2012).

Carbon as a support material is used in various forms such as activated carbon (AC), glucose, polymers, sucrose and applied for Lithium-ion batteries and photocatalytic applications. The most widely used carbon form is AC which possesses excellent adsorption properties and therefore frequently used for photocatalytic degradation of organic pollutants (Dahl et al., 2014). Lately, Fe and Fe_3O_4 coated with carbon in the form of nanorods, nanospindles and nanowires have been prepared and used in Lithium-ion batteries as anode material to enhance the electrochemical performance of bare Fe particles (Xia et al., 2013).

TiO_2 coated magnetic activated carbon (TMAC) was synthesized and used for the photocatalytic degradation of phenol in aqueous solution in comparison with bare TiO_2. TMAC shows 1.8 times higher photocatalytic performance than bare TiO_2 (Yao et al., 2015). However, the synthesis procedures and loading steps of nanomaterials while dealing with water soluble carbon are time taking and quite complex. The huge size of

carbon matrix and its hydrophobic nature further limits the composite's catalytic applications (Li et al., 2015).

2.5.1.3 Graphene

Graphene and its oxide form, graphene oxide (GO), have gained special attention by researchers due to their widespread applications and unusual thermal, electrical and mechanical properties. It has large surface area, high electron mobility, variety of defects and a range of functional groups including hydroxyl (OH), epoxy (C-O-C), and carboxyl (COOH) (Dahl et al., 2014; Wei et al., 2012). These properties help in designing and applying graphene as sensor, catalyst support and polymer composite (Yoon et al., 2016). The composite of graphene with TiO_2 has been studied extensively in application of Lithium-ion batteries and photocatalysis as electron capture, storage and transport properties of graphene enhances the charge separation in TiO_2. Meanwhile, the large surface area and high adsorption power facilitate the removal of organic pollutants (Amir et al., 2015; Dahl et al., 2014).

The combination of graphene with Fe_3O_4 in a composite system possesses high adsorption capacity with separation facility. Therefore, these composite systems have been synthesized extensively and used in MRI, drug delivery, membrane technology, water purification and catalysis (Vuong Hoan et al., 2016; Tayyebi et al., 2015). For instance, they are commonly used for the removal of dyes, heavy metals and organic pollutants. Recently, aternary system consisting of graphene/titania/magnetic nanocomposite are the focus of many researchers. A successful synthesis of TiO_2 and Fe_3O_4 nanoparticles on reduced GO have been reported and the resultant composite displayed a higher photocatalytic performance than both TiO_2/Fe_3O_4 and pure TiO_2 for the degradation of RhB (Lin et al., 2012). In another report, the synthesis of $TiO_2/GO/SiO_2/SrFe_{12}O_{19}$ nanocomposite was reported and it showed enhanced

photoactivity for 2,4-dichlorophenol degradation under direct sunlight (Abd Aziz et al., 2014). However, the limitations faced using graphene composite in aqueous-based application is its tendency to restack due to strong π-π interaction among graphene nanosheets (Yao et al., 2015).

2.5.1.4 Chitosan (CS)

CS is a carbohydrate biopolymer with same ß-glycosidic linkages derived by N-deacetylation of Chitin which is the main constituent of crustacean, shrimp or crab shell (Figure 2.10).

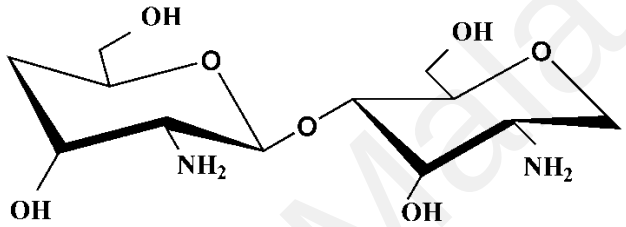

Figure 2.10: Structure of Chitosan

Due to its high porosity, biocompatibility, nontoxicity and biodegradability, it is regarded as an auspicious support material (Abdeen, 2016; Delmar & Bianco-Peled, 2015). Moreover, it is inexpensive and accessible abundantly than other support materials (Szymańska & Winnicka, 2015; Krajewska, 2004). The surface of CS contains plenty of functional groups namely –OH (hydroxyl) and –NH_2 (amino), which increase its adsorption capacity and function as reaction sites (Wang et al., 2016; Haldorai & Shim, 2014). Therefore, it is effectively used as adsorbent for the removal of variety of pollutants, including heavy metals, dyes, herbicides and pesticides (Kyzas & Bikiaris, 2015). It has also been used to detoxify water in water purification plants for the last 30 years. It provides an interface for charge transfer when used in the synthesis of nanosized materials, resulting in their improved photocatalytic activity. Numerous reports indicated that the immobilization of CS onto semiconductor as a support

provides great facility due to their low cost, ease of synthesis method and clean reusability (Nithya et al., 2014).

The combination of TiO_2 with CS was first explored by Zainal et al (Zainal et al., 2009) for the synergistic treatment of dye containing wastewater under visible light illumination. The as prepared catalyst was coated onto glass plates for a convenient wastewater treatment. In another report, a simple bilayer system consisting of TiO_2 and CS onto a glass plate was successfully synthesized and utilized for the removal of phenol (Lee et al., 2015b). Recent studies also exhibited multifunctional performance of CS and TiO_2 or ZnO in heterogeneous photocatalysis applications, including increased adsorption capacity and enhanced photocatalytic activity (Amir et al., 2017; Nithya & Jothivenkatachalam, 2015). Applications of CS based material for the degradation of dyes are tabulated in Table 2.4.

Table 2.4: CS based materials for the degradation of dyes (Nithya et al., 2014)

Metal oxide	Composite	Pollutant	Findings
TiO_2	TiO_2-CS porous material	Methylene blue	Maximum degradation rate reached 91% under UV-light irradiation.
TiO_2	TiO_2-CS immobilize on glass plate	Methyl orange	87% of photodegradation was achieved by four layer of TiO_2-CS glass photocatalyst.
ZnO	ZnO-CS composite	Direct blue 78	High adsorption capacity observed for DB 78 (25 mg/L) in presence of 0.5 g/L catalyst.
CdS	CdS-CS composite	Congo red	Degradation rates were 85.9% within 180min
CdS	CdS-CS composite	C.I. Acid red 86	Degradation rate reached 94.3% under visible light irradiation
Cu_2O	Cu_2O-CS composite	Brilliant red X-3B	Maximum degradation of 79% achieved under visible light irradiation
Nb_2O_5	CS-niobium (V) oxide	Indigo carmine	Exhibited high Photocatalytic efficiency for the degradation under UV-light irradiation.

In recent years, the use of magnetite/CS (Fe_3O_4/CS) nanoparticles has increased rapidly in water purification due to their speediness and great separation efficiency. In the literature, CS coated Fe_3O_4 nanoparticles as chelating agent and adsorbent were synthesized for the removal of bacteria and heavy metals from water. The report highlighted the adsorption capacity of different contaminants which is found to be highest (98%) for petroleum impurities (Nechita, 2017). A ternary system consisting of ZrO_2/Fe_3O_4/CS was reported to be successfully utilized for the treatment of Cr (VI) and 4-chlorophenol from simulated wastewater (Kumar et al., 2016). In another report, ZnO/Fe_3O_4/CS composite was prepared and used for the removal of a textile dye Reactive blue 198 (RB 198) (Nguyen et al, 2015).

Other than the above mentioned, various materials have also been reported as intermediate passive layers, including polymers such as poly (sodium 4-styrene sulfonate) (PPS^-) polyanion coupled with poly (diallyldimethylammonium) (PDD^+) cation, poly (methyl methacrylate. Some of the molecules and polymers used as coating material for Fe_3O_4 are listed in Table 2.5. Similarly, Au, fly ash, alumina, and zeolite are also used to improve photocatalytic and separation properties of the ternary composite system (Pasandideh et al., 2016; Amir et al., 2015; Yao et al., 2015).

Table 2.5: Different coating Molecules/polymers to stabilize Fe_3O_4 NP's (Ali et al., 2016)

Molecules/polymers	Benefits
Polyethylene glycol (PEG)	Improve biocompatibility by non-covalent immobilization of PEG on the surface, internalization efficiency of the NP's
Fatty acids	Terminal functional carboxyl groups and colloidal stability
Polyvinyl alcohol (PVA)	Give rise to monodisperse particles and prevents coagulation of particles
Polyacrylic acid	Improves biocompatibility of particles, also helps in bio-adhesion, and increase the stability
Gelatin	Biocompatible, natural polymer used as gelling agent

2.6 Applications of TiO_2 based composites in wastewater treatment

After Fujishima and Honda, TiO_2 has continuously been used in the form of nanopowders deposited on thin films or as nanotubes for the photocatalytic degradation of toxic contaminants (Fagan et al., 2016; Wang et al., 2014). The TiO_2 photocatalytic system is capable of decomposing recalcitrant pollutants due to its high oxidation power. The photo-induce charge carriers generate on the surface of TiO_2 and reactive oxygen species cause to inactivate microbes and mineralize the variety of organic pollutants (Lee & Park, 2013). TiO_2 with various supports used successfully for the degradation of numerous dyes and organic pollutants in aqueous solution as presented in Table 2.6.

Table 2.6: Applications of TiO_2 with various support systems for the degradation of textile dyes and organic pollutants

Photocatalyst	Type of Pollutants	Photocatalytic activities (%)	Time (minutes)	References
For the removal of textile dyes				
TiO_2-SiO_2	ß-naphthol	100	90	Qourzal et al., 2009
TiO_2/AC	Methyle orange	77	100	Mansoori et al., 2008
Fe_3O_4/SiO_2/TiO_2	Methylene blue	95	90	Teixeira et al., 2017
TiO_2-P25 Cu_2O-CuO/TiO_2	Reactive blue 49 (RB 49)	Irradiation time: 80min	76 100	Ajmal et al., 2016
ZnS/TiO_2	Acid blue 113 (AB113)	Irradiation time: 27.32 min	99	Talebi, et al., 2017
TiO_2/graphene	Methylene blue	Irradiation time: 150min	96	Yang et al., 2016
TiO_2/AC	Rhodamin B(Rh B)	Irradiation time: 120 min	93.2	Xing et al., 2016
Mesoporous TiO_2 doped by Ag coated graphen (MT-Ag/GR)	Methylene blue	Irradiation time: 160 min	100	Xiao et al., 2017
TiO_2/Fe_3O_4/Bentonite	Methylene blue	Irradiation time: 90 min	90	Chen et al., 2015

Table 2.6: Continued

For the removal of organic pollutants				
Photocatalyst	**Type of Pollutants**	**Photocatalytic activities (%)**	**Time (minutes)**	**References**
TiO_2 immobilized on SiO_2 gel	Dimethoate and glyphosate	100	60	Echavia et al., 2009
Eosine Ysensitized TiO_2/Pt	Phenol	93	90	Chowdhury et al., 2012
$Fe_3O_4/SiO_2/TiO_2$	Ciprofloxacin Norfloxacin Ibuprofen	95 95 60	90 90 90	Teixeira et al., 2017
CBC2-TiO_2 (TiO_2 and carbonized composites)	Benzene	72	180	(Mansoori et al., 2008

2.6.1 Persistent organic pollutant (POP's)

POP's are some of the most hazardous pollutants found in wastewater, particularly in chemical industries, sewage water effluents, landfills and others (Zhang et al., 2013). POP's are considered the most toxic set of organic pollutants because of their persistence, bio-accumulation, semi volatility long range atmospheric transport, and toxic even at very low concentration level. Thus, POP's results in adverse environmental and health effects. Figure 2.11.

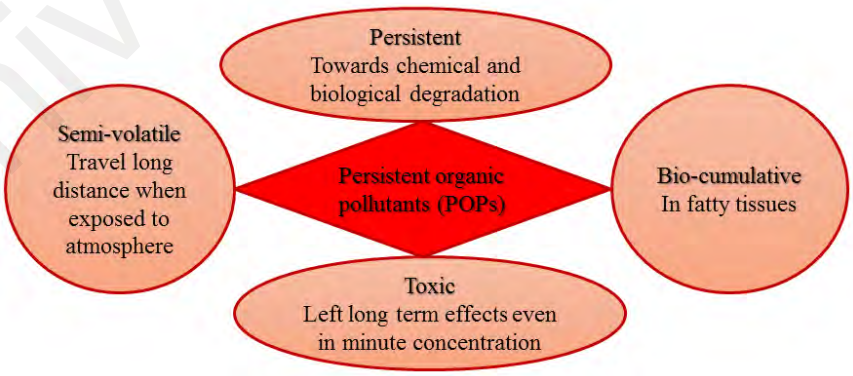

Figure 2.11: Persistent organic pollutant with their distinctive features

The extent of POP's pollution globally is now apparent, and they are detected in areas where they have never been produced or used, such as the Arctic. The source of their

exposure in environment is determined by type of their use and location which is listed in Table 2.7.

Table 2.7: The type of POP's and their sources (Vallack et al., 1998)

Types of POP's	Sources
Pesticides	Released intentionally from the point of their application in agriculture
Industrial chemical	Released intentionally during different industrial processes like volatilization, leaching or leakage during product's lifetime or when it is disposed off
Unintentionally by-products	Released from both mobile and stationary sources during combustion or industrial processes.

Photocatalysis reactions initiated by nanoTiO_2 are remarkable in degrading POP's due to its biological and chemical stability, high selectivity and ability to degrade pollutants even at trace level (Zhang et al., 2013). For instance, TiO_2 was used to study oxidative degradation of polychlorinated biphenyls (PCB's) namely 2,3,3′,4′-tetraCB, 2,3′,4′,5-tetra CB and 3,4,4′,5-tetra CB in water. About 90% decomposition of these three tetra CBs was reported within 120 min. Similarly, in another investigation, the efficiency of TiO_2-pillared mica for the photocatalytic degradation of hexachlorocyclohexans (HCH) was observed and TiO_2-pillared fluorine mica showed activity by two orders of magnitude than TiO_2. (Zhang et al., 2013).

2.6.1.1 Nitrophenol

Nitrophenols (NPs) are anthropogenic and considered as hazardous, priority pollutants by Public health service USA and USEPA (Liu et al., 2008c). They are widely used in the manufacture of pesticides, pharmaceuticals and dyes and appeared as intermediates during the degradation of pesticides like nitrofen and parathion (Di Paola et al., 2003). Therefore, they are largely released in wastewater coming from chemical and pharmaceutical industries (Atta et al., 2012). These NPs are mainly introduced into the environment through industrial discharge or as a result of the transformation of NPs

containing pesticides. Their presences in water produce unpleasant odor and taste. The momentary exposure cause skin irritation and may leads to severe skin disorders on constant exposure. The exposure through inhalation causes dizziness and headache, which may produce mutagenic and carcinogenic effects on the targeted organism if the exposure is consistent. USEPA classified ONP as a highly stable, non-biodegradable and recalcitrant which can bio-accumulate in the environment for a long period, with substantial endocrine disrupting properties (Tijani et al., 2017). The recommended limit for these NPs is in the range of 1 to 20 ppb in natural waters, according to USEPA (Liu et al., 2008c).

Degradation of NPs by biological means is not very effective as it takes long incubation time and extra stability and resistance of aromatic ring toward microbial degradation (Liu et al., 2008c). Other NP abatement methods include wet air oxidation, microwave enhanced catalytic degradation, ultrasound assisted degradation and photocatalytic degradation (Atta et al., 2012). However heterogeneous photocatalytic treatment using TiO_2 is an effective way as it gives complete mineralization of the organic pollutant without producing any residual intermediate (Di Paola et al., 2003). Ammar et al. (2007) reported the oxidative degradation of ONP by using electro Fenton process and observed the complete degradation of ONP and its aromatic intermediates in less than 2h (Ammar et al., 2007). Tijani et al. (2017) investigated ONP degradation by dielectric barrier discharge system alone and its combination with TiO_2 supported photocatalyst. They identified three pathways (hydroxylation, nitration and de-nitration) during ONP oxidation and OH was reported to be the most prominent oxidant for the ONP mineralization (Tijani et al., 2017). Similarly, Di Paola et al. (2003) utilized aerated TiO_2 suspension for the degradation of ONP and observed the formation of dihydroxy nitronezene isomers, which indicates that the $OH^{\bullet}$ oxidation is the major reaction

pathway for ONP degradation (Di Paola et al., 2003). Table (2.8) presents the degradation of various NPs using TiO_2 and TiO_2 based composite.

Table 2.8: Photocatalytic treatment of NP's using TiO_2 and TiO_2 based composites

Photocatalyst	Model pollutant	Experimental set up	Percent (%) degradation	Ref.
TiO_2 (Degussa P25)	4-nitrophenol	Pollutant concentration= 3.55 mg/L Catalyst dosage= 0.03g/L Light source= 5x8 W black light fluorescent lamp solution temperature = 21 ± 1	58.7 % degradation after irradiation of 160min	San et al., 2002
Multi-walled carbon nanotubes/TiO_2 (MWCNTs/TiO_2)	2,4-dinitrophenol	Pollutant concentration= 38.8 mg/L Catalyst dosage= 8 g/L Light source= solar	100% degradation in 150 min	Wang et al., 2009a
TiO_2 nanowires encapsulated graphene and palladium nanoparticles (G-Pd@TiO_2-CNWs)	4-nitrophenol	Pollutant concentration= 70 mg/L Catalyst dosage= 0.05g/L Light source= Red LED lamp	~100% degradation	Lee et al., 2015a
Silver dopped TiO_2 (Ag-TiO_2)	4-nitrophenol	Pollutant concentration= 4 mg/L Catalyst dosage= 1g/ L Light source= 20W black ray UV lamp	98% degradation in 1hour.	(Ilyas et al., 2011
TiO_2 Polycrystalline TiO_2 impregnated with tungsten (TiO_2/W)	4-nitrophenol	pollutant concentration= 20 mg/L catalyst dosage= 1.4g/L Light source= 125W medium pressure Hg lamp	100% degradation with bare TiO_2 in 3h. 95% degradation with TiO_2/W/0.3, TiO_2/W/1.0, TiO_2/W/2.0 27% degradation TiO_2/W/5	Di Paola et al., 2002
TiO_2-natural hematite-supported bentonite (TiO_2NHB)	4-nitrophenol	Pollutant concentration = 20 mg/L Catalyst dosage = 0.025g/L Light source = 25W UV lamp	98% degradation in 180min	Gaffour & Mokhtari, 2016

Table 2.8: Continued

Photocatalyst	Model pollutant	Experimental set up	Percent (%) degradation	Ref.
Silver and Sulphur co-doped TiO_2 (Ag-S/TiO_2)	2-nitrophenol	Pollutant concentration = 76 mg/L Catalyst dosage = 1g/L Light source = 15W UV lamp	99.8% degradation in less than 150min	Feiliazadeh et al., 2015
TiO_2-IL (Ionic liquid)	2-nitrophenol	Pollutant concentration = 45mg/L Catalyst dosage= 0.4g/100ml Light source = 250W high pressure Hg lamp	99% degradation in 120min	(Dai et al., 2014)

2.7 Effects of operating parameters on degradation rate

In aqueous medium, the photocatalytic degradation activity is governed by different parameters, comprising the initial concentration of pollutant, catalyst loading, pH of the reaction medium, dissolved and aerated oxygen, reaction temperature, wavelength and intensity of light used (Reza et al., 2017). Therefore, these operating parameters carefully adjusted during the photocatalytic degradation process.

2.7.1 Catalyst loading

At high catalyst concentration, the photoactivated catalyst provides more $OH^{\bullet}$ and more active sites are available, and consequently, the rate of photocatalytic reaction also increased. Conversely, at low catalyst concentration more of the light radiation transmitted from the reactor and less is utilized to precede the photocatalytic reaction, hence the rate of photocatalysis also decreases. However, beyond certain concentration (optimum concentration), the rate of degradation will decline as at higher concentration nanoparticles agglomerate and reduce the availability of active sites for photocatalytic process. Furthermore, it increases the light scattering events, causes turbidity or opaqueness of the reaction solution, and decrease the penetration of photon by the photocatalyst. The collision between activated molecules cause to deactivate them,

hence the overall photocatalytic activity will decrease. For instance, the degradation of ONP using ZnO nanoparticles at four different concentrations (0.025, 0.05, 0.1, 0.15) was reported and it was observed to increase by increasing amount of ZnO. However, after 0.05g no significant increase in the degradation was observed (Assi et al., 2015).

2.7.2 Initial concentration of pollutant

An increased concentration of pollutant molecule causes a decline in the photocatalytic degradation efficiency. This is because at high pollutant concentration, more pollutants are adsorbed on catalyst's surface, resulting in lowering the chances of photon to strike on photocatalyst surface to generate charge carrier ($e^- - h^+$) to bring about photocatalysis. Additionally, high pollutant concentration will accumulate on the surface of the photocatalyst and inhibit the production of $OH^\bullet$, resulting in reduced photocatalytic activity. For instance, the degradation of phenol by TiO_2-P25 was compared in literature by using initial concentrations of phenol from 0.13–1.01 mM and 90% of its removal occurred within 1h when the concentration is below 0.13 mM. This indicates the improved photocatalytic oxidation at low pollutant concentrations (Chiou et al., 2008).

2.7.3 pH of reaction medium

pH plays a significant role in the photocatalytic performance of catalyst as it affects its surface charge, VB oxidation potential, adsorption and degradation of organic pollutant. At high pH, the photocatalyst surface is negatively charged, which facilitates the adsorption of cationic molecules. Furthermore, at high pH values (pH>12) more $OH^\bullet$ are generated, which reduce the degradation of organic pollutant as hydroxyl ions compete with organic pollutant for adsorption on the catalyst surface. Conversely, at low pH, catalyst surface is positively charged, which reduces the adsorption of cationic

molecules, resulting in reduced degradation efficiency in acidic pH (Gnanaprakasam et al., 2015). Wang et al. (1999) studied the effect of pH on the degradation of 2-chlorophenol (0.1 mM) using TiO_2 and observed 95% degradation efficiency within 140min at acidic and neutral conditions. However, the degradation efficiency is about 60% at pH 11 (Wang, et al., 1999). Thus, an optimum pH must be adjusted for the degradation of organic pollutants.

2.7.4 Light Intensity

In a semiconductor catalyst, the $e^- - h^+$ is produced when the catalyst absorbs light equal or greater than its band gap. High intensity incident light increases the excitation of catalyst molecule, resulting in the increase in photodegradation efficiency. However, at low intensity of incident light, the $e^- - h^+$ separation competes with recombination which decreases the free radical formation and hence, reduces the overall photocatalytic degradation efficiency. Li et al. (2008) observed the degradation of RhB by TiO_2 coated AC and noted the enhancement in degradation rate as the light intensity increases. The degradation rates were observed at 10, 15, 25, 40 and 60 mW cm^{-2} and the highest was found at 60 mW cm^{-2}. This is due to higher production of $e^- - h^+$ pair at the high light intensity. Therefore, high intensity light would be preferable to achieved improved photocatalytic activity (Li et al., 2008).

2.7.5 Effect of oxidants

In photocatalysis, the $e^- - h^+$ recombination can be suppressed by the addition of irreversible electron acceptor such as $(NH_4)_2S_2O_8$, $K_2S_2O_8$, $KBrO_3$ and H_2O_2. H_2O_2 is most commonly used for this purpose to enhance the overall photocatalytic activity. Upon photolysis, H_2O_2 produces $OH^{\bullet}$ on the photocatalyst surface and also trap

electrons, thus, increasing the photocatalytic degradation efficiency. The mechanism by which H_2O_2 produces $OH^{\bullet}$ and trap electron is given as below:

$$H_2O_2 + O_2^{\bullet-} \rightarrow OH^{\bullet} + OH^- + O_2 \quad \textbf{(2.1)}$$

$$H_2O_2 + hv \rightarrow 2\ OH^{\bullet} \quad \textbf{(2.2)}$$

$$H_2O_2 + e_{CB} \rightarrow OH^{\bullet} + OH^- \quad \textbf{(2.3)}$$

However, quenching of $OH^{\bullet}$ by H_2O_2 could occur when the concentration of H_2O_2 increased beyond the optimum level. This will cause to decrease the overall degradation efficiency. Sobana and swaminathan (2007) studied the addition of H_2O_2 beyond the optimum concentration, which resulted in the reduction of photocatalytic activity due to the generation of peroxide radical that acts as a hole scavenger (Gnanaprakasam et al., 2015; Sobana & Swaminathan, 2007). Likewise, Tseng et al. (2012) reported the degradation of monochloro benzene by TiO_2 suspension under varying concentration of H_2O_2 (5.6 to 78 .0 mgL^{-1}). The degradation rate was observed to increase when the H_2O_2 concentration increases from 5.6 to 22.5 mgL^{-1}. However, a further increase from 22.5 to 78 mgL^{-1} significantly decreased the rate of degradation. H_2O_2 traps the photoinduced e^- and prevent the $e^- - h^+$ recombination and hence, enhance the degradation rate. Beyond the optimum concentration, H_2O_2 would trap the $OH^{\bullet}$ to form a weaker oxidant, $HO_2^{\bullet}$, according to the equations as below (Tsenget al., 2012).

$$H_2O_2 + OH^{\bullet-} \rightarrow H_2O + OH^{\bullet}_2 \quad \textbf{(2.4)}$$

$$HO^{\bullet}_2 + OH^{\bullet-} \rightarrow H_2O + O_2 \quad \textbf{(2.5)}$$

2.7.6 Effect of temperature

Generally, the photocatalytic degradation efficiency of a photocatalyst is enhanced by increasing the temperature. Increase in temperature facilitates the degradation by producing bubbles in the reaction solution, which generates free radicals. Secondly,

high temperature overcomes the recombination of e^{-}– h^{+}, thereby increasing the photocatalytic efficiency. Thirdly, a high temperature condition may improve the oxidation rate of organic compound at the interface (Gnanaprakasam et al., 2015). Sugiyama et al. (2014) investigated the effect of temperature (ranging 10 ºC to 50 ºC) on the photodegradation of ethylenediaminetetraacetic acid (EDTA) by TiO_2 and reported an increase in the degradation rate up to 25˚C. However, no significant enhancement was observed after 25˚C (Sugiyama et al., 2014). In another report, Ishiki et al. (2005) determined the temperature effect (between 20 ˚C and 40 ˚C) on the photocatalytic degradation of imazethapyr herbicide on TiO_2/H_2O interface. The degradation of herbicide was more favorable at lower temperatures, perhaps due to the lower physisorption between the imazethapyr molecules and TiO_2 surface. Therefore, the effect of temperature seems to also be dependent on the target pollutant (Ishiki et al, 2005).

2.8 Summary of Literature review

Photocatalysis employing semiconductor is a promising technology for the treatment of wastewater containing different pollutants such as POP's. TiO_2 semiconductor is the most studied and used photocatalyst in this regard. However, the photocatalytic applications of TiO_2 are limited to UV region which comprise only four percent of sun's energy. Secondly, the charge carrier generated during photocatalysis has a strong recombination ability, which declines the overall activity of the photocatalyst. Thirdly, and most importantly, the recycling issue faced while using nanoparticles TiO_2 limits their applications as the non-recyclable TiO_2 inside the reaction medium can cause secondary toxic effects. Therefore, different strategies have been employed to overcome these drawbacks.

Applications of Fe_3O_4 nanoparticle with TiO_2 can facilitate the recycling of TiO_2 and also improve its optical behavior significantly. Although direct coating of TiO_2 onto Fe_3O_4 nanoparticles is not favorable, an intermediate layer between the two can maintain the photocatalytic behavior of TiO_2 and magnetic properties of Fe_3O_4. CS is one of the best choices to coat magnetite nanoparticle as Fe_3O_4/CS nanoparticles are frequently used in wastewater treatment applications.

Thus, a ternary system consisting of TiO_2/CS/Fe_3O_4 is expedient due to the unique properties of each individual component. Improved photocatalytic performance can be obtained by optimizing certain parameters like catalyst loading, pollutant concentration and pH of the reaction medium using RSM. The synthesized and optimized composite provides a facile route for the degradation of POP's in wastewater under visible light and with effective recyclability.

CHAPTER 3: METHODOLOGY

This chapter comprised five sections which explain the activities involved in the experimental work conducted in this research. The first section deals with the material and chemicals involved during the experimental procedures. The second part of this chapter detailed the synthesis route adopted to prepare TiO_2/CS/Fe_3O_4 nanocomposites. The third segment discussed the characterization techniques used to explain the physicochemical properties of the nanocomposite. The subsequent sections included the photocatalytic activity and analysis techniques used to elucidate the degradation of ONP.

In this study, TiO_2 was modified by the incorporation of Fe_3O_4 and CS. Initially Fe_3O_4 supported CS were prepared by co-precipitation method, followed by subsequent coating of TiO_2 nanoparticles over Fe_3O_4/CS to develop a ternary system: TiO_2/CS/Fe_3O_4 nanocomposite. To assess the effect of the ratio of TiO_2, CS and Fe_3O_4, six composites were prepared by varying the concentrations of these components. All the synthesized nanocatalysts were characterized to determine their physical and chemical properties using FESEM, HR-TEM, BET, XRD, VSM, FTIR, PL, DRSUV and XPS. The photocatalytic activities of the synthesized composites were evaluated using ONP as the model POP's under visible light and the samples were analyzed by UV-visible spectrophotometer and LC-MS. The overview of this research work is presented in Figure 3.1.

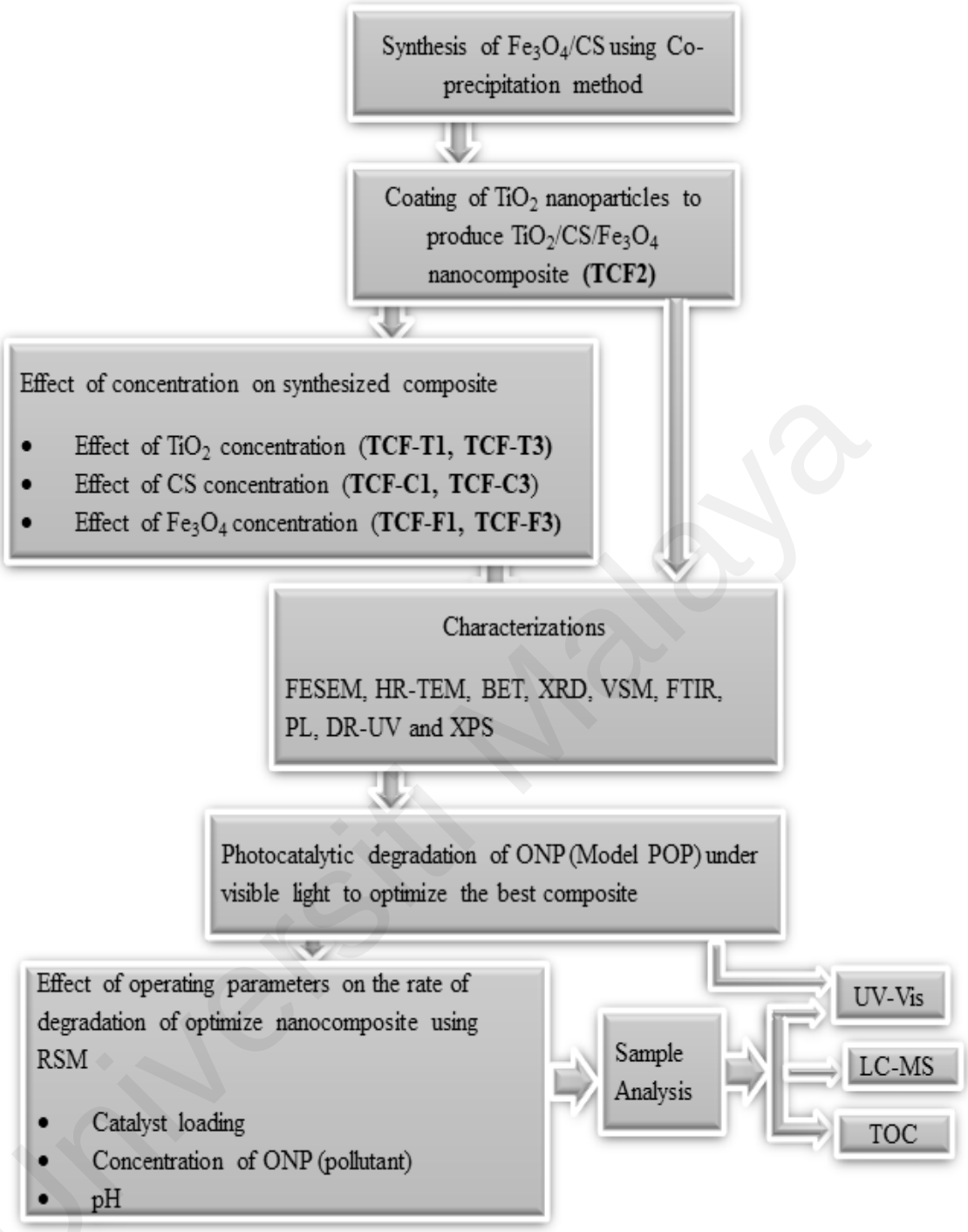

Figure 3.1: An overview of research work

3.1 Materials

Iron (III) chloride hexahydrate, Iron (II) chloride tetrahydrate, acetic acid (100%), absolute ethanol (99.5%), ammonia solution (30%), ONP (2-nitroitrophenol) and acetonitrile were purchased from Merck (Darmstadt, Germany). Titanium (IV) oxide nanopowder (particle size 21 nm) and CS with medium molecular weight were purchased from Sigma Aldrich (Steinheim, Germany). All the chemicals were of analytical grade and used without further purification. Deionized water (18.2 MΩ) was used throughout the experiments. Millipore Milli-Q water used in LC-MS analysis.

3.2 Synthesis of TiO_2/CS/Fe_3O_4 nanocomposite

Synthesis of TiO_2/CS/Fe_3O_4 was carried out in two successive steps. The first step involves the synthesis of Fe_3O_4/CS by co-precipitation and the next step involves the coating of TiO_2 on Fe_3O_4/CS to produce TiO_2/CS/Fe_3O_4 as presented in Figure 3.2.

3.2.1 Synthesis of Fe_3O_4/CS

In a typical synthesis of Fe_3O_4/CS, 0.814g of $FeCl_2.4H_2O$ and 2.028g of $FeCl_3.6.H_2O$ were dissolved in 40 ml of deionized water with continuous stirring for 30 minutes. 0.1g CS in 3% acetic acid solution (20ml) was prepared and added to the above solution and stirred for another 2 hours at room temperature. Then, NH_3 solution was added dropwise with continuous stirring, until the pH of solution became 9-11. The color of solution was initially brown which turns black gradually indicating the formation of Fe_3O_4. The solution was stirred for further 1 hour at 100 ^oC to strengthen the CS-O-Fe cross linking on the surface of Fe_3O_4 nanoparticles. The product (Fe_3O_4/CS) was washed with ethanol and deionized water alternately for several times to neutralize the pH.

3.2.2 Synthesis procedure for $TiO_2/CS/Fe_3O_4$

The washed Fe_3O_4/CS was dispersed in deionized water (50 ml). In another 50 ml of deionized water, TiO_2 nanoparticles was dispersed and then added slowly into Fe_3O_4/CS solution with continuous stirring. The resultant product $TiO_2/CS/Fe_3O_4$ was oven-dried overnight at 60 ^oC.

3.2.3 Synthesis of $TiO_2/CS/Fe_3O_4$ on varying concentration of TiO_2, CS and Fe_3O_4

In order to study the effect of TiO_2, CS and Fe_3O_4 concentration on the formation of $TiO_2/CS/Fe_3O_4$ nanocomposite, six composites were prepared using the same procedure as described in section 3.2.1 and 3.2.2 by varying the amount of TiO_2, CS, and Fe_3O_4. The composite prepared in Section 3.2.2 is denoted as TCF2. Two composites (TCF-T1 and TCF-T3) were synthesized by varying the concentration of TiO_2 nanoparticles. The effect of CS and Fe_3O_4 was also investigated by varying the concentrations of CS and Fe_3O_4 and labeled as TCF-C1, TCF-C3, TCF-F1 and TCF-F3, respectively.

The amount of chemicals used during the synthesis step affects the overall physicochemical properties of the composite, therefore careful consistencies are needed in this step. The amount of chemicals used during the whole synthesis procedure is presented in Table 3.1.

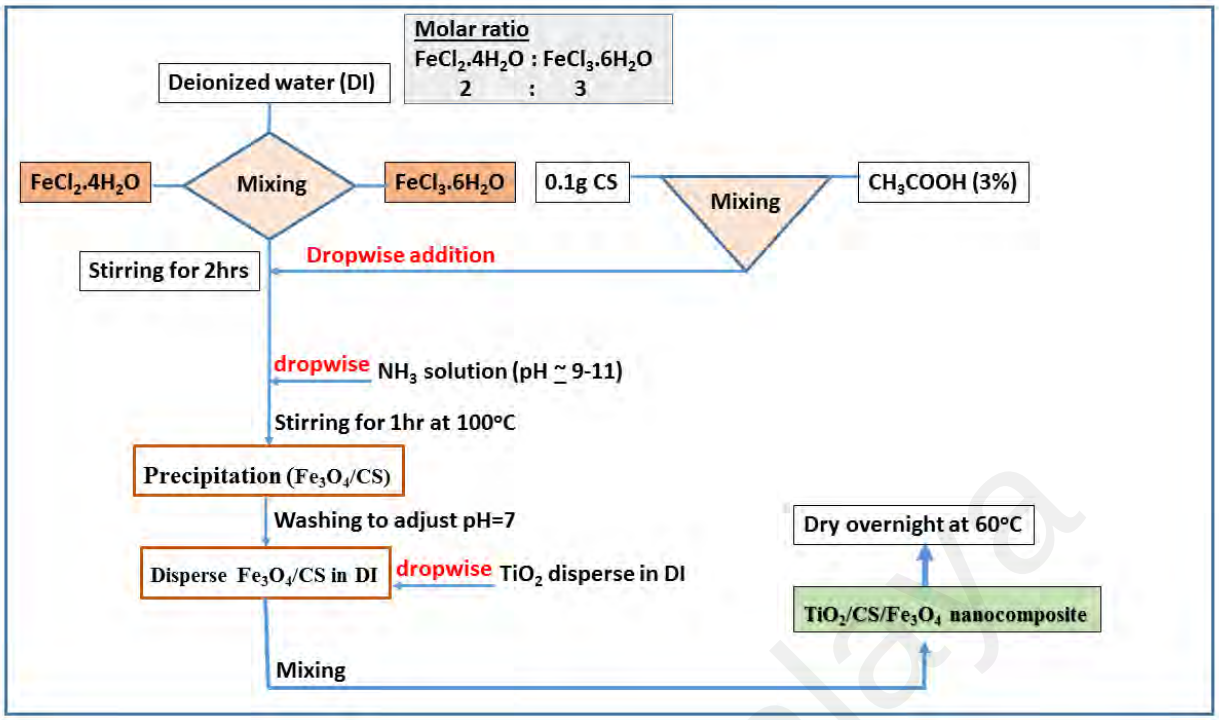

Figure 3.2: Synthesis of TiO_2/CS/Fe_3O_4 nanocomposite

Table 3.1: The amount of chemicals required during synthesis of nanocomposite

Chemicals	TCF2	TCF-T1	TCF-T3	TCF-C1	TCF-C3	TCF-F1	TCF-F3
$FeCl_2.4H_2O$ (g)	0.814					0.408	1.013
$FeCl_3.6.H_2O$ (g)	2.028					1.225	3.040
CS (g)	0.1			0.05	0.15		
TiO_2 nanoparticles (g)	2.829	1.421	4.265				
CH_3COOH	3%						
NH_3 solution	To adjust pH 9-11						

3.3 Characterization techniques

To understand the physico-chemical properties of the synthesized nanocomposite, various techniques were employed including FESEM, HR-TEM (morphology), BET (textural properties, XRD (crystal properties), VSM (magnetic properties), FTIR (chemical structure), PL (recombination rate and defects, DR-UV (optical response) and XPS (surface chemical state). The principle and procedure of each individual analysis are discussed in the subsequent sections.

3.3.1 Field emission scanning electron microscopy (FESEM)

FESEM provides topographical details on the surface of objects. Electron is emitted from field emission gun and then confined and focused into a thin focused, monochromatic beam using metal apertures and magnetic lenses. Different electron detectors are placed in the microscopes to collect signals to generate specimen's image. Compared with convention techniques such as SEM, the FESEM generates much clearer images with 3 to 6 times better spatial resolution.

For FESEM analysis FEI Quanta 450 FEG was used to determine the surface morphology of the composite. Sample was prepared by fixing small amount on carbon tap. A high vacuumed (10 kV) were employed to give the best resolution with magnification from 50 k to 200 k.

3.3.2 Energy dispersive x-ray spectroscopy (EDX)

EDX is an x-ray technique used to identify the elemental composition of materials. EDX systems are attachments to Scanning Electron Microscopy (SEM) or Transmission Electron Microscopy (TEM)) instruments where the imaging capability of the microscope identifies the specimen of interest. The data generated by EDX analysis consist of spectra showing peaks corresponding to the elements making up the true composition of the sample being analyzed. EDX can distinguish all elements in the order of 0.1 percent and is limited to elements having an atomic number greater than boron. The analysis was conducted per area basis. For EDX, a similar sample preparation as FESEM was employed.

3.3.3 High resolution transmission electron microscopy (HR-TEM)

HR-TEM is an imaging mode of the transmission electron microscope (TEM) that has been used widely for crystal structure and lattice analysis in variety of advanced materials on an atomic resolution scale. It can also be used for characterizing point defects, dislocations, grain boundaries stacking faults and surface structures. The instrument used both the transmitted and scattered beams to generate an interference image which is phase contrast image and can be as small as the crystal's unit cell. The instrument consisted of more than one condenser lenses which focus the beam of electron to the sample, objective lens to produce diffraction patterns and intermediates lenses to magnify the image on the screen.

HR-TEM analysis was performed using JEOL JEM-3010. The sample was prepared by dispersing small amount of the composite in ethanol and sonicated in an ultrasonic bath for 10 min at room temperature. A drop of suspension was dropped carefully using a disposable pipette on a 400 square mesh copper grid (3.05 mm) and dried it for 3 days prior to analysis.

3.3.4 Brunner-Emmet-Teller (BET)

BET is an analysis used to study the textural properties of materials such as surface area, pore size, pore volume and pore shape. It is a process of multilayer adsorption utilizing probing gases that do not chemically react with the material to evaluate the adsorption of gas molecules on the solid surface. There are several factors such as temperature, pressure and solid-gas interactions which affect the degree of the adsorption. At the saturation pressure, the sample is removed from the gas environment and the adsorbed gases are released through heating. The released gases are then quantified. The data is presented as BET isotherm, which plots the amount of adsorbed gas with the relative partial pressure. There are 5 types (Type I, II, III, IV and V) of

adsorption isotherms which determine the porosity of the sample. The Brunauer-Emmett-Teller (BET) surface area, porosity and cumulative pore volume was measured using the N_2 adsorption-desorption studies on TriStar II 3020 series, Microactive 2.0.

A 0.3g of sample was dried for 2 h at 60 ºC prior to BET analysis and then placed in a 6 mm glass cell and put in a vacuumed chamber to degas for 6h at 150 ºC to remove any trapped moisture and possible impurities. The range of relative pressure during sample measurement was 0.01- 0.90 P/Po.

3.3.5 X-Ray powder diffraction (XRD)

XRD is used to obtain structural information (crystallinity, crystal phase, ratio, and lattice spacing) of crystalline solid. It is a non-destructive analysis in which a beam of x-ray strikes the crystalline atom, causing the electrons surrounding the atom to oscillate with the same frequency as the incident beam. As atoms are periodically arranged in a crystalline structure, the combining waves formed constructive interference and produce well defined x-ray diffracted beams at various directions while leaving the sample.

XRD analysis was conducted using Bruker-Axs D8 Advance diffractometer. The Bragg's angle was set from 10-80º with step size 0.02º and an acquisition time of 1sec/step. The sample was ground into a fine powder before analysis and then closely packed into a sample holder. High score plus software was used to assess the obtained diffraction patterns and matched with the JCPDS (Joint Committee for Powder Diffraction Standards) standard reference patterns.

Scherrer's equation was employed to determine the crystallite size of nanocomposite as shown in the equation 3.4 (Talat-Mehrabad et al., 2016).

$$\tau = \frac{K\lambda}{\beta \cos\theta} \quad \textbf{(3.1)}$$

Where:

τ is the mean size of the ordered (crystalline) domains;

K is a dimensionless shape factor;

λ is the X-ray wavelength;

ß is the line broadening at half the maximum intensity (FWHM);

θ is the Bragg angle (in degrees).

3.3.6 Vibrating-sample magnetometer (VSM)

VSM is used to determine the magnetic moment of a sample with a very high precision. The basic principle of VSM is based on Faraday's law according to which *an electromagnetic force is generated in a coil when there is a change in flux through the coil*. In VSM, a sample is positioned in appropriately placed sensing coils which cause the sample to undergo sinusoidal motion. This causes magnetic flux changes which induce a voltage in the sensing coils that is proportional to the magnetic moment of the sample.

The magnetic properties of synthesized nanocomposite were measured using a lakeshore 7400 series, Model 7407 with a 7 in. electromagnet vibrating sample magnetometer. The analysis was conducted at room temperature in the field of ±10 kOe.

3.3.7 Fourier transform infrared (FTIR) spectroscopy

FTIR spectroscopy was used to determine the functional groups and the type of chemical linkages between TiO_2, CS and Fe_3O_4. The IR spectrum is recorded by passing IR radiation through a sample and measured the absorption frequencies that correspond with the structural properties of molecules. The different functional groups attached to a molecule produce characteristics absorption in IR spectrum. Perkin Elmer spectrum 400FTIR/FT-FIR Fourier transform spectrometer was used for IR spectral analysis. A small amount of sample was ground and placed on sample holder and the IR spectrum is

generated within the range of 450-4000 cm^{-1}. For chemical interpretation the region of most consideration is the mid-infrared (4000-400cm^{-1}) that determines changes in vibrational energies within the molecules. In this technique the samples is examined directly in the solid or liquid state without further preparation, hence speeding the sample analysis.

3.3.8 Photoluminescence spectroscopy (PL)

PL is a non-destructive test used to investigate the electronic structure (both intrinsic and extrinsic) of a material by photon absorption-emission process. The PL spectrum is widely employed to understand the mobility of charge carriers (electrons and holes) and the intrinsic defects. PL measurements were carried out using Reinishaw InVia Raman spectroscope with excitation wavelength of 325nm for recording PL spectra and excitation source of He-Cd laser. The sample was ground into fine powder prior to analysis.

3.3.9 UV-vis Diffuse reflectance spectroscopy (UV-vis DRS)

UV-vis diffuse reflectance spectroscopy is used to determine the optical properties of a material (liquid and solid) by quantifying the amount of absorbed and scattered light. The sample is positioned in between a light source and a photodetector and the difference in the light intensity before and after passing through the sample is measured and compared at each wavelength to determine its absorption spectrum.

DRS were recorded on Shimadzu UV-2700 UV-vis Spectrometer and the measurements were done in wavelength range of 200-800 nm. The samples were ground and then placed in quartz cell evenly before putting into the spectrometer. Before carrying out DRS measurement for the samples, a reference spectrum was also been taken by using barium sulfate. The band gap of the sample was determined by *Tauc plot*. A Tauc plot is

one of the methods for determining the optical band gap in semiconductors in which the optical band gap can be calculated by the Tauc equation. The Tauc's equation is as follows:

$$\alpha = \frac{(hv-Eg)\gamma}{hv} \quad \textbf{(3.2)}$$

Where, α is the linear absorption coefficient of the material, hν is the energy of photon, A is a proportionality constant and γ is a constant depending on the band-gap nature; γ = 1/2 for direct band gap and γ = 2 for indirect band gap (Mansoor et al., 2015).

3.3.10 X-ray photoelectron spectroscopy (XPS)

XPS is a powerful surface analysis technique to depict the surface chemical state of a material from 1 to 12 nm in depth. It can identify the chemical composition and bonding between different elements excluding hydrogen and helium.

In XPS, the material is irradiated with X-rays to excite the electrons of an element into the vacuum state. These electrons hold information about elemental composition, electronic structure, chemical oxidation state and binding energy of the sample under investigation. In a vacuum region, the electron analyzer produces an energy spectrum of intensity versus binding energy. Every energy peak in the spectrum corresponds to a specific element. Hence the surface composition and the electronic environment can both be determined.

The surface chemical state was evaluated by X-ray photoelectron spectroscopy using ULVAC-PHI Quantera II with a 32-channel Spherical Capacitor Energy Analyzer under vacuum (1 x 10^{-6} Pa) using Monochromated A1 Kα radiation (1486.8 eV) and natural width of 680 meV. The carbonaceous C 1s line (284.6 eV) was used as a reference to calibrate the binding energies.

3.4 Photocatalytic degradation experiments

3.4.1 Reactor setup and photocatalytic activity test

Photocatalytic reactions are conducted in a customized reactor provided with LED (light emitting diodes) spot light (30W) (Figure 3.3). The LEDs offers several advantages including a new source of "tunable" approximately monochromatic light, long lifetime, and efficient electricity to light conversion (little heating). For the constant supply of oxygen, the reactor was provided with an air pump.

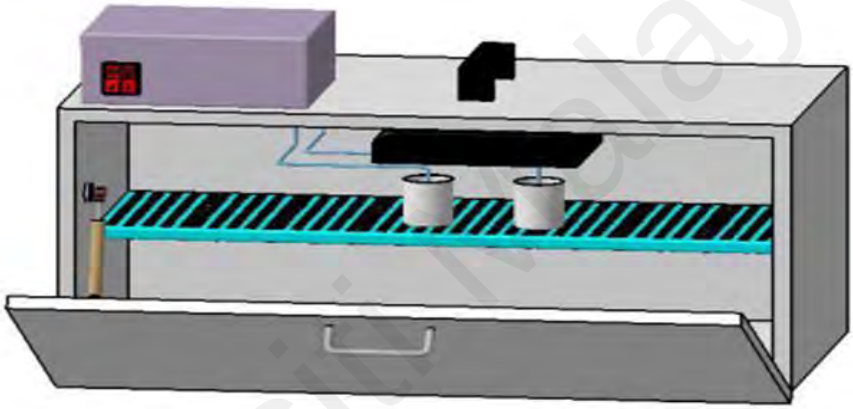

Figure 3.3: Schematic diagram for photocatalytic reactor setup

A 30-ppm stock solution of ONP was prepared by dissolving 30 mg ONP in 1 L of deionized water. The solution is kept for stirring in darkness for 24 h then stored away from direct sunlight in a cool and dry place. Furthermore, four concentration of ONP were prepared (10, 20, 40 and 50 ppm) by using stock solution and utilized for calibration. The intensity of light absorption and maximum wavelength (lambda max) of ONP was identified and verified by using UV-Vis spectrophotometer.

To evaluate the photocatalytic performance, a preliminary experiment was first conducted to optimize the best composite by using a fix amount of composite (0.01g), ONP concentration (30 ppm) and natural pH. The selected best composite was further

optimized based on operating parameters such as catalyst loading, pollutant concentration and pH using RSM.

In a typical experiment (design by RSM), a certain amount of TiO_2/CS/Fe_3O_4 composite was added into 100 mL of ONP with a known concentration. The pH of the solution was adjusted to the desired level using 0.1 M HCl or 0.1 M NaOH. The solution was stirred for 30 min in the dark to attain adsorption–desorption equilibrium between TiO_2/CS/Fe_3O_4 composite and ONP substrate before irradiation. Air was bubbled into the reaction medium to maintain a constant supply of oxygen. The aliquot was immediately filtered by using PES 0.45 μm Millipore Millex filter after irradiation to remove catalyst particles. The concentration of ONP in the aliquot was determined by a UV-Vis spectrophotometer.

3.4.2 Response surface methodology (RSM) and experimental design

To standardize the process and study the effect of operating parameter such as catalyst loading, initial ONP concentration and pH on the rate of degradation, experiments can be designed using RSM technique. RSM is a multivariate statistical tool for designing experiments and developing empirical models where a response or set of responses are affected by operational parameters. Using RSM, the optimal experimental conditions can be determined precisely and with minimum labors by investigating the interactive effects of operating parameters (Mun et al., 2015a).

The central composite design (CCD) was used to investigate the combined effect of three operation parameters, namely TiO_2/CS/Fe_3O_4 dosage, ONP concentration and initial solution pH that yield optimum degradation rate of ONP. Other factors such as temperature, light intensity and oxygen supply were held constant. This model was chosen because it is appropriate for fitting quadratic surface with a minimum number of experiments and also interaction between the parameters is possible (Arami-Niya et al.,

2012). The steps that were followed for the CCD are presented in Figure 3.4. The ranges and levels of the operational parameter were tabulated in Table 3.2. The statistical analysis was carried out by Design Expert V.6.0.8 (Stat-Ease Inc.,USA) to examine the interaction between the process parameters with a total of 20 runs, including six replications at the center points.

Table 3.2: Operational parameter and experimental ranges for ONP degradation

Parameter	Unit	Symbol	Range		
			-1	0	+1
Catalyst loading	g/100mL	A	0.02	0.03	0.04
Initial concentration of Pollutant (ONP)	ppm	B	30	40	50
pH		C	3	6	9

3.5 Chemical Analysis

3.5.1 pH Adjustment

To adjust the pH of ONP solution, NaOH (0.1M) and HCl (0.1M) were used and the pH was monitored by pH meter of Horiba Laqua series (Model: F-71G).

3.5.2 ONP degradation analysis

Degradation of ONP by TiO_2/CS/Fe_3O_4 nanocomposite was studied using UV-vis spectrophotometer (Shimadzu - UV-3101PC) at the wavelength of maximum absorption (278 nm) detected by Uv-Vis spectrophotometer. The degradation (%) of ONP was calculated using the Equation 3.3.

$$\text{Degradation efficiency (\%)} = \left(\frac{C_o - C}{C_o}\right) \times 100 \quad \textbf{(3.3)}$$

Where Co is the initial concentration of ONP and C is the concentration after photo-irradiation.

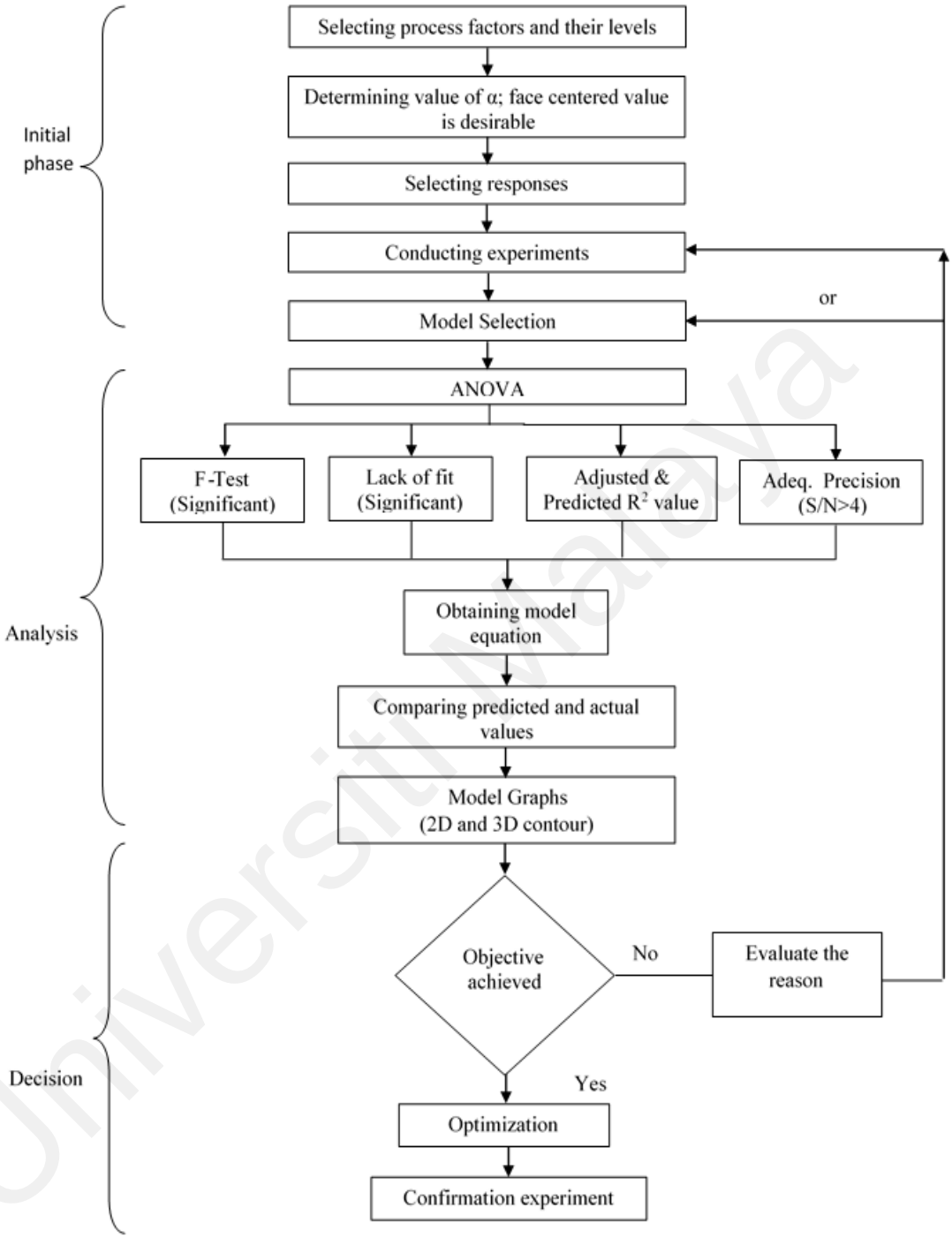

Figure 3.4: Flow chart for central composite design

3.6 Reaction Kinetics

For photocatalytic degradation kinetics of ONP in the presence of TiO_2/CS/Fe_3O_4, ONP solution was withdrawn after every 30 minutes of interval and its concentration was measured as a function of time. The collected results were analyzed by first order kinetic model (Equation 3.4).

$$\ln \frac{C_o}{C} = kt \quad \textbf{(3.4)}$$

Where, Co and C are the initial and final concentrations respectively. The plot of concentration data gave a straight line.

3.7 Catalyst Reusability study

The composite samples were collected using magnetic separation after photocatalytic degradation experiments. The composite sample was washed several times with distilled water and dried in oven at 60 ºC for 12h. The dried composite sample was used for the degradation of ONP and the degradation efficiency was monitored up to four cycles.

3.8 Mechanistic studies

The liquid samples collected during photocatalytic degradation experiments **we**re further analyzed to develop a pathway by intermediate determination by LC-MS using Triple Quadrupole LC/MS System (Agilent tachnologies) in both positive and negative ionization modes. The triple quadrupole mass spectrometer increases the sensitivity and specificity at lower detection limits. An agilent zorbax C-18 column (4.6 x 250 mm, 5 µm) at 20 ºC was used as separation column for intermediate product (IMP) formed during degradation of ONP. Two separate mobile phase acetonitrile and 0.1 % phosphoric acid in the ratio of 85:15 respectively was used with the injection volume of 5 µL and the flow rate were adjusted at 0.4mL/min.

3.9 Total Organic Carbon (TOC) Analysis

Total organic carbon (TOC) analyzer is a useful tool to determine the organic content in the given sample. The TOC analysis was performed by Shimadzu TOC-L (TOC-L CPN, TNM-L, SSM-5000) analyzer. The operating principle of TOC measurement is based on heated persulfate wet oxidation technique, which maintains the low system background essential for high sensitivity TOC measurements. The sample was injected into the combustion chamber through carrier gas (Air zero) and the concentration of TC in the sample was obtained. Afterward, IC content of the sample was obtained through nitric acid oxidation of inorganic content. Thus, the TOC and its removal efficiency for a specific sample was calculated according to the equations given below:

$$TOC = TC - IC \quad \textbf{(3.5)}$$

$$\%TOC = [1 - \frac{TOC_f}{TOC_i}] \quad \textbf{(3.6)}$$

CHAPTER 4: RESULTS AND DISCUSSION

In this chapter, the characterization results of all the TCF nanocomposites are presented and the photocatalytic activity of composite samples toward ONP degradation is detailed. The results are presented in four main sections for better understanding and for an ideal flow of the current study. The first section comprises the characterization results of the synthesized Fe_3O_4/CS and TiO_2/CS/Fe_3O_4 (TCF2) nanocomposites. The second section detailed results regarding the effect of concentration of TiO_2, CS and Fe_3O_4 on the physicochemical and photocatalytic properties of TCF nanocomposites. The effects of operating parameter on the rate of degradation of ONP by using RSM are explained in the third section. The last section demonstrates the possible intermediates and the proposed degradation pathway of ONP.

4.1 Synthesis of TiO_2/CS /Fe_3O_4

4.1.1 Morphological and textural properties

FESEM analysis was performed to analyze the morphology and the presence of TiO_2 shell on Fe_3O_4/CS core. SEM micrograph of TCF-2 in comparison to TiO_2, Fe_3O_4 and Fe3O4/CS are presented in the Figure 4.1. Well distributed TiO_2 nanoparticles were clearly seen in Figure 4.1(a). Fe_3O_4 nanoparticles (Figure 4.1b and c) are easily distinguishable from TiO_2 nanoparticles in the SEM micrographs. However, TiO_2 nanoparticles with uniform size are clearly observed in Figure 4.1(d), which indicate that they covered the Fe_3O_4/CS core in TCF2 composite system. This showed the comprehensive covering of TiO_2 over Fe_3O_4/CS shell to form a well-defined core-shell structure.

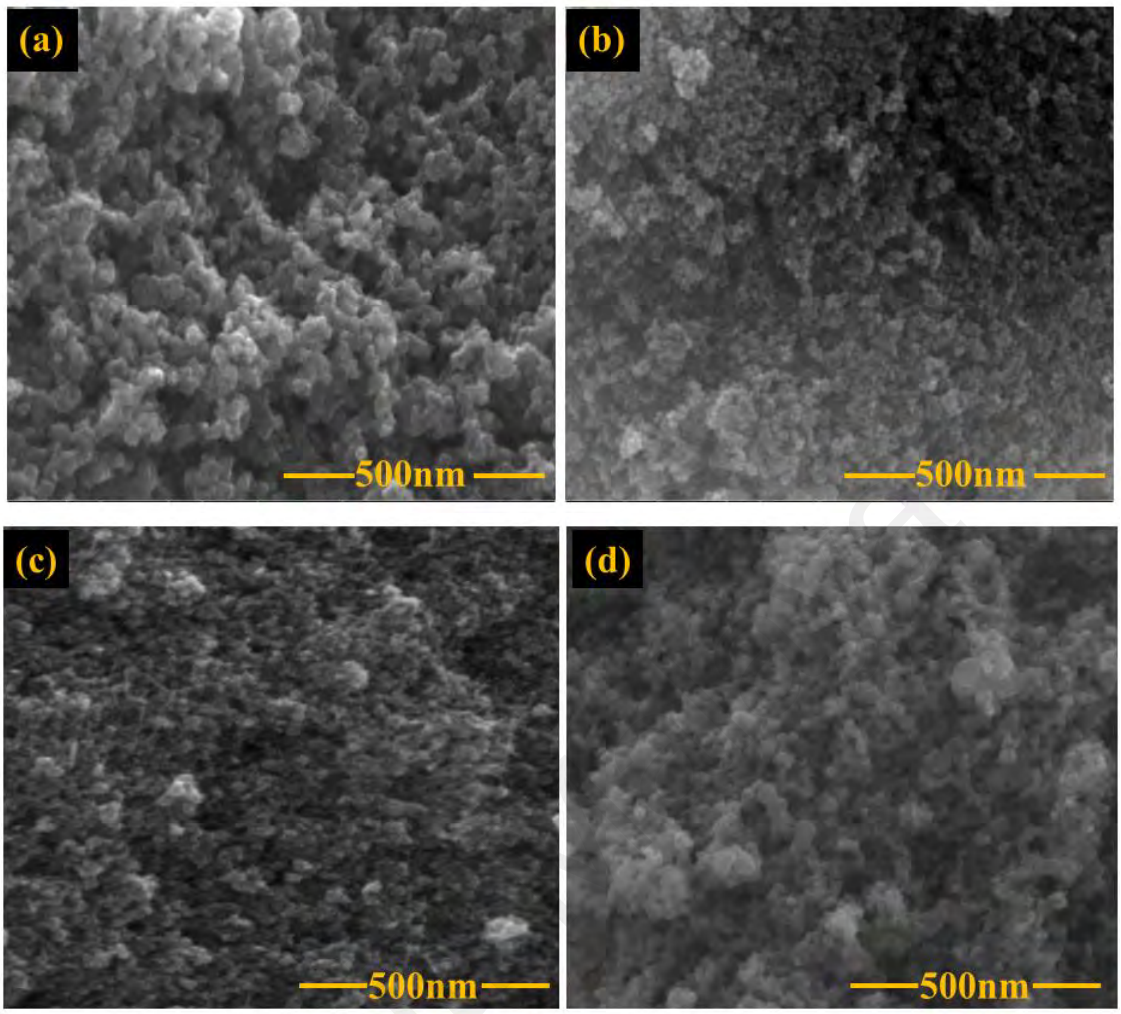

Figure 4.1: High magnification FESEM images of (a) TiO_2 (b) Fe_3O_4(c) Fe_3O_4/CS and (d) TCF2 nanocomposite

To determine the elemental composition of TCF2 nanocomposite, EDX analysis was employed. Due to certain factors such as surface, specimen and elemental features, the EDX data is not absolutely reliable but still the technique can provide a reasonable and realistic elemental composition of inorganic materials particularly for insoluble inorganic materials like TiO_2 (Yoo et al., 2016). The bright field images of O K-edge, Ti K-edge, C K-edge and Fe K-edge are presented in Figure 4.2(a), in which Ti, O, Fe and C signals are clearly seen throughout the nanocomposite. By taking the spot on three different areas of the sample, the weight percentage of Ti, O, Fe and C of the TCF2 nanocomposite were obtained directly from the EDX data and presented in Figure 4.2(b).

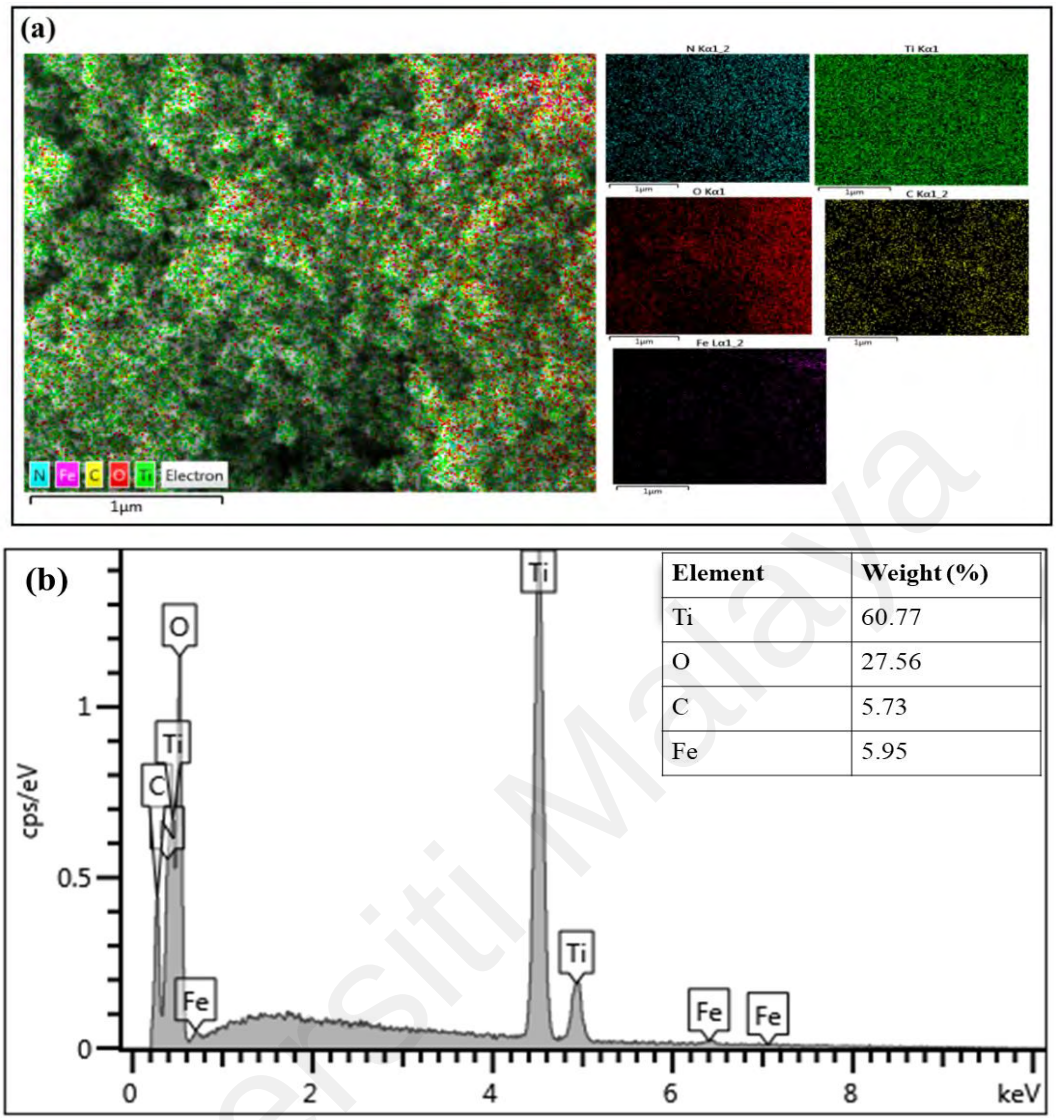

Figure 4.2: (a) Elemental mapping and (b) EDX spectrum and composition of TCF2 nanocomposite

The crystal structure and lattice spacing of TiO_2 and TCF2 nanocomposite were examined by HR-TEM. In Figure (4.3a), tetragonal TiO_2 nanoparticles are clearly seen and the assessed d-spacing is 0.35 nm which indicate the presence of anatase (101) phase of TiO_2 (Figure 4.3b). Well dispersed TiO_2 nanoparticles can be observed throughout the composite surface (Figure 4.3c), with the tetragonal TiO_2 nanoparticles covering the dark Fe_3O_4 core, indicating the successful synthesis of core shell TCF2 nanocomposite. The lattice fringes in Figure 4.3 (d) are noticeably visible and the

assessed d-spacing was found to be 0.35 nm corresponding to (101) anatase phase of TiO_2. In addition to anatase, another d-spacing matches Fe_3O_4 (311) plane was observed at 0.25 nm indicating the presence of Fe_3O_4 in nanocomposite. The estimated average particle size of TCF2 nanocomposite was found to be 24.3 nm well indexed with average crystallite size of TCF2 presented in XRD results.

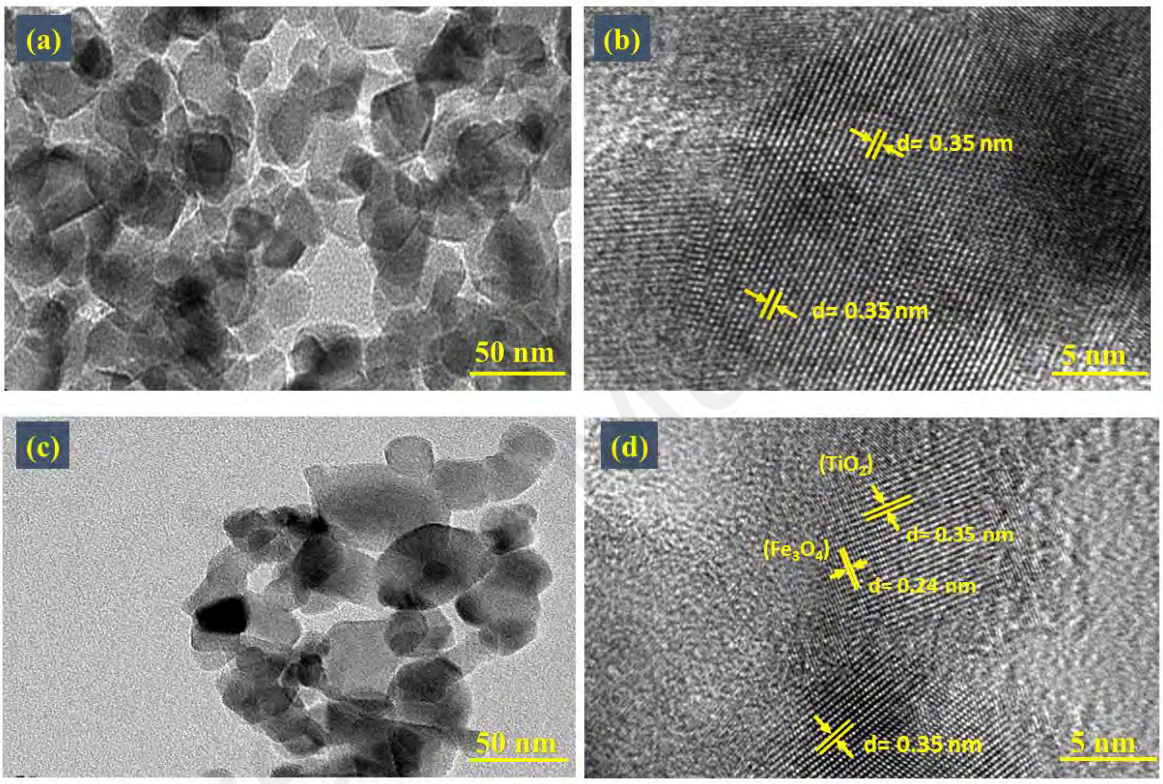

Figure 4.3: HRTEM images of (a) TiO_2 and (c) TCF2 nanocomposite. Lattice fringes and the assessed d-spacing of (b) TiO_2 and (d) TiO_2 and Fe_3O_4 in TCF2 nanocomposite

Nitrogen adsorption-desorption isotherm was measured to determine the specific surface area and porosity of as prepared TCF2 nanocomposite. The isotherm of TCF2 nanocomposite in comparison to TiO_2, Fe_3O_4 and Fe_3O_4/CS is presented in Figure 4.4. It is evident from Figure 4.4 that all samples exhibit type IV adsorption-desorption linear isotherms, which is characteristic of materials with mesoporosity indicating the presence of mesopores (2-50 nm) (Wang et al., 2012). However, the shape of hysteresis loop in Fe_3O_4 and Fe_3O_4/CS is H1, containing nearly vertical and parallel adsorption

and desorption branches comprising cylindrical pores (Condon, 2006). The coating of TiO_2 layer on to Fe_3O_4/CS core changed the hysteresis from H1 to H3 in TCF2 (Figure 4.4d) as TiO_2 possess H3 hysteresis loop (Figure 4.4a). The H3 hysteresis loop has sloping adsorption and desorption branches with characteristic slit like pores. This alteration in morphology and pore shape in TCF2 nanocomposite from cylindrical to slit improves its properties (Samsudin et al., 2016). The presence of slit like mesoporous (IV-H3) in TCF2 in contrast to cylindrical pores (Fe_3O_4/CS) is reported to facilitate the transportation of ionic species (reactant and product) through the interior space and facilitates overall photocatalytic process (Tu et al., 2013).

Table 4.1 presents the BET surface area, pore volume and porosity of synthesized composite in comparison to TiO_2, Fe_3O_4 and Fe_3O_4/CS which shows that there is significant decrease in surface area of TCF2 because of TiO_2 coating over Fe_3O_4/CS. These are observed to be 66.9 m^2/g and 133.8 m^2/g for TCF2 and Fe_3O_4/CS respectively. This decrease in surface area in TCF2 is well indexed with HRTEM and XRD results, which show increase in particle size because of coating of TiO_2 shell on Fe_3O_4/CS core. However, these results are not consistent for TiO_2 which shows small crystallite size than TCF2 and still shows the lower surface area (49.96 m^2/g) than TCF2. This could be due to the CS contributing to the larger surface area as reported in the literature that the unsmooth, granular surface of CS leads to higher specific surface area (Ing et al., 2012; Zhang et al., 2011). This is consistent with the fact that the coating of CS over Fe_3O_4 significantly enhances its surface area and will remain higher after coating of TiO_2 layer.

The hysteresis loop in TCF2 shifts to a higher relative pressure with increase in its area, which causes an increase in the average pore size and pore volume (Wang et al., 2012) as evident from Table 4.1.

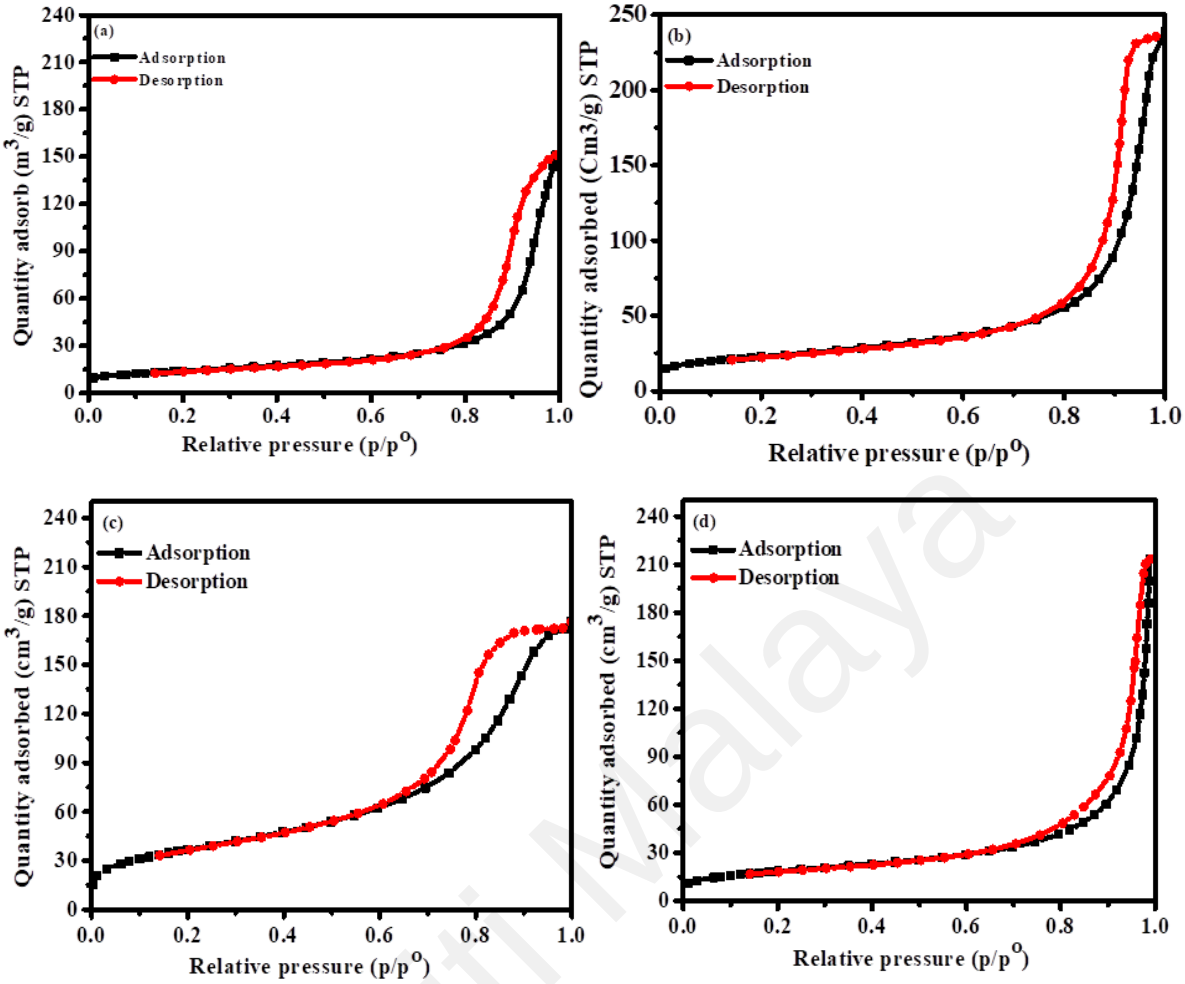

Figure 4.4: Nitrogen adsorption-desorption linear isotherm plot of (a) TiO_2 (b) Fe_3O_4 (c) Fe_3O_4/CS and (d) TiO_2/CS/Fe_3O_4

Table 4.1: Crystallite size, BET surface area, pore volume and average pore width of Fe_3O_4/CS and core-shell TiO_2/CS/Fe_3O_4 nanocomposite

Sample	Crystallite size (nm)	BET surface area (m^2/g)	Pore volume (cm^3/g)	Average pore width (nm)
TiO_2	20.90	49.96	0.23	17.51
Fe_3O_4	16.86	81.34	0.37	16.87
Fe_3O_4/CS	14.53	133.78	0.27	7.12
TCF2	24.50	66.93	0.33	20.19

4.1.2 Crystal properties

XRD analysis was conducted for phase identification, phase mixture, lattice parameters and crystallite size of the synthesized nanocomposite TCF2. Figure 4.5 shows the X-ray

patterns of TCF2 nanocomposite in comparison to TiO_2, Fe_3O_4 and Fe_3O_4/CS. As the TiO_2-P25 used in this study is a mixture of anatase and rutile phases, the prominent diffraction patterns of TiO_2 (Figure 4.5a) were indexed at 25.4, 27.5, 38.7, 48.2, 55.2° which correspond to (101), (110), (211), (002), (112) crystallographic planes respectively (JCPDS 01-073-1764). Similarly, the diffraction patterns of Fe_3O_4 (Figure 4.5b) were indexed at 30.3, 35.7, 43.5, 57.4, 63°. These peaks correspond to (220), (311), (400), (511), and (440) crystallographic planes of magnetite (Fe_3O_4), respectively (JCPDS 96-900-5842). Furthermore, the absence of any peaks in the range of 2θ angle of 20° to 30° which corresponds to maghemite additionally verified the purity magnetite. Figure 4.5c also shows the presence of Fe_3O_4 as all the observed diffraction peaks indicate the presence of Fe_3O_4.

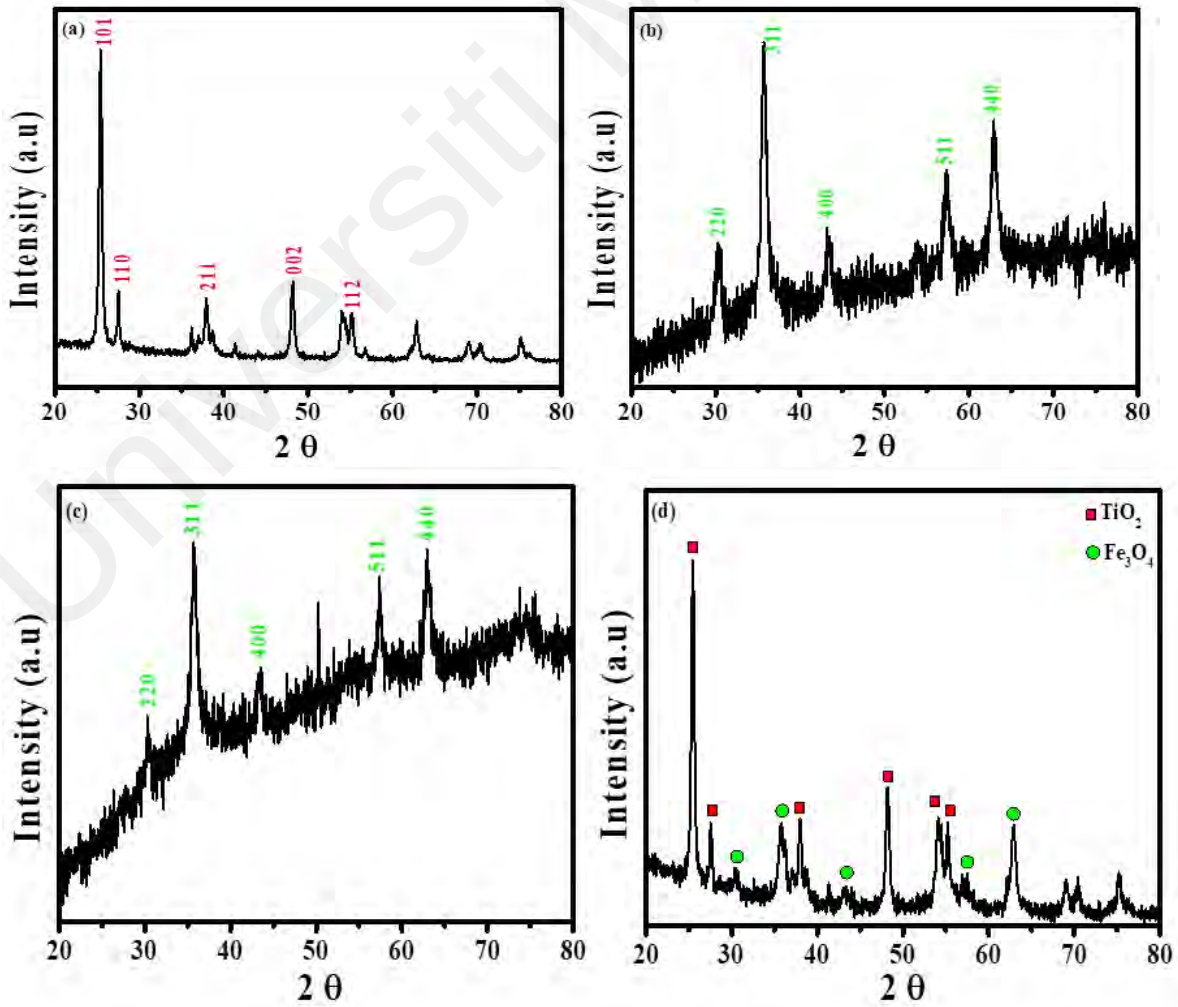

Figure 4.5: XRD patterns of (a) TiO_2 (b) Fe_3O_4 (c) Fe_3O_4/CS and (d) TCF2

All the diffraction peaks in TCF2 nanocomposite were observed at 25.4, 27.5, 30.4, 35.7, 37.9, 48.2, 55.2, 57.2, and 62.9° corresponds to the presence of Fe_3O_4 and TiO_2 (Figure 4.5d). The average crystallite size for each sample was calculated using Scherrer's equation [$D = (K\lambda)/\beta\cos\Theta$)] and found to be 20.9 nm, 16.8, 14.5 nm and 24.5 nm for TiO_2, Fe_3O_4, Fe_3O_4/CS and TCF2 nanocomposites respectively. The gradual increase in average crystallite size from Fe_3O_4/CS to TCF2 might be due to the coating of TiO_2 layer on to Fe_3O_4/CS. The average crystallite size of TCF2 is also in agreement with the average particle size calculate through HRTEM analysis (24.3 nm).

4.1.3 Magnetic properties

The magnetic property of the TiO_2/CS/Fe_3O_4 nanocomposite is one of the attractive features which distinguishes them from conventional catalysts. Figure 4.6 shows the hysteresis measurement in applied field ranging from -10 to 10 kOe at room temperature. The Ms of Fe_3O_4 nanoparticle synthesized by co-precipitation method is 67.87 (Figure 4.6a) emu/g. However, for Fe_3O_4/CS which was also synthesized by co-precipitation method in one pot is 46.45 emu/g (Figure 4.6b). The calculated Ms for TCF2 nanocomposite is 21.462 emu/g (Figure 4.6c) and this gradual decrease in magnetization is due to the successive coating of non-magnetic CS and TiO_2 layer on to the surface of Fe_3O_4 (Mohseni-Bandpi et al., 2015; Ahmed et al., 2014). This reduction in magnetization is additional evidence that CS and TiO_2 are successfully coated on Fe_3O_4 surface. Moreover, the results are also in agreement with coercivity (Hci) of TCF2 (2.683 G) which is lower than reference Fe_3O_4 (8.617 G) (Table 4.2). These results suggest that coated CS is bonded onto the surface of the Fe_3O_4 and TiO_2 nanoparticles and successfully served as a linker between these two materials, which was further confirm through FTIR and XPS results. The Ms of TCF2 nanocomposite indicated that it can be easily separated from the reaction solution using external

magnetic field. The recovery of nanocomposite was experimentally proven by the fact that they can be attracted by a conventional magnet placed close to the reaction vessel within three to five second as shown in the inset of Figure 4.6. This is economically suitable for the treatment of wastewater on large scale.

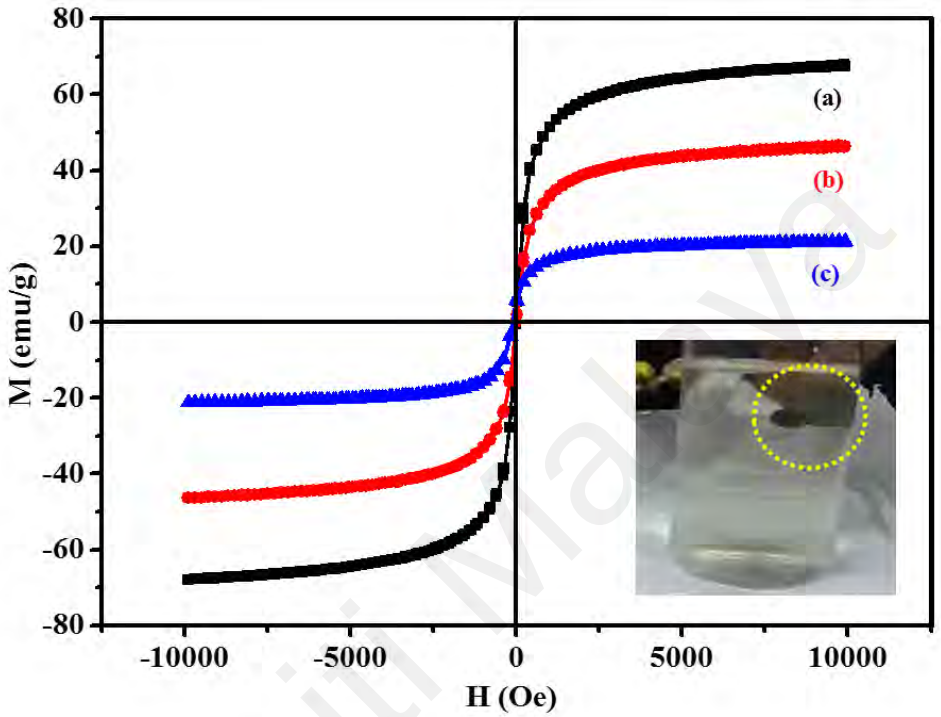

Figure 4.6: VSM curves of (a) Fe_3O_4, (b) Fe_3O_4/CS and (c) TCF2 nanocomposite

Table 4.2: Magnetic properties of Fe_3O_4, Fe_3O_4/CS and TiO_2/CS/Fe_3O_4 nanocomposite

Sample	Saturation magnetization (Ms) emu/g	Coercivity (Hci) G	Magnetic remanence (Mr) emu/g
Fe_3O_4	67.88	8.62	1.35
Fe_3O_4/CS	46.45	5.36	0.53
TCF2	21.46	2.68	0.14

4.1.4 Chemical composition

To confirm the chemical composition of synthesized core-shell nanocomposite, FTIR spectra of TCF2 with reference to the bare TiO_2, Fe_3O_4 and Fe_3O_4/CS were obtained and

presented in Figure 4.7. In the case of bare TiO_2 (Figure 4.7 a), three prominent peaks are observed at 680, 1628 and 3408 cm^{-1}. The peak at 680 cm^{-1} is associated with metal-oxygen (Ti-O) stretching vibrations (Chen et al., 2012). The peak at 1628 cm^{-1} may refers to stretching vibration of O-H group and bending vibration of TiO_2-OH and the prominent peak at 3408 cm^{-1} reflects the stretching vibrations of O-H groups. Similarly, in the case of Fe_3O_4 (Figure 4.7b), prominent peaks are observed in the range of 581, 1631, 3419 cm^{-1}, corresponding to the presence of Fe-O stretching vibrations and the stretching vibrations of OH groups respectively (Du et al., 2014; Chen et al., 2012).

According to the literature, metal oxides show almost the same IR spectra. However, the variation in IR spectra of Fe_3O_4/CS (Figure 4.7c) is due to the coating of CS layer onto the Fe_3O_4 nanoparticles. The insertion of CS induced more absorption bands in the IR spectra of Fe_3O_4 and TCF2. The IR spectrum of TCF2 is almost consistent with reference spectra, however, a variation in the absorption bands is clearly observed (Figure 4.7d). In TCF2, the bands centered at 680cm^{-1} are associated with metal-O stretching vibrations (Chen et al., 2012) which confirmed the presence of Fe-O and Ti-O bonds. The IR absorption band in the range of 1070 cm-1 and ~1391 cm^{-1} corresponds to C-H bending vibrations of CH_2 group of CS (Kumirska et al., 2010). The peak at 1628cm^{-1} is assigned to characteristic N-H scissoring from primary ammine due to the presence of free amino groups in CS (Chen et al., 2012; Unsoy et al., 2012). The peak (1631 cm^{-1}) can also be produced due to stretching vibrations of O-H groups and from the bending vibrations of Ti-OH (Afzal et al., 2017). The small peak around 1459 cm^{-1} is an indication of surface absorb (physisorb) nitrogen due to the presence of NH_2 groups of CS in Fe_3O_4/CS. However, this was not noticeable in TiO_2/CS/Fe_3O_4. This might be due to the strengthened interactions between the constituents in the TCF2 composite than Fe_3O_4/CS. The IR bands at 2856cm^{-1} and 2921cm^{-1} are due to the stretching vibrations of -CH_2 groups in CS (Du et al., 2014). A prominent peak at 3408

cm^{-1} reflects the overlapping of the stretching vibrations of N-H and O-H groups (Du et al., 2014; Chen et al., 2012).

The intensity of peaks in the range of 1390, 1450, 2850 and 2920 cm^{-1} which corresponds to the presence of CS is low for TiO_2/CS/Fe_3O_4 in comparison to Fe_3O_4/CS. This lowering in peak intensity can be ascribed to the less availability of free OH and NH_2 groups of CS and their engrossment in bonding with Metal oxide (TiO_2 and Fe_3O_4) network. Hence, these groups are behaving as coordination and reaction sites for the adsorption of organic species for wastewater treatment (Zainal et al., 2009).

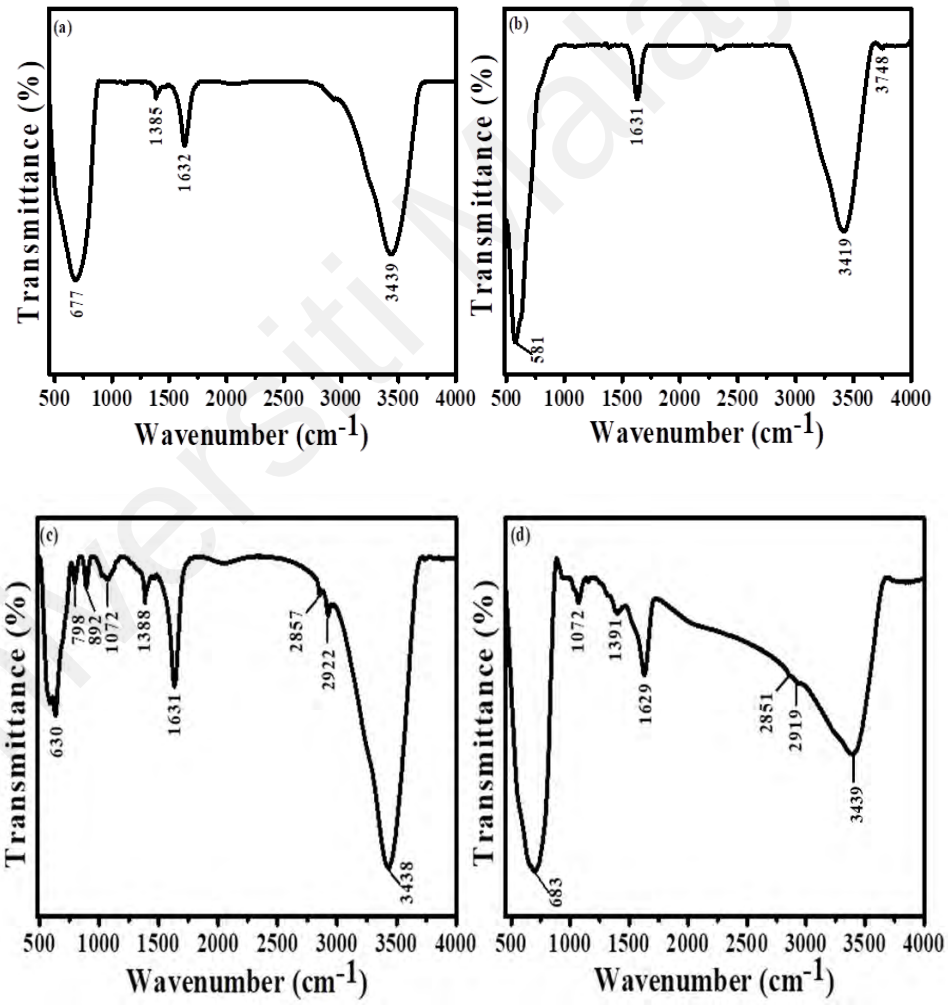

Figure 4.7: FTIR spectra of (a) TiO_2, (b) Fe_3O_4, (c) Fe_3O_4/CS and (d) TCF2 nanocomposite

4.1.5 Optical properties

PL emission spectroscopy was utilized to appraise the separation competency of charge carriers resulting from UV and Visible light illuminations. The intensity of PL spectra is associated with the recombination rate of the photo-induced electrons and holes (Zha et al., 2015). TiO_2, an indirect band gap semiconductor, generates a broad visible PL under UV light irradiation (Samsudin et al., 2015c), constituting three kinds of physical origins: surface defects, self-trapped excitons and oxygen vacancies (Stefan et al., 2014).

The PL emission spectra of TCF2 in contrast to TiO_2 are depicted in Figure 4.8. Both samples display distinguished PL peaks at 443, 494, 521 and 663 nm. However, peak broadening with declined PL intensity was observed in TCF2 nanocomposite. The broad PL bands at a given excitation intensity consists of multiple bands (Kaplan et al., 2016). In the case of TCF2, broad absorption occurred at 393 nm, corresponding to the Eg of TiO_2 anatase phase (Chen et al., 2011). The PL peak at 443 and 494 nm are due to the surface state defects and different intrinsic defects in the TiO_2 lattice such as oxygen vacancies, titanium vacancies and interstitial defects. These surface states are possible due to the interaction of TiO_2 and Fe_3O_4 (Stefan, 2014). A green emission at ~521 nm corresponds to donor-acceptor recombination or transition from CB to oxygen antisites (surface defects and oxygen vacancies) (Memesa et al., 2011; Samsudin et al., 2016). The PL peak at 663 nm represents red PL which is the migration of trapped electron (0.7eV-1.4eV) under CB to VB holes (Samsudin et al., 2015b). It is obvious from the PL spectra that the peak intensity of TCF2 is significantly decreased which revealed the decreased in recombination rate and enhanced photocatalytic activity of the synthesized core-shell nanocomposite (Jin et al., 2016).

Previous literature reported that the formation of such heterostructure and coupling of semiconductors leads to increase in charge separation, increase transport and decrease rate of recombination. Furthermore, band edge position also has attraction for these charge carriers which facilitate the charge separation. The holes accumulate on to the VB of TiO_2 because of the less positive band edge and likewise electrons accumulate near the CB of Fe_3O_4 because of the positive band edge (negative for TiO_2). This will ultimately improve charge separation and decreased recombination (Kumar et al., 2016). Furthermore, the decreased PL intensity and corresponding recombination rate in TCF2 compared to bare TiO_2 could also be explained in terms of energy level theory. As the energy level of Fe^{3+}/Fe^{2+} are closer to the energy level of TiO_2 (Ti^{4+}) CB and the energy level of Fe^{3+}/Fe^{4+} are closer to the energy level of TiO_2 (Ti^{4+}) valence band, the Fe^{3+} are therefore able to capture e^- as well as h^+ and reduces the e^-– h^+ recombination of TiO_2 (Li et al., 2016; He et al., 2008).

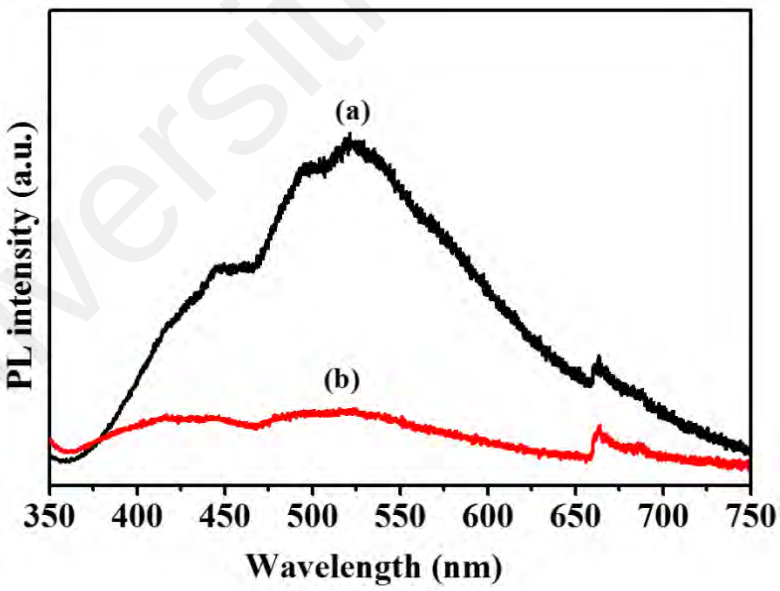

Figure 4.8: PL spectrum of (a) TiO_2 and (b) TCF2 nanocomposite

UV-vis diffuse reflectance spectra were used to evaluate light absorption and band gap of the catalyst (López & Gómez, 2012). Figure 4.9 shows the ultraviolet visible (UV-Vis) absorption spectra of TCF2 in comparison with TiO_2, Fe_3O_4 and Fe_3O_4/CS. The

absorption spectra of TiO_2 (4.9a) show intense transition in the UV region, thus indicating that the intrinsic band gap absorption of TiO_2 is due to the electronic transition from valence to CB (O2p → Ti 3d). The valence band mainly consists of O 2p state and a few Ti 3d states, indicating the strong p-d hybridization between O 2p and Ti 3d states which form the bonding state in the valence band region. Moreover, the CB is primarily consisting of Ti 3d states, mixed with a few O2p and Ti 3p states. The hybridization broadens the valence band and the transfer of photo-generated holes is prompted (López & Gómez, 2012).

The indirect band gap is determined by the Tauc's plot (Inset Figure 4.9 a,b)

$$\alpha h\nu = A\,(h\nu - E_g)^{\gamma}$$

where α is the linear absorption coefficient of the material, hν is the photon energy, A is a proportionality constant and γ is a constant depending on the band gap nature; γ 1/2 for direct band gap and γ 2 for indirect band gap. For an indirect band gap, the Tauc equation can be rearranged as $(\alpha h\nu)^{1/2} = A_2(h\nu - E_g)$. A plot $(\alpha h\nu)^{1/2}$ vs hν would have a linear region with slope A_2 and whose extrapolation to α(hν) = 0 would give the value of the indirect band gap (Mansoor et al., 2015). The calculated band gap of pure TiO_2 is 3.19 eV (4.10a) and for Fe_3O_4 is 1.70 eV (4.9b). It is interesting to note that the coating of CS over Fe_3O_4 cause a slight reduction in band gap, which is observed to be 1.61 eV (Figure 4.9c). This might be due to the existence of CS in the Fe_3O_4 matrix. CS is a semi crystalline material with absorption edge in wider ranges, which leads the absorption edge to slightly higher wave number in the case of Fe_3O_4/CS. Similar finding were reported in literature for TiO_2/CS composite system (Saravanan et al., 2018).

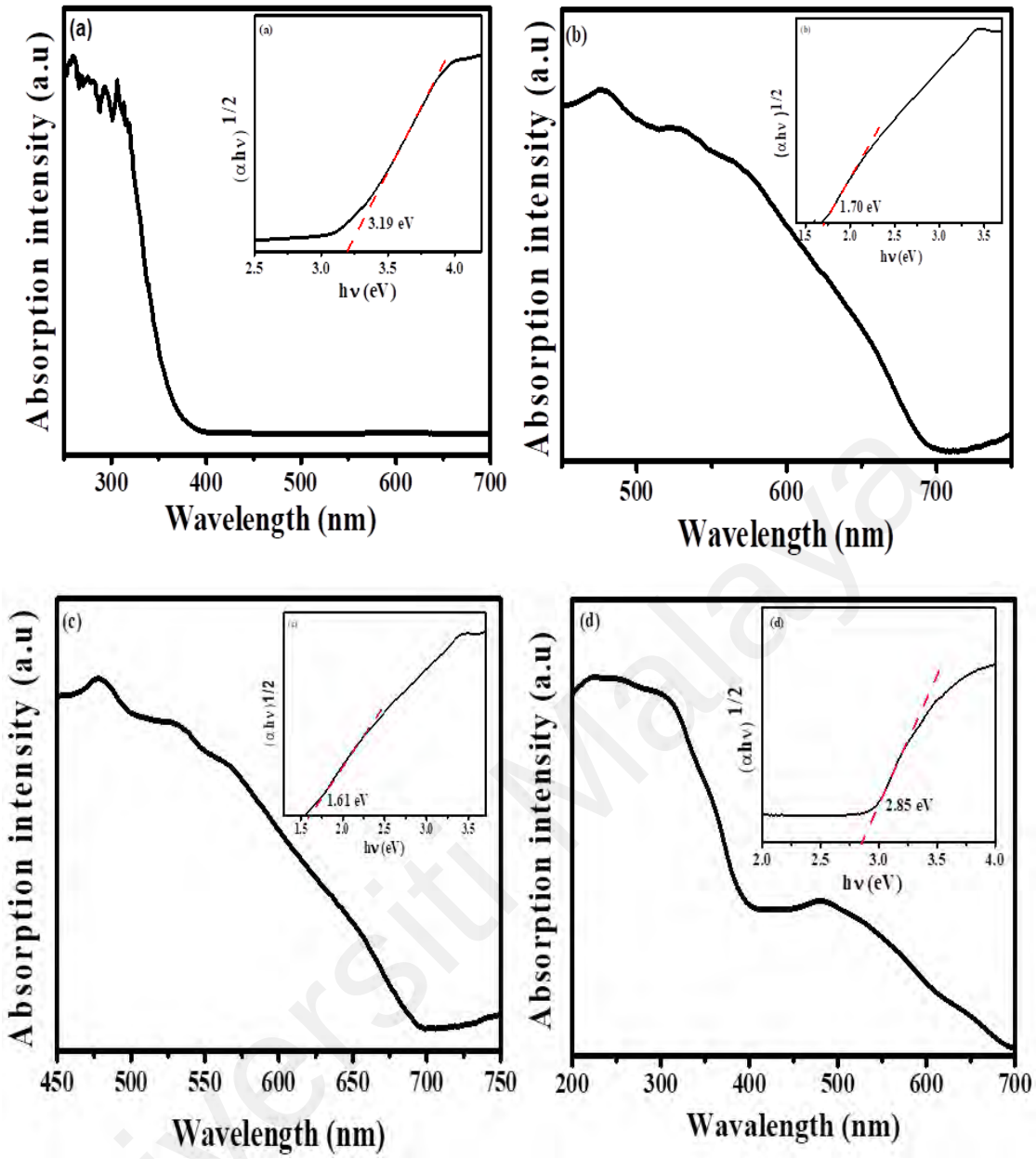

Figure 4.9: Full range absorption spectrum and calculated band gap (inset) of (a) TiO_2 and (b) Fe_3O_4, (c) Fe_3O_4/CS and (d) TCF2 composite

The absorption spectrum of TCF2 displays broad absorption in the entire visible region and the calculated band gap is 2.85 eV (Figure 4.9d). The reduction of band gap in TCF2 is possibly attributed to the presence of Fe_3O_4/CS. The presence of Fe_3O_4 in TCF2 nanocomposite cause the red shift in the absorption spectrum. This is consistent with the fact that Fe_3O_4/CS has a small band gap than pure TiO_2. Therefore, incorporation of Fe_3O_4/CS in TiO_2 shifts the absorption in the visible region of spectrum. The reduction in band gap inhibit charge carrier recombination rate, improved radical formation and consequently facilitate the good photocatalytic activity (Samsudin

et al., 2015c). It is also reported that the band gap of semiconductor is particles size dependent and is increases with decease of particle size (Banisharif et al., 2013). TCF2 have larger particle size than TiO_2 as evident from XRD and TEM results, hence this finding supports the reduction of band gap in TCF2 as particles size is inversely related with the band gap (Koole et al., 2014).

4.1.6 Surface chemical state

The chemical composition, sorption sites and interaction between ions present in TCF2 were further investigated by XPS. Figure 4.10 shows the representative individual XPS spectra of Ti 2p, O 1s, N 1s and Fe 2p3. The survey spectrum indicated the presence of five elements namely Ti, O, N, C and Fe on the catalyst surface (Figure 4.10a). The binding energies of all the elements were aligned with C 1s peak at 285 eV, corresponding to adventitious hydrocarbons from the XPS instrument itself.

The presence of Ti(IV) is indicated in Ti 2p spectrum with binding energies at ~458 eV and ~ 464 eV, conforming to the Ti 2p 3/2 and Ti 2p 1/2 paramagnetic spin respectively (Samsudin et al., 2015c) (Figure 4.11b). Nonappearance of reduce surface Ti(III) is confirmed by the absence of its characteristic peak around 457.7 eV (Samsudin et al., 2015b). Figure 4.10 (c) represents the spectra of O1s which shows the presence of a prominent peak at 529.6 eV, well indexed with the O 1s electron binding energy of TiO_2 and Fe_3O_4 (Liu et al., 2008a). Another peak corresponds to the surface hydroxyl (OH) group observed at 531.06 eV (Samsudin et al., 2016).

As the structure of Fe_3O_4 (magnetite) is inverse spinel which is also possessed by γ-Fe_2O_3 (maghemite), both can have the same XRD patterns. Therefore, XRD by itself is not an ideal method to discriminate between these two iron oxides. However, in XPS the core electron lines demonstrating ferrous and ferric ions can both be detectable and distinguishable (Unsoy et al., 2012). The characteristic doublet photoelectron peak of Fe

2p 3/2 and 2p1/2 core level spectra of iron oxide was observed at 711.7 eV and 725.1 eV respectively and are consistent with the oxidation states of Fe in Fe_3O_4 (Figure 4.9d) (Unsoy et al., 2012; Liu et al., 2010; Teng et al., 2003). Moreover, the absence of satellite peak at 719 eV, which is observed in the case of Fe_2O_3 (Fe(III)), further confirms the purity of the sample as Fe_3O_4 does not show any satellite peak (Djebaili et al., 2015).

The binding energies of N 1s spectra are presented in Figure 4.10 (d) and are observed at 398.40 eV, 399.53 eV and 401.47 eV. These were all attributed to the presence of CS. The binding energy at 398.40 eV corresponds to the C-N bonds (Morant et al., 2009). However, the free amino groups (NH) and amino groups that were involved in hydrogen bond (NH_2–O) were observed at 399.53 eV. Another band for N 1 s at 401.47 eV was assigned to chelation between the amino groups and iron ions (NH2–Fe) (Unsoy et al., 2012; Wang et al., 2009b). In addition, the binding energy at around 401 eV is an indication of molecularly chemisorb nitrogen (Samsudin et al., 2015a; Hu et al., 2014) or metal coordinated NH_2 →Ti (Aqil et al., 2014). Hence, the expected interactions in TiO_2/CS/Fe_3O_4 nanocomposite are between metal oxides (TiO_2, Fe_3O_4) and NH_2 groups of CS (Xiao et al., 2013; Yan et al., 2011; D. Yang et al., 2009).

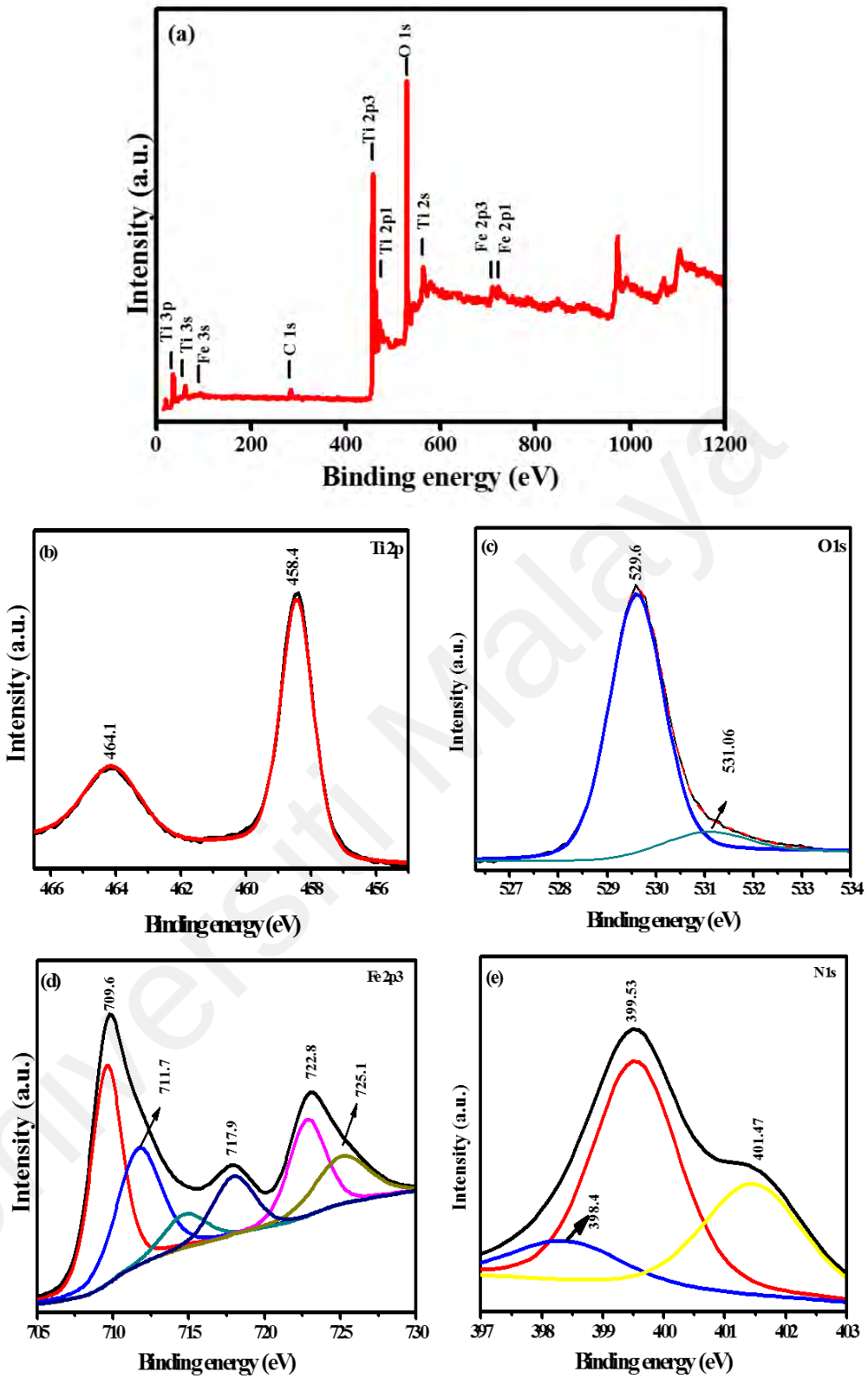

Figure 4.10: XPS spectrum of (a) survey spectra of TiO_2/CS/Fe_3O_4 nanocomposite and narrow scan of TiO_2/CS/Fe_3O_4 (b) Ti 2p, (c) O1s, (d) Fe 2p3, (e) N1s

4.2 Photocatalytic activity on the degradation of ONP

The photocatalytic activity of TCF2 nanocomposite was evaluated by photodegrading ONP under visible light irradiation. The concentration of ONP in test solutions was measured at λ_{max} 278 nm. Primarily, the degradation of ONP was carried out with TCF2 in comparison with pure visible light as blank, bare TiO_2, Fe_3O_4 and Fe_3O_4/CS. This is to confirm that proposed modification of TiO_2 by Fe_3O_4/CS has truly overcomes the draw backs of bare TiO_2 as addressed earlier. The photolysis of ONP by visible light show only 16% removal. However, the removal percentage increased gradually with Fe_3O_4 and Fe_3O_4/CS, which show 70% and 74% degradation of ONP respectively. The removal percentage is significantly enhanced in the presence of TiO_2 and TCF2 nanocomposite Figure 4.11. Though, the most promising photocatalytic activity was achieved with TCF2 nanocomposite, which gives 92% degradation of ONP. Bare TiO_2 shows only 83% within 180 minutes of visible light exposure. Although Fe_3O_4 and Fe_3O_4/CS possess small band gaps than TiO_2 and TCF2, their photocatalytic activity is lower than these two. The lower photocatalytic activity of Fe_3O_4 and Fe_3O_4/CS is reported to be due to high recombination rates of photogenerated charge carriers (Wang et al., 2017b). The slightly higher photoactivity of Fe_3O_4/CS than Fe_3O_4 is due to the presence of CS layer, which enhanced the adsorption of pollutant molecule and consequently overall photoactivity.

The superior photocatalytic activity of TCF2 than bare TiO_2, Fe_3O_4 and Fe_3O_4/CS can be explained by considering the characterization results. The presence of metal coordinated nitrogen which constitutes NH_2 groups of CS in TCF2 increases the surface adsorption of pollutant molecules, and hence enhanced its photocatalytic activity. The presence of metal coordinated CS not only increase the adsorption but also reduce the e^-– h^+ recombination rate as CS act as an electron shuttle between metal oxide and

dioxygen molecule. Similar findings were also obtained in the literature for TiO_2/CS and TiO_2-polyoxometalate system (Ozer & Ferry, 2001). The coupling of two semiconductors (TiO_2 and Fe_3O_4) in TCF2 favors the reduction in e^-– h^+ recombination rate and eventually increases the overall photocatalytic activity of TCF2 composite system.

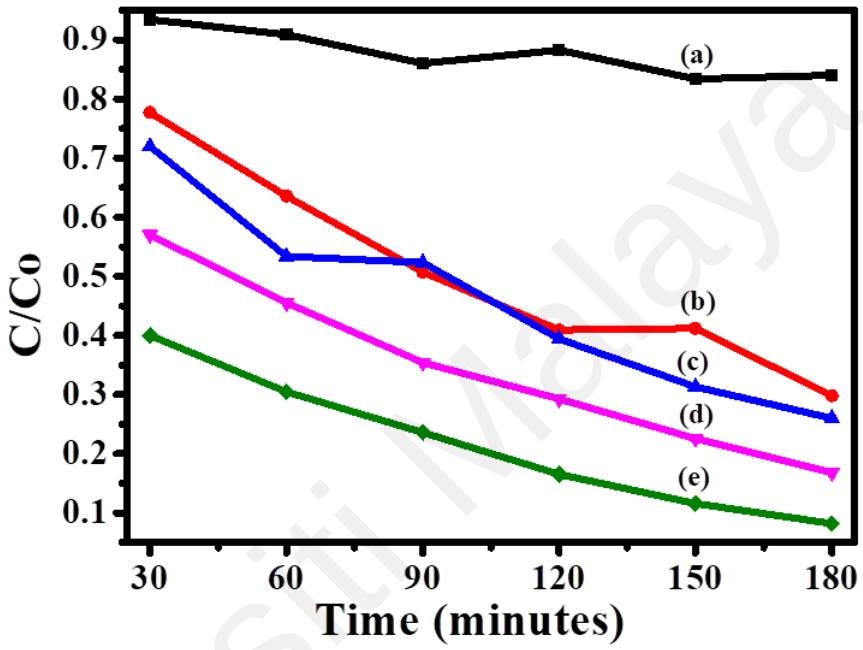

Figure 4.11: Degradation of ONP under (a) pure visible light, (b) Fe_3O_4 (c) Fe_3O_4/CS (d) TiO_2 and (e) TCF2 nanocomposite

4.3 TCF nanocomposite under varying concentrations (TiO_2, CS, Fe_3O_4)

4.3.1 Effect of TiO_2 content

4.3.1.1 Morphology

The morphology of the composites prepared on varying concentration of TiO_2 is to evaluate its effect presented in Figure 4.12. The basic structure of both composites is the same, containing TiO_2 nanoparticles coated over Fe_3O_4/CS core. These TiO_2 nanoparticles distributed over the Fe_3O_4/CS core can be clearly seen in TCF-T1 (Figure 4.12a) and TCF-T3 (Figure. 4.12b). This indicated the complete covering of TiO_2 nanoparticles over Fe_3O_4/CS core.

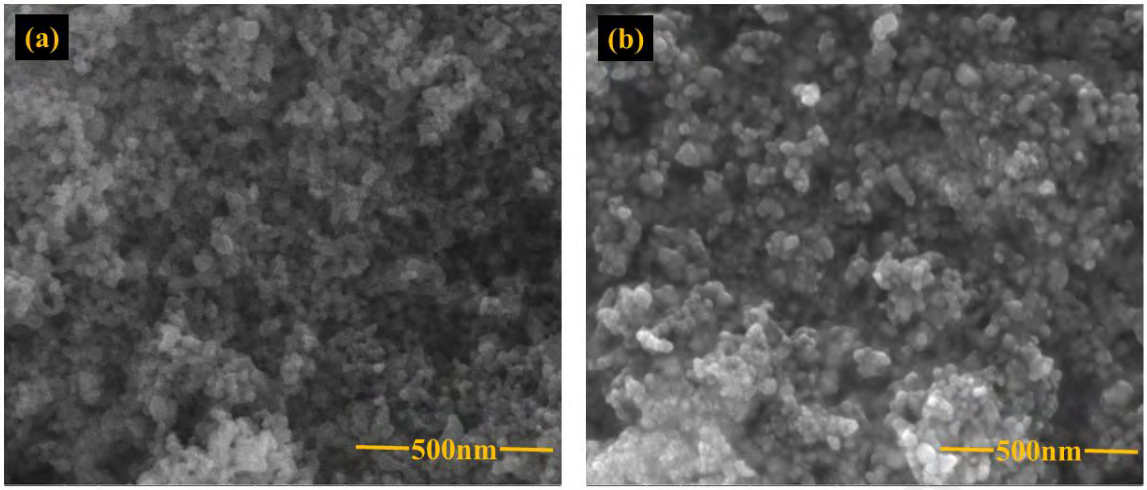

Figure 4.12: FESEM images of TCF nanocomposite on varying concentrations of TiO_2

The elemental composition of the composites prepared by varying TiO_2 concentration was determined. The weight percent of Ti, O, C and Fe are tabulated in Table 4.3. The table shows the presence of Ti, O, C and Fe in all the composite samples, however, the EDX data confirms that the weight (%) of TiO_2 differed in all three composites. This difference in weight (%) is due to the varying concentration of TiO_2. The highest concentration of Ti was observed to be in TCF-T3 which decreases gradually as the Ti amount in the composite sample decrease.

Table 4.3: EDX elemental composition (weight %) of Ti, O, C and Fe in TCF nanocomposites

Composite samples	Ti	O	C	Fe
TCF-T1	56.16	37.99	1.81	4.04
TCF2	60.77	27.56	5.73	5.95
TCF-T3	70.94	22.40	4.34	2.32

The elemental distribution of the nanocomposites prepared at higher and lower TiO_2 concentration than TCF2 were obtain through EDX mappings, which illustrates the obvious distribution of the elements (Ti, O, C, Fe) in all the composite samples (Figure 4.13). It can be noted that Ti, O, C and Fe signals are clearly observed in all the

composite samples. In Figure 4.13 (b), the area of spectrum shows the prominent green color of TiO_2 as concentration of TiO_2 is high in this sample.

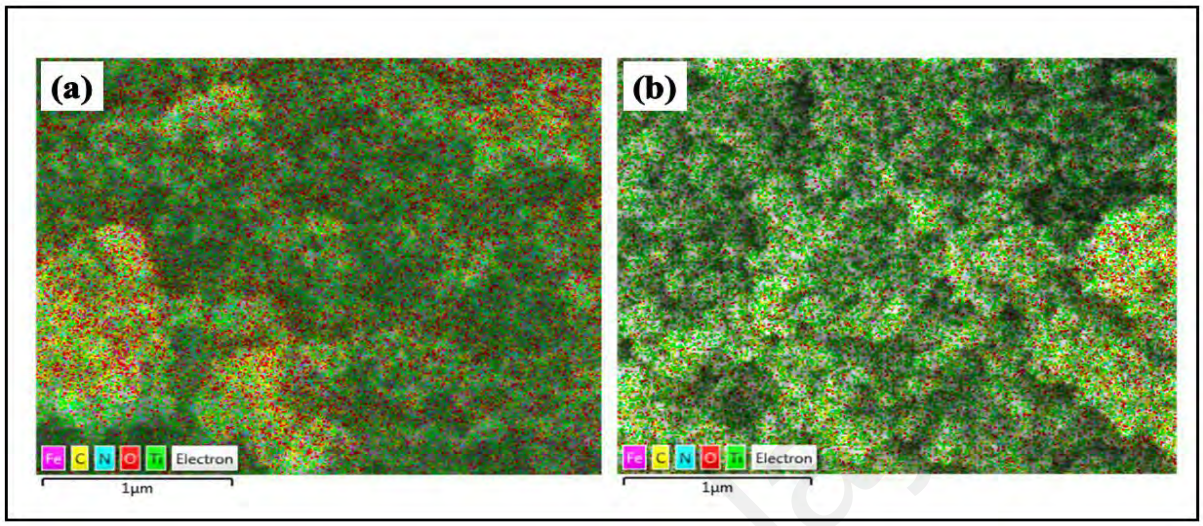

Figure 4.13: Elemental mapping of (a) TCF-T1 and (b) TCF-T3

4.3.1.2 Crystal properties

XRD analysis was conducted to determine the crystallinity, phase mixture and crystallite size of as synthesized nanocomposites on varying TiO_2 concentration. Figure 4.14 shows the X-ray patterns of the composite samples prepared with varying concentration of TiO_2. The diffraction peaks in both composite samples TCF-T1 (Figure 4.14a) and TCF-T3 (4.14b) were observed around 25.4, 27.5, 30.4, 35.7, 37.9, 48.2, 55.2 and 57.2° corresponding to the 101, 110, 220, 311, 211, 002, 112 and 511 planes which indicate the presence of both Fe_3O_4 and TiO_2 in the composite samples. The average crystallite size for both samples was calculated using Scherrer's equation [$D = (K\lambda)/\beta\cos\Theta$)] (Table 4.3). As TiO_2-P25 was used in this study and Fe_3O_4/CS was synthesized by using co-precipitation method using same experimental conditions, changing the concentration of TiO_2 does not have much impact on the crystalline properties of the composite samples. However, the crystallite size was found to be low at lower TiO_2 content (TCF-T1) (Table 4.4). This could be due to the faster nucleation

rates observed at lower Ti content, which led to the formation of smaller crystallites. Similar findings were also reported in the literature (Isley & Penn, 2006).

Table 4.4: Average crystallite size of TCF nanocomposites on varying concentration of TiO_2, CS and Fe_3O_4

Composite samples	Crystallite size (nm)
TCF-T1	19.9
TCF2	24.5
TCF-T3	23.5

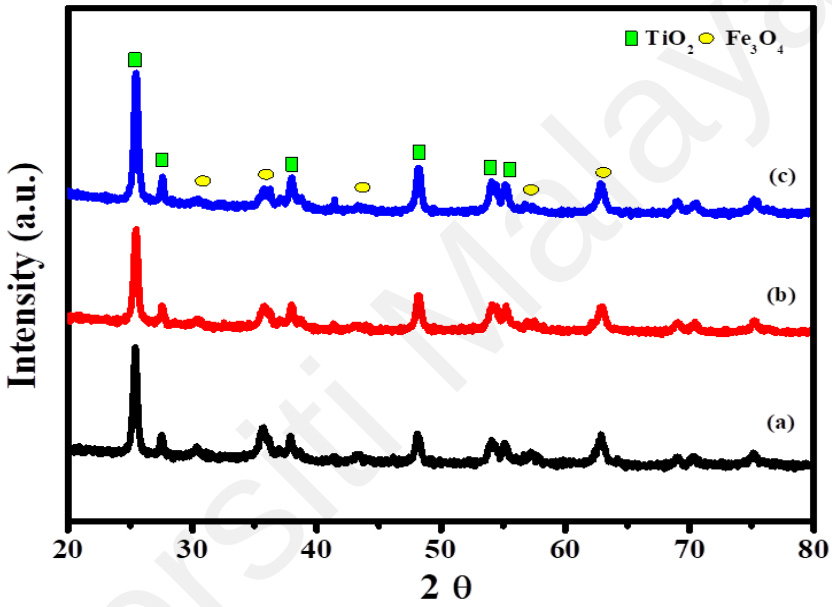

Figure 4.14: XRD spectra of (a) TCF-T1, (b) TCF2 and (c) TCF-T3 nanocomposite

4.3.1.3 Magnetic properties

Magnetism is a distinctive property which overcomes the recovery hurdle of composite after wastewater treatment. The variation in the concentration of TiO_2 is expected to have a significant effect on the magnetic properties of the resultant composite. As TiO_2 is nonmagnetic in nature, the alteration in its concentration also affects the overall magnetic properties of the composite sample. The hysteresis measurement of composite samples in applied field ranging from -10 to 10 kOe at room temperature are presented in Figure 4.15, which indicates a decline in magnetic properties as concentration of TiO_2 was increased, obviously due to their nonmagnetic property. Ms values (Table:

4.5) shows a decline as it moves from TCF-T1 to TCF-T3. As TiO_2 is non-magnetic, by increasing its concentration, the magnetism of the composite sample will reduce. This evidence is also in the favor of successful coating of TiO_2 onto Fe_3O_4/CS composite surface.

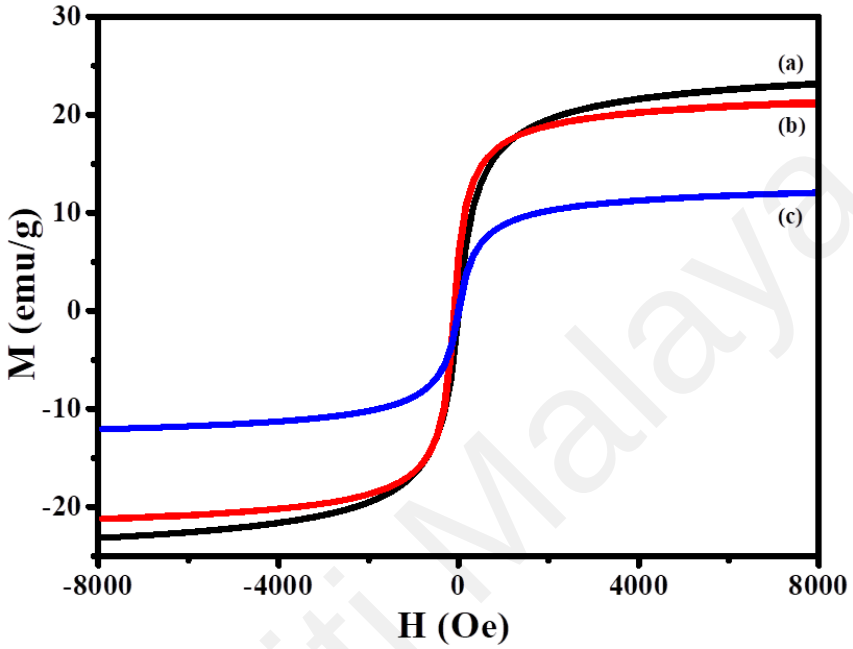

Figure 4.15: VSM spectra showing (a) TCF-T1 (b) TCF2 and (c) TCF-T3 nanocomposite

Table 4.5: Saturation magnetization, coercivity and magnetic remanence of all the synthesized nanocomposites

Composite sample	Saturation magnetization (Ms) emu/g	Coercivity (Hci)	Magnetic remanence (Mr) emu/g
TCF-T1	23.16	6.64	0.42
TCF2	21.46	2.68	0.14
TCF-T3	12.07	9.61	0.32

4.3.1.4 Chemical composition

The chemical composition and interactions between composite components (TiO_2, CS and Fe_3O_4) is determined by FTIR. In Figure 4.16 the FTIR spectra of composite samples prepared on varying TiO_2 concentration are presented and compared. All the samples show almost consistent absorption band with a variation in their intensities. The

peak at 633 cm^{-1} is associated with metal-oxygen (Ti-O and Fe-O) stretching vibrations (Chen et al., 2012). The IR absorption band in range of 1072 cm^{-1} corresponds to C-H bending vibrations. Another absorption band observed ~1391 cm^{-1} corresponds to asymmetrical C-H bending of CH_2 group of CS (Kumirska et al., 2010). The peak at 1629cm^{-1} is assigned to characteristic N-H scissoring from primary ammine due to the presence of free amino groups in CS (Chen et al., 2012; Unsoy et al., 2012). The IR bands at 2851cm^{-1} and 2925 cm^{-1} are due to the stretching vibrations of -CH_2 groups in CS (Du et al., 2014). These peaks are with low intensity in case of TCF2 might be due to the strengthening of interactions between metal oxide and CS. A prominent peak at 3402 cm^{-1} reflects the overlapping of the stretching vibrations of N-H and O-H groups (Du et al., 2014; Chen et al., 2012). In Figure 4.16a, overall high absorption intensities are observed at low TiO_2 content and gradually decrease as TiO_2 concentration was increased. All the composite samples show absorption peaks, indicating the presence of metal oxide and CS functional groups and the involvement of these groups in bonding with metal oxides.

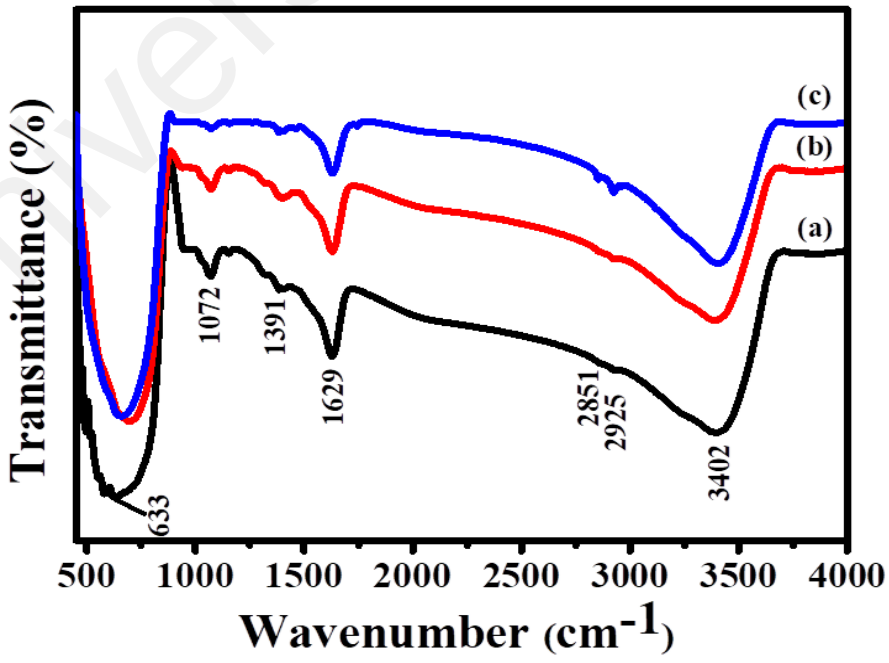

Figure 4.16: FTIR spectra of (a) TCF-T1 (b) TCF2 and (c) TCF-T3 nanocomposites

4.3.1.5 Optical properties

To evaluate the fate of e^-– h^+ recombination in the composite samples, PL emission spectroscopy was carried out. The recombination rate of these photo generated e^-– h^+ is directly related with the intensity of PL spectra (Zha et al., 2015). The PL emission spectra of composite samples prepared with varying TiO_2 concentration are presented in Figure. 4.17. All the samples display distinguished PL peaks at 415 nm, 442 nm, 496 nm, 519 nm and 663 nm, however, the variation in peak intensity is distinguishable. The PL peak at 415 nm corresponds to the self-trapped excitons (Yenchalwar et al., 2014). The PL peak at 442, 496 and 519 nm corresponds to surface defects and oxygen vacancies (Memesa et al., 2011; Samsudin et al., 2016). The PL peak at 663 nm represents red PL which is the migration of trapped electron (0.7eV-1.4eV) under CB to VB holes (Samsudin et al., 2015b). The broad PL peak at 393 nm in TCF2 agrees well with the Eg of anatase phase TiO_2 crystals (Chen et al., 2011).

It is obvious from the PL spectra that the peak intensity of TCF2 is significantly smaller than TCF-Tl and TCF-T3 composites, which reveal the decrease of recombination rate and enhanced photocatalytic activity of this composite. As mentioned earlier in Figure 4.8 that the PL intensity of native TiO_2 is quite high, indicating the role of TiO_2 content in affecting the PL intensity of the composite samples. As evident from the results, the PL intensity from TCF-T1 to TCF2 decreased. However, the increase in the TiO_2 content led to the increase in the PL intensity in TCF-T3. This can be ascribed to the crystallite size of the composite sample as TCF2 have the larger crystallite size than TCF-T1 and TCF-T3. This might be due to the decrease in the content of surface oxygen vacancy and defect with increasing crystallite size. Therefore, a bulk semiconductor material exhibit weak PL signals in the usual conditions (Liqiang et al., 2006). Moreover, when the crystallite size decreases, the effective band gap increases, therefore, the emitted photon has comparatively higher energy giving

photoluminescence (Gupta & Ramrakhiani, 2009). As reported in literature for TiO_2 nanoparticles synthesized by varying calcination temperatures, the PL intensity decreased as calcination temperature increased due to the increased in crystallite size (Liqiang et al., 2006). Similar finding were also reported for CdS nanoparticles in which the PL intensity of CdS nanoparticles increases by decreasing particle size (Gupta & Ramrakhiani, 2009).

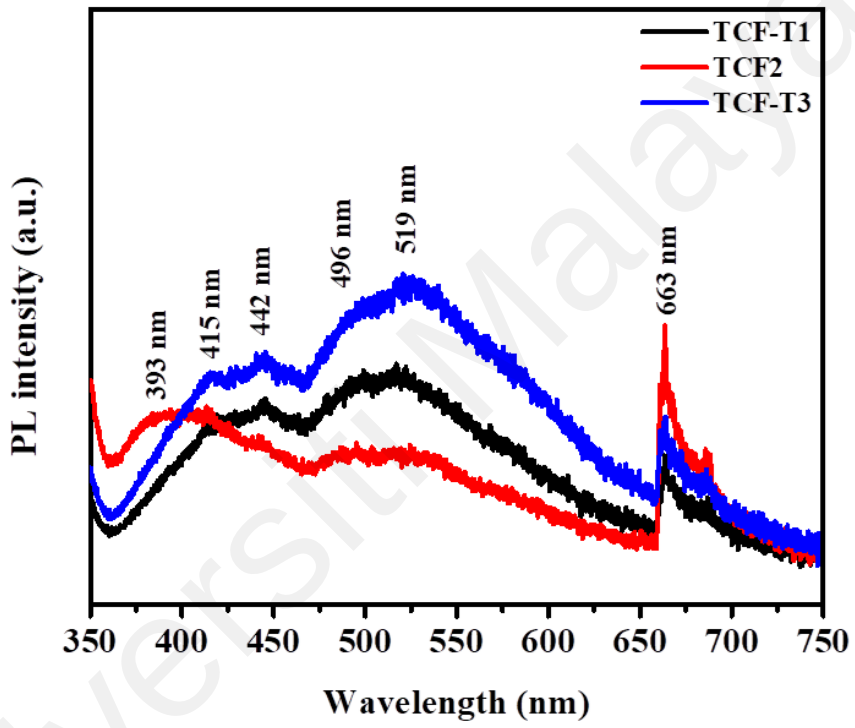

Figure 4.17: PL spectra showing effect of concentration of TiO_2 on optical properties and respective e^+- h^- recombination of nanocomposites

UV-vis diffuse reflectance spectra were used to determine the band gap of the composite samples prepared with the varying TiO_2 concentration. The band gap of the composite samples was determined by Tauc plot and the results are presented in Figure 4.18. It has been observed that the variation in the concentration of TiO_2 altered the band gap. This observation confirms that the concentration of TiO_2 has a strong influence on the optical properties of the composite sample. TCF-T1 (3.05 eV) (Figure 4.18a) and TCF-T3 (3.15 eV) (Figure 4.18b) show a reduced band gap than native TiO_2

(3.19eV). However, this band gap values are higher than TCF2 (2.85 eV) as mentioned earlier. It is interesting to note that increasing and decreasing TiO_2 content in the composite sample than TCF2 will cause increase the band gap. However, both TCF-T1 and TCF-T3 have a slight variation with a difference of 0.1. These results can be correlated to the crystallite size of these samples as TCF2 shows the larger crystallite size than TCF-T1 and TCF-T3.

This phenomenon of band gap broadening by decreasing crystallite size could be explained as that at smaller size the e^-– h^+ pairs are much closer together and the columbic interaction between them can no longer be neglected giving an overall higher kinetic energy. As the size reduced, the number of overlapping orbitals or energy levels decrease, and the width of the band get narrower. This will cause an increase in energy gap between the VB and CB. Similar results were also reported in the literature (Kamarulzaman et al., 2016; Kamarulzaman et al., 2015; Koole et al., 2014).

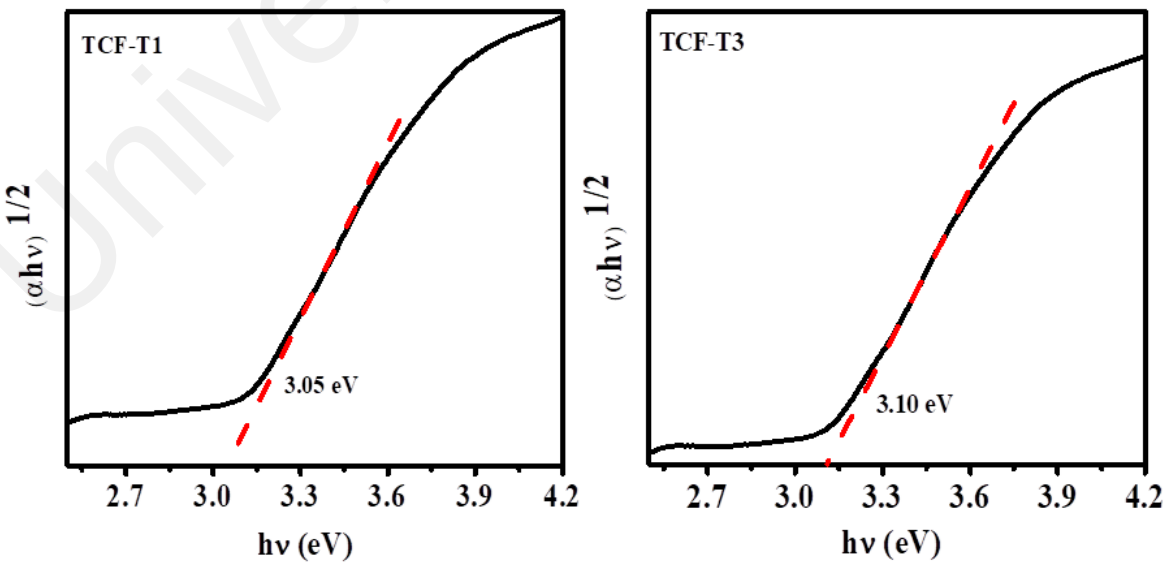

Figure 4.18: UV absorption spectra and calculated band gap of (a) TCF-T1 and (b) TCF-T3

4.3.1.6 Photocatalytic degradation of ONP

The photocatalytic activity of all the three composites samples synthesized on varying concentration of TiO_2 was then compared by degradation of ONP under visible light and the degradation results are presented in Figure 4.19. The change in concentration of TiO_2 as observed in TCF-T1 and TCF-T3 (Table 4.4) decrease the degradation rate and gives 89% degradation of ONP under same conditions. The highest photocatalytic activity was observed for TCF2 with 92% degradation of ONP.

As TiO_2 nanoparticles are coated over Fe_3O_4/CS core to overcome its recovery hurdle and to improve its activity in visible region, a very fine layer of TiO_2 is required to be on the surface of Fe_3O_4/CS. Increasing TiO_2 content as outer layer decrease the adsorption of pollutant molecules by CS and at low concentration, it might be damage during photocatalytic process and expose the internal core (Fe_3O_4/CS). The characterization results revealed the increase in band gap 3.05 eV and 3.15 eV for TCF-T1 and TCF-T3 respectively and high PL intensities for these two composites samples compared to TCF2. Hence the concentration of TiO_2 in TCF2 is considered as the best compared to TCF-T1 and TCF-T3.

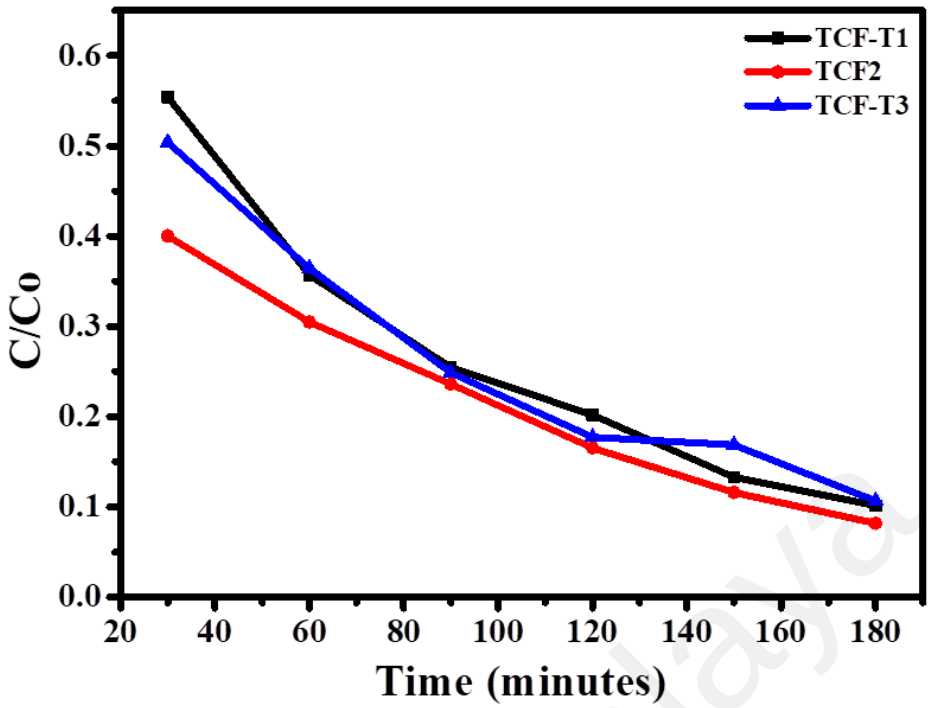

Figure 4.19: Photocatalytic activity of TCF nanocomposites for ONP degradation on different concentration of TiO_2.

The heterogeneous photocatalytic degradation reactions are usually first order and follows Langmuir-Hinshelwood kinetics (Yu et al., 2005). The photocatalytic degradation kinetics of ONP with TCF-T1, TCF2 and TCF-T3 is presented in Figure 4.20. The linearity of the curves represented that the degradation of ONP by TCF nanocomposites follows first order kinetic model i.e., ln (Co/C) = kt, where Co is the initial concentration and C is the concentration at time t. The data of concentration provides nearly a straight line for all the composite samples. The experimental data fitting to first order kinetics are presented and tabulated in Table 4.6. The results clearly show that TCF2 nanocomposite has the highest degradation rate and thus, have a higher photocatalytic degradation activity. This enhanced photocatalytic activity is due to variety of favorable features of TCF2 which enable it to utilize the solar spectrum more efficiently than other composite samples. The rate constant decreases as the concentration of TiO_2 increase or decrease in the composite system than in the TCF2.

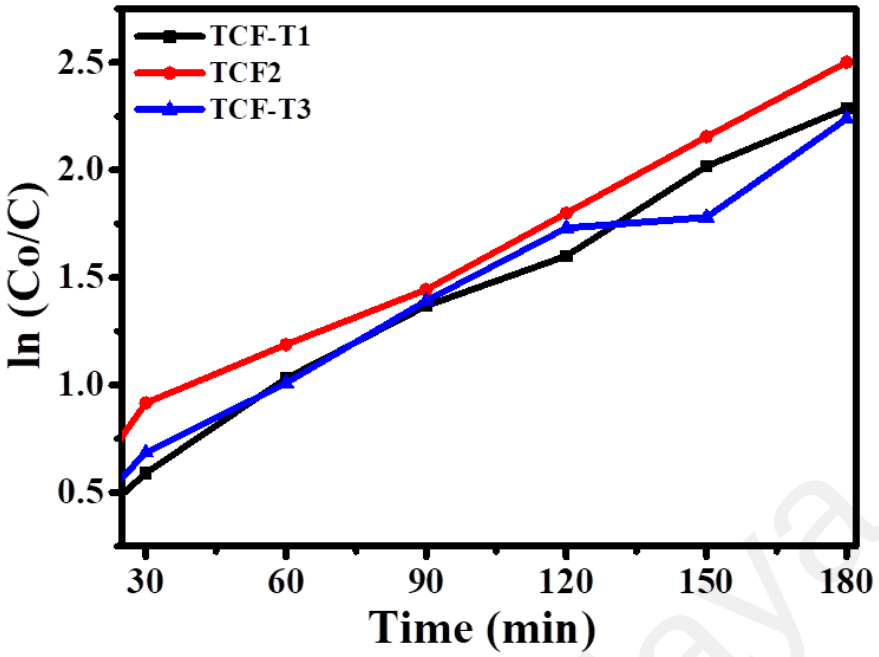

Figure 4.20: First order kinetics for composite samples synthesized on varying TiO_2 concentration on the degradation of ONP.

Table 4.6: Rate constants for the degradation of ONP by composite samples synthesized on varying TiO_2 concentration

Samples	Rate constant (K)	R^2
TCF-T1	0.0127	0.9934
TCF2	0.0138	0.9954
TCF-T3	0.0124	0.9757

From the above results, it was observed that the rate constants for TCF-T1, TCF2 and TCF-T3 are quite close. To confirm the effectiveness of TCF2, all the three composite samples were used for the degradation of ONP at higher concentration (50ppm) and it was observed that the highest degradation rates were still observed for TCF2 followed by TCF-T1 and TCF-T3 (Appendix A & B). This observation confirmed that TCF2 is the optimum composite among these three samples as it shows the highest degradation rates towards ONP even at higher concentration.

4.3.2 Effect of CS loading

4.3.2.1 Morphology

The SEM micrographs of the composite samples prepared by varying CS content are presented in the Figure 4.21 (a) TCF-C1 and (b) TCF-C3. It is obvious from Figure 4.21 that TiO_2 nanoparticles are well distributed throughout the entire composite surface. As CS serves as a linker between TiO_2 and Fe_3O_4, the outer surface of the composites composed of only TiO_2 nanoparticles. Therefore, the variation in CS concentration does not cause much alteration in the morphologies and both samples display the presence of TiO_2 nanoparticle on the surface.

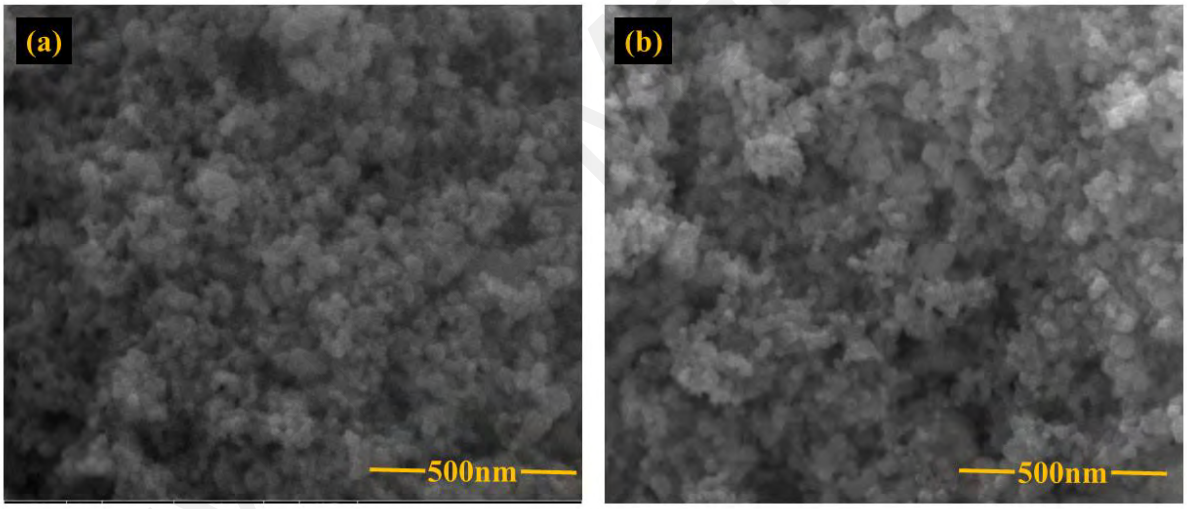

Figure 4.21: FESEM imanges of TCF nanocomposite on varying CS loading (a) TCF-C1 and (b) TCF-C3

The elemental composition and weight percent of Ti, O, C and Fe are tabulated in Table 4.3. The table shows the presence of Ti, O, C and Fe in all the composite samples. Regardless of SEM images, it is evident from Table 4.7 that TCF-C1, TCF2 and TCF-C3 display a distinct difference in weight % of carbon as CS concentration was varied. The highest concentration of C was observed in TCF-C3, which decreases gradually as the CS amount in the composite sample decreases.

Table 4.7: EDX elemental composition (weight %) of Ti, O, C and Fe in TCF nanocomposites

Composite samples	Ti	O	C	Fe
TCF-C1	57.58	38.28	2.28	1.86
TCF2	60.77	27.56	5.73	5.95
TCF-C3	48.27	42.17	8.43	1.13

The distribution of the elements in the composite samples prepared at higher and lower CS concentration than TCF2 were obtained by means of EDX mapping and a noticeable distribution of elements (Ti, O, C, Fe) in TCF-C1 and TCF-C3 can be seen (Figure 4.22). The signals of Ti, O, C and Fe are clearly visible throughout the composite samples. The prominent yellow color of C in TCF-3 can be easily seen in Figure 4.22 (b) as this sample has higher CS content.

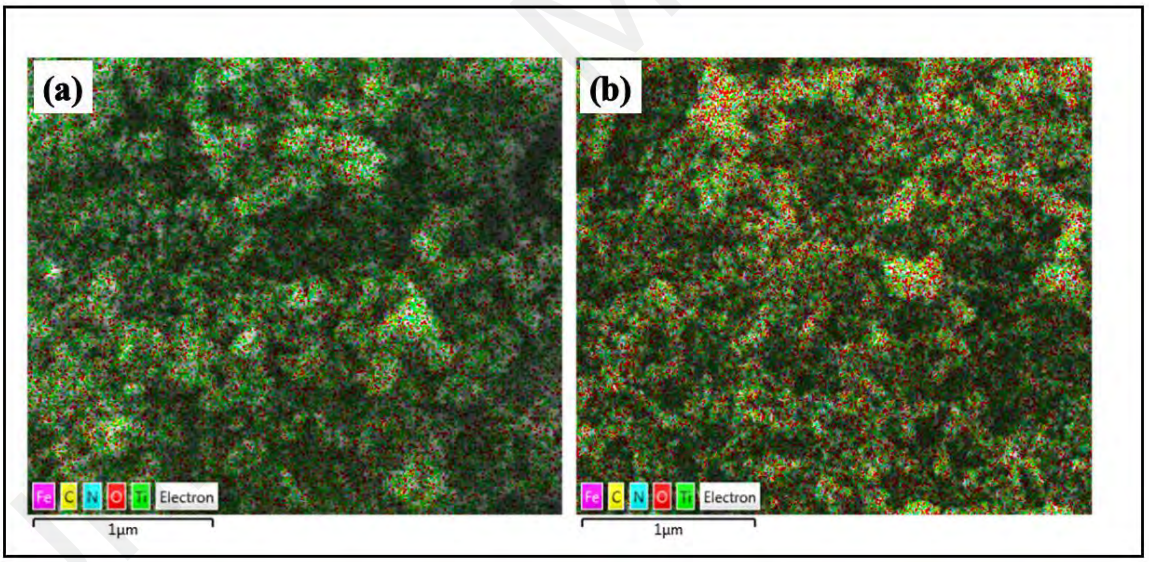

Figure 4.22: Elemental mapping of (a) TCF-C1 and (b) TCF-C3

4.3.2.2 Crystal properties

For the determination of crystallinity and crystallite size of the composite samples prepared on varying CS concentration, XRD analysis was conducted. Figure 4.23 shows the X-ray patterns of all the composite samples (a) TCF-C1, (b) TCF2 and (c) TCF-C3. All the three samples show presence of both Fe_3O_4 and TiO_2 with observed diffraction

peaks around 25.4, 27.5, 30.4, 35.7, 37.9, 48.2, 55.2 and 57.2° corresponds to the 101, 110, 220, 311, 211, 002, 112 and 511 planes. Scherrer's equation [$D = (K\lambda)/\beta\cos\Theta$)] was used to calculate the average crystallite size for each sample (Table 4.8). The crystallinity of all the three composite samples was not much altered as their synthesis was done under identical experimental conditions by varying only CS concentration. However, a decrease in crystallite size of the composite sample prepared at higher concentration of CS (TCF-C3) was observed. Similar observations were also reported in the literature, where increasing CS content drop the crystallite size in TiO_2/CS nanocomposite. By increasing CS loading, the Fe_3O_4 distribution in solution is affected and Fe_3O_4 clusters are separated into small sized Fe_3O_4 which then interact with CS to produce small sized CS coated Fe_3O_4 nanoparticles (Wulandari et al., 2017).

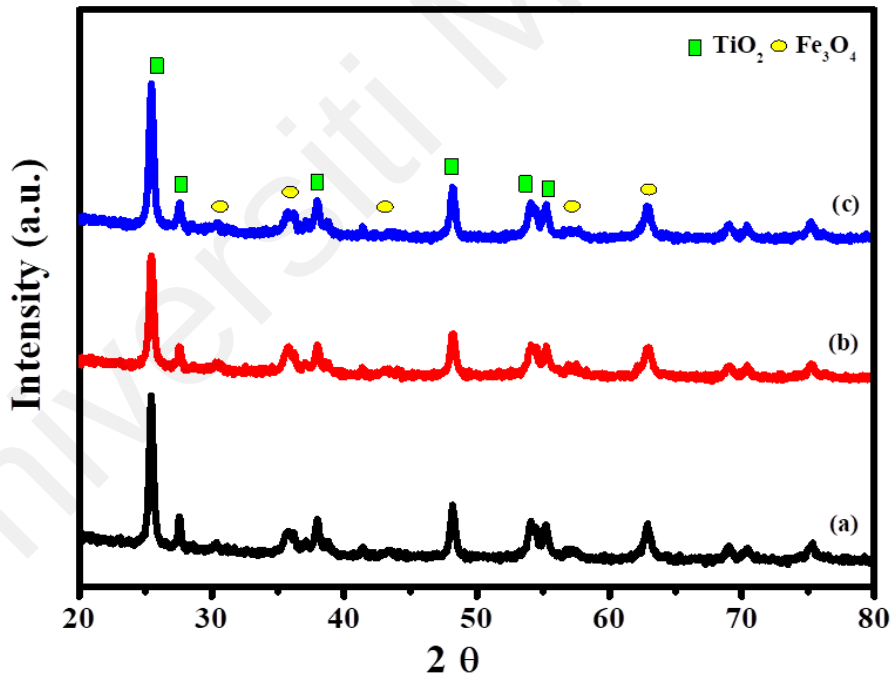

Figure 4.23: XRD spectra of (a) TCF-C1 (b) TCF2 and (c) TCF-C3

Table 4.8: Average crystallite size of TCF nanocomposites on varying concentration of CS

Composite samples	Crystallite size (nm)
TCF-C1	19.2
TCF2	24.5
TCF-C3	17.0

4.3.2.3 Magnetic properties

The magnetic properties of composite samples prepared on varying concentration of CS are presented in Figure (4.24). As CS is also nonmagnetic in nature like TiO_2, the alteration in its concentration also affects the overall magnetic properties of the composite sample. Figure 4.24 (a and b) indicate an inflation and a decline in magnetic properties as the concentration of CS was decreased and increased respectively. Ms values (Table: 4.9) shows a decline, moving from TCF-C1 to TCF-C3. As CS is non-magnetic, increasing its concentration will lead to a reduction in the magnetism of the nanocomposite. This evidence is in favor of successful coating of CS onto Fe_3O_4.

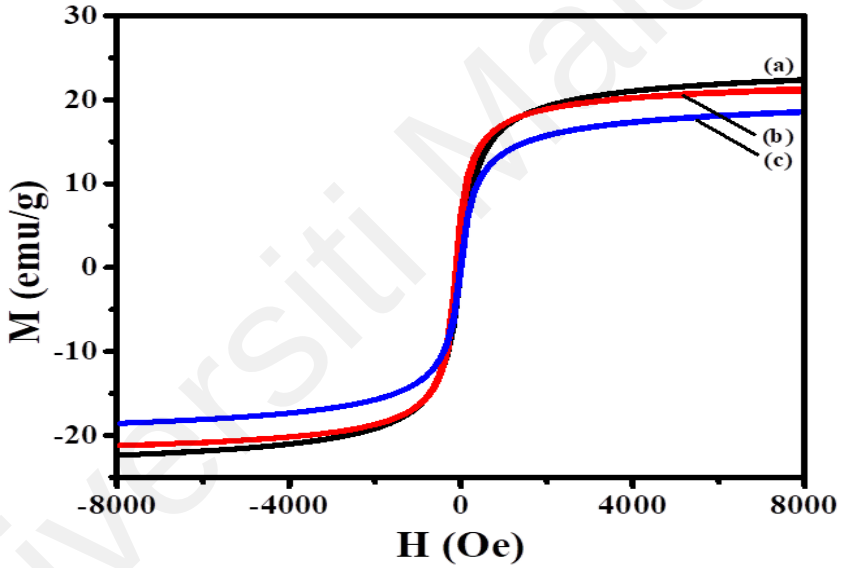

Figure 4.24: VSM spectra of (a) TCF-C1 (b) TCF2 and (c) TCF-C3

Table 4.9: Saturation magnetization, coercivity and magnetic remanence of composite samples synthesized on varying CS concentration

Composite sample	Saturation magnetization (Ms) emu/g	Coercivity (Hci)	Magnetic remanence (Mr) emu/g
TCF-C1	22.37	12.08	0.71
TCF2	21.46	2.68	0.14
TCF-C3	18.57	10.09	0.49

4.3.2.4 Chemical composition

Composite samples prepared under varying CS concentration are further characterized based on their chemical composition. The FTIR spectra TCF-C1 and TCF-C3 in comparison to TCF2 are presented in Figure 4.25. The FTIR spectra indicated the presence of both metal oxide (TiO_2, and Fe_3O_4) and CS in the composite samples with a variation in their absorption intensities. The peak at 656 cm^{-1} (Figure 4.25a) is associated with metal-oxygen (Ti-O and Fe-O) stretching vibrations (Chen et al., 2012). The absorption band in the range of 1076 cm^{-1} and ~1393 cm^{-1} is due to asymmetrical C-H bending of CH_2 group of CS (Kumirska et al., 2010). The peak at 1631cm^{-1} is assigned to characteristic N-H scissoring from primary ammine due to the presence of free amino groups in CS (Chen et al., 2012; Unsoy et al., 2012). The characteristic IR bands of CS due to stretching vibrations of -CH_2 groups in CS was obtain at 2848 cm^{-1} and 2922 cm^{-1} (Du et al., 2014). A prominent peak at 3416 cm^{-1} reflects the overlapping of the stretching vibrations of N-H and O-H groups (Du et al., 2014; Chen et al., 2012). The peak intensity associated with metal oxide stretching vibrations (656 cm^{-1}) and stretching vibrations of OH groups (3416 cm^{-1}) are least at higher CS content, obviously because the CS functional groups dominate over metal oxides.

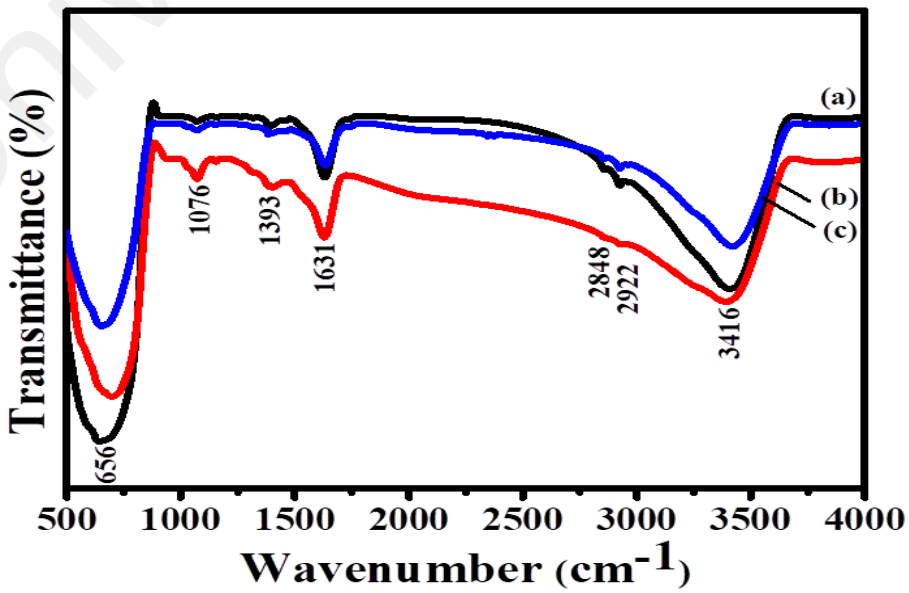

Figure 4.25: FTIR spectra showing effect of (a) TCF-C1, (b) TCF2 and (c) TCF-C3

4.3.2.5 Optical properties

To evaluate the charge carrier separation competency in the composite samples prepared on varying CS loading, the PL spectra are presented in Figure 4.26. The PL emission spectra of TCF-C1 and TCF-C3 in comparison to TCF2 show notable PL peaks around 415, 442, 496, 519 and 663 nm, however, the variation in peak intensity is distinguishable. The PL peak at 415 nm corresponds to the self-trapped excitons (Yenchalwar et al., 2014). The PL peaks at 442, 496 and 519 nm corresponds to surface defects and oxygen vacancies (Memesa et al., 2011; Samsudin et al., 2016). The red PL at 663 nm represents the migration of trapped electron (0.7eV-1.4eV) under CB to VB holes (Samsudin et al., 2015b).

It is obvious from the PL spectra that the peak intensity of TCF2 is significantly smaller than TCF-C1 and TCF-C3 which reveals the decrease of recombination rate and enhanced photocatalytic activity of this composite. The insertion of CS to the composite system facilitate th e^{-}– h^{+} separation as observed in TCF-C1 and TCF2. However, further enhancing CS concentration in the case of TCF-C3 led to the increase in PL intensity, which is still lower than TCF-C1. This indicates that the presence of CS ficilitate the charge carrier separation as mentioned in section 4.3.1.6 and also reported in previous literature. However, the optimum concentration of CS attained in TCF2 as it shows the lowest PL intensity among the composites. This might be due to the difference in the crystallite size of the composite samples. As smaller the size of nanoparticles, the larger the defect contents and oxygen vacancies. TCF2 have the largest crystallite size which might be decrease the content of surface oxygen vacancy and defect, thereby reducing the PL intensity. As also reported in literature, bulk semiconductor material exhibits weak PL signals in the usual conditions (Liqiang et al., 2006).

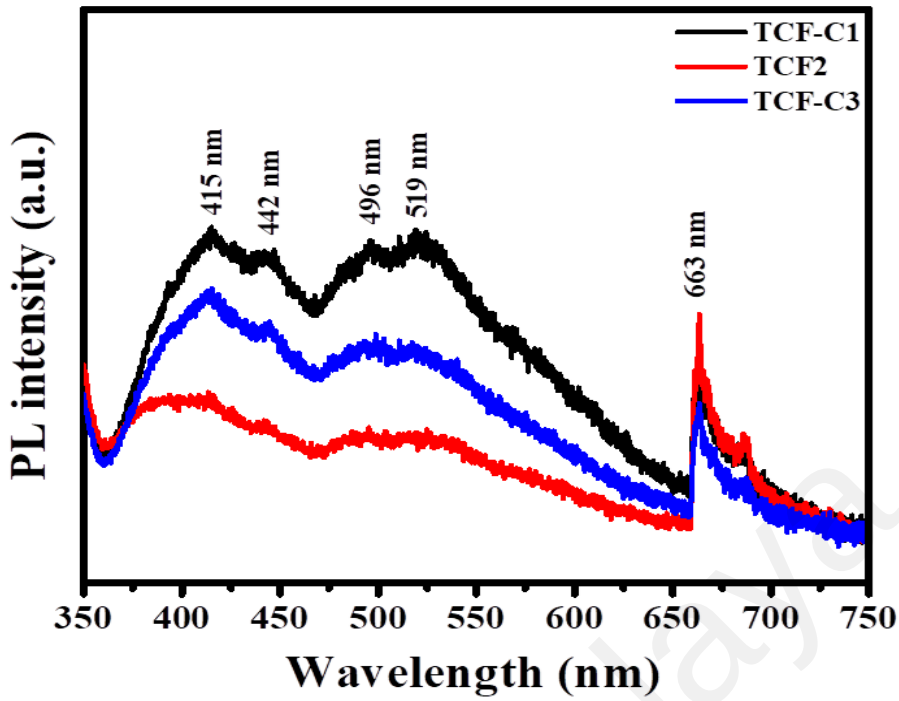

Figure 4.26: PL spectra showing effect of concentration of CS on optical properties and respective e^{+}-h^{-} recombination of resultant nanocomposites

The optical properties and band gap of TCF synthesized on varying CS concentration are further assessed by UV-DR and the band gap is determined by Tauc plot as presented in Figure 4.27. It is obvious from results that the low and high CS content in TCF-C1 (3.15 eV) and TCF-C3 (3.14 eV) respectively, show a slight decrease in band gap than pure TiO_2. However, these values are higher than TCF2 (2.85). These results are well indexed with values of crystallite sizes, as the crystallite sizes of TCF-C1 (19.2 nm) and TCF-C3 C3 (17 nm) are lower than TCF2 (24.5 nm) as detailed in XDR results. This explains their higher band gaps than TCF2. The increase in band gap by decreasing crystallite size is due to electron confinement, as the size reduced the number of overlapping orbitals or energy levels decreases cause to narrow the width of the band. It results in increase in energy gap between the VB and CB (Kamarulzaman et al., 2016; Kamarulzaman et al., 2015; Koole et al., 2014).

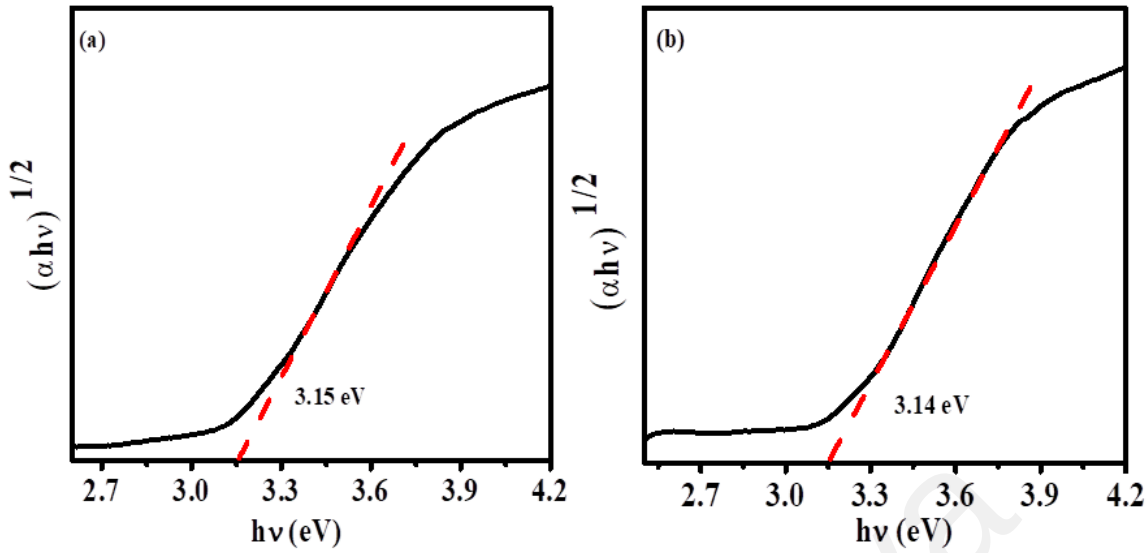

Figure 4.27: UV absorption spectra and calculated band gap of (a) TCF-C1 and (b) TCF-C3

4.3.2.6 Photocatalytic degradation of ONP

The photocatalytic activity of TCF-C1 and TCF-C3 was compared with TCF2 by degradation of ONP under visible light and the results are presented in Figure 4.28. It can be seen from results that at lower CS content (TCF-C1), the degradation efficiency was only 77%. Similarly, for TCF-C3, the degradation efficiency was 80%, which is slightly higher than TCF-C1 but lower than TCF2.

Although CS is used as barrier between TiO_2 and Fe_3O_4, it has an excellent adsorption capacity towards pollutants. Therefore, by lowering the concentration of CS (than in TCF2) the adsorption capacity of the composite also decreased. Likewise, the higher concentration of CS like in TCF-C3 may increase the adsorption capacity but will also increase the viscosity and cause agglomeration, thus reducing the overall photoactivity (Satheesh et al., 2014). Therefore, the optimum concentration of CS as a barrier was achieved in TCF2 which show the higher degradation results (92%). The high photoactivity of TCF2 could be attributed to its optical properties. TCF2 has the highest crystallite size than TCF-C1 and TCF-C3, which led to a comparatively smaller band

gap and lower PL intensity corresponding to lower recombination rates of charge carriers.

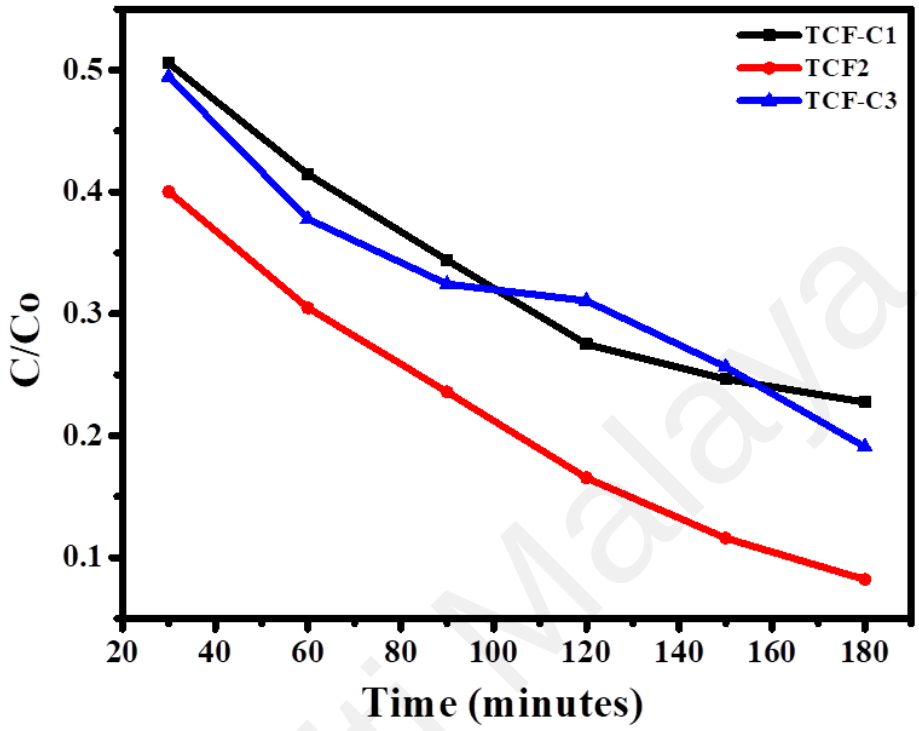

Figure 4.28: Photocatalytic activity of composite samples synthesized on varying CS concentration for ONP degradation

The photocatalytic degradation kinetics of ONP with TCF-C1 and TCF-C3 in comparison to TCF2 is presented in Figure 4.29, which indicate that the degradation of ONP by these composite samples follows a first order kinetic model i.e., ln (Co/C) = kt, where Co is the initial concentration and C is the concentration at time t. Nearly a straight was observed for all the composite samples from the concentration data. The results of the experimental data fitting to first order kinetics are tabulated in Table 4.10, which clearly indicated that TCF2 composite sample has the highest photocatalytic degradation activity and possess higher degradation rate. The enhanced photocatalytic activity of TCF2 than TCF-C1 and TCF-C3 can be attributed to its optical properties. Having the lowest PL intensity coupled with reduce band gap enhance the

photocatalytic degradation performance of TCF2 compared to TCF-C1 and TCF-C3. The rate constant decreases as the concentration of CS increase or decrease in the composite system than in the TCF2. Thus, the optimum concentration of CS was achieved in TCF2.

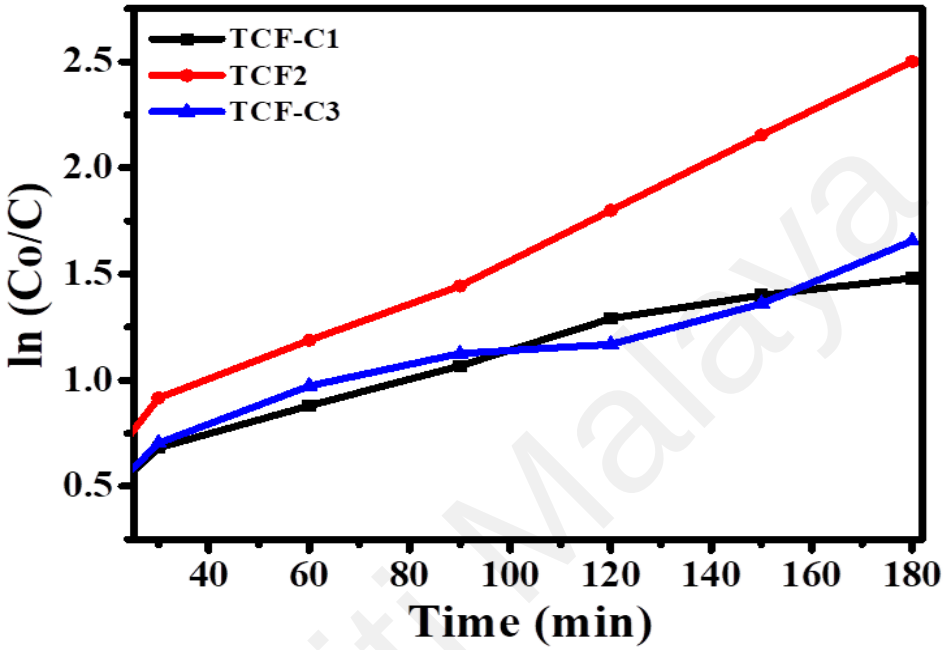

Figure 4.29: First order kinetics for composite samples synthesized on varying CS concentration on the degradation of ONP

Table 4.10: Rate constants for the degradation of ONP by composite samples synthesized on varying CS concentration

Samples	Rate constant (K)	R^2
TCF-C1	0.0082	0.9754
TCF2	0.0139	0.9954
TCF-C3	0.0092	0.9588

4.3.3 Effect of Fe_3O_4 concentration

4.3.3.1 Morphology

To evaluate the effect of Fe_3O_4 concentration on the morphology of the nanocomposite, SEM micrographs were taken and displayed in Figure 4.30. The surfaces of both composite samples TCF-F1 (Figure 4.30a) and TCF-F3 (Figure 4.30b) were covered by well distributed uniform size of TiO_2 nanoparticles. As Fe_3O_4 nanoparticles are the core

material and coated with successive layers of CS and TiO_2, the changes in their concentration did not show any distinctive alteration on the overall morphology of composite samples.

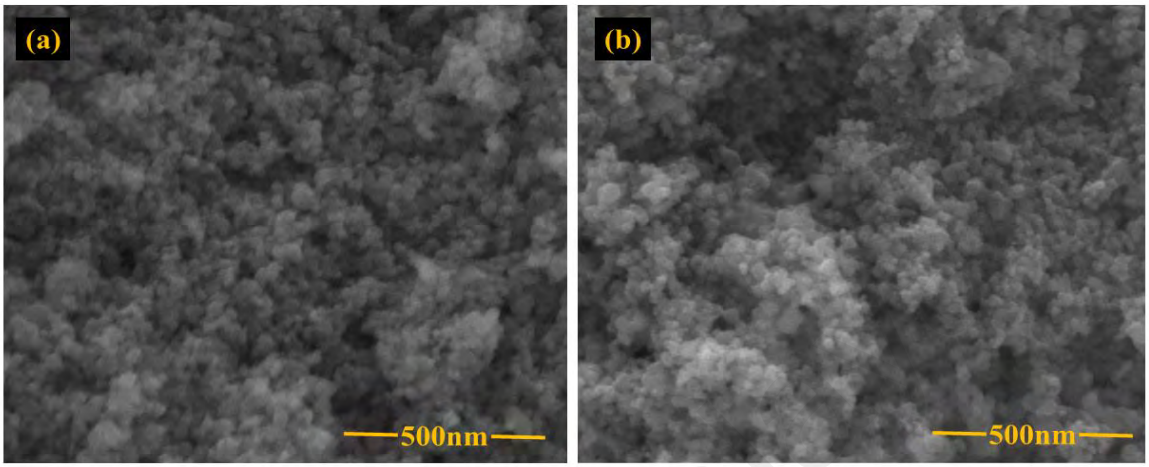

Figure 4.30: FESEM images of TCF nanocomposite on varying Fe_3O_4 concentration (a) TCF-F1 and (b) TCF-F3

The elemental composition of the composites samples prepared by varying Fe_3O_4 concentration was determined and the results are tabulated in Table 4.11. The EDX data confirms the presence of Ti, O, C and Fe in all the composite samples with a variation in weight (%) of these elements due to variation in Fe_3O_4 concentration.

Table 4.11: EDX elemental composition (weight %) of Ti, O, C and Fe in composite sample synthesized on varying Fe_3O_4 concentration

Composite samples	Ti	O	C	Fe
TCF-F1	51.91	43.94	3.45	0.70
TCF2	60.77	27.56	5.73	5.95
TCF-F3	51.42	36.57	3.24	8.77

The elemental distributions of TCF-F1 and TCF-F3 were obtained from EDX mapping which illustrate the obvious distribution of Ti, O, C, Fe in these composite samples (Figure 4.31). It can be noted that Ti, O, C and Fe signals are clearly observed throughout the composite samples. However, in the case of TCF-F3 (Figure 4.31b), the

spectrum was filled with the pinkish color of Fe, indicating the higher concentration of Fe_3O_4 in this composite sample.

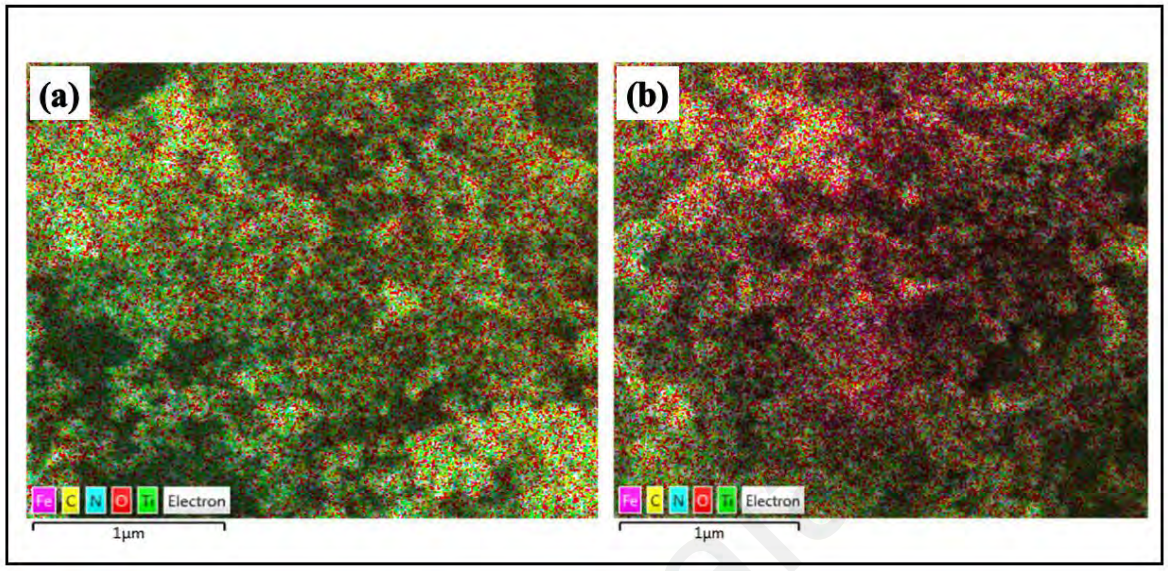

Figure 4.31: Elemental mapping of (a) TCF-F1 and (b) TCF-F3

4.3.3.2 Crystal properties

The crystallinity and crystallite size of composite samples TCF-F1 and TCF-F3 in comparison to TCF2 were obtained by X-ray analysis and the results are presented in Figure 4.32. The results indicate the presence of diffraction peaks in the range of 25.4, 27.5, 30.4, 35.7, 37.9, 48.2, 55.2 and 57.2° corresponding to the 101, 110, 220, 311, 211, 002, 112 and 511 planes. This indicates the presence of both Fe_3O_4 and TiO_2 in all composite samples. The average crystallite size was calculated using Scherrer's equation [$D = (K\lambda)/\beta\cos\Theta$)] (Table 4.12). It is obvious from the results that the difference in Fe_3O_4 content does not have much impact on overall crystallinity of composite samples. However, the trends in the variation in crystallite size were similar as observed by varying CS concentration. By lowering Fe_3O_4 content, the composite sample slightly decreases in crystallite size (TCF-F1 (20.3 nm), TCF2 (24.5 nm)), however, increasing Fe_3O_4 will remarkably reduce the crystallite size (TCF-F3 (18.7 nm)). This indicate that higher concentration of Fe_3O_4 precursors during synthesis of

composite samples promotes faster nucleation resulting in reduction of crystallite size (Kharisov et al, 2015).

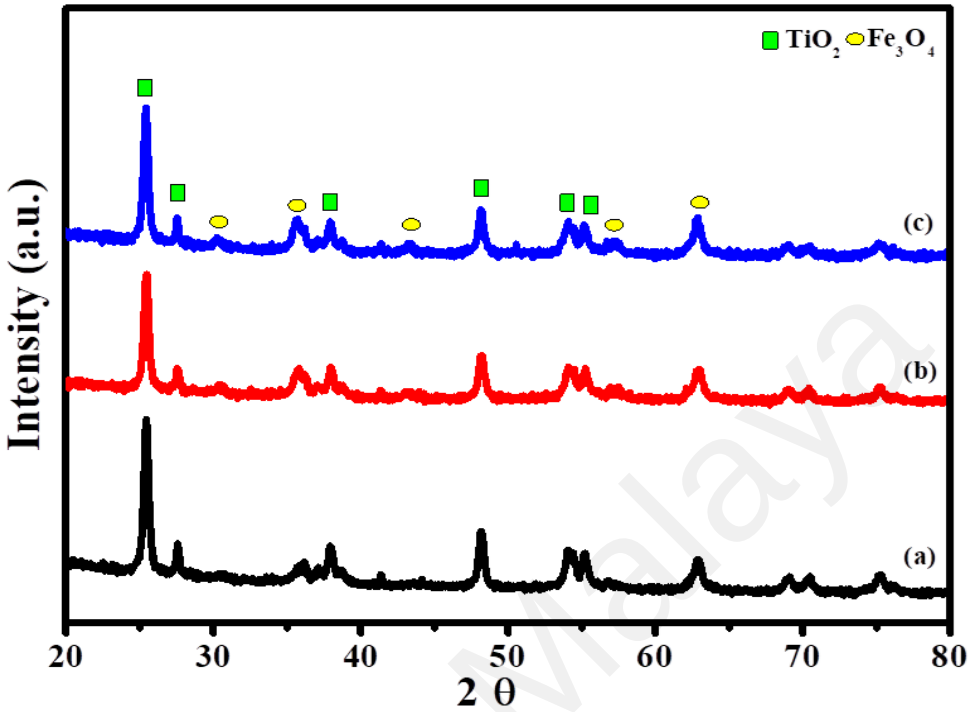

Figure 4.32: XRD spectra of (a) TCF-F1 (b) TCF2 and (c) TCF-F3

Table 4.12: Average crystallite size of TCF nanocomposites on varying concentration of Fe_3O_4

Composite samples	Crystallite size (nm)
TCF-F1	20.3
TCF2	24.5
TCF-F3	18.7

4.3.3.3 Magnetic properties

The use of Fe_3O_4 nanoparticles in this study is to induce magnetism into the resultant composite to enhance its recovery after wastewater treatment. As Fe_3O_4 is the main source of magnetism in the composite samples, so changes in its concentration have remarkable effect on the magnetic properties. The hysteresis measurement is presented in Figure 4.33, which shows a gradual increase in magnetic properties as concentration of Fe_3O_4 increase in the composite samples. The Ms values (Table: 4.13) also shows gradual inflation moving from TCF-F1 to TCF-F3. The composite sample with higher

values of Ms (TCF-F3) is good in terms of its magnetic properties and can be recovered easily after wastewater treatment. However, there are several factors including photoluminescence behavior, band gap and bonding between constituent atoms which determine the overall photocatalytic activity of a sample.

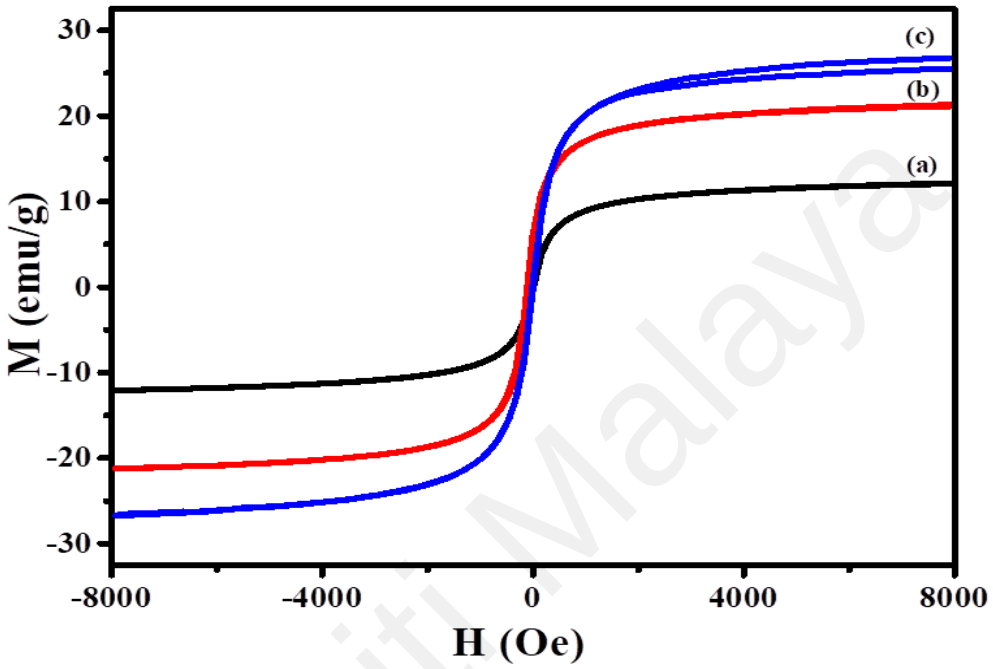

Figure 4.33: VSM spectra of (a) TCF-F1 (b) TCF2 and (c) TCF-F3

Table 4.13: Saturation magnetization, coercivity and magnetic remanence of composite samples synthesized on varying Fe_3O_4 concentration

Composite samples	Saturation magnetization (Ms) emu/g	Coercivity (Hci)	Magnetic remanence (Mr) emu/g
TCF-F1	12.09	10.29	0.38
TCF2	21.46	2.68	0.14
TCF-F3	26.71	5.78	0.59

4.3.3.4 Chemical composition

FTIR spectra have been taken to assess possible chemical composition and interactions between the components of composite samples prepared by varying concentration of Fe_3O_4. It is obvious from the Figure 4.34 that varying metal oxide (Fe_3O_4) concentration does not cause any significant change in the FTIR spectra of composite samples. All the

three samples TCF-F1 (Figure 4.34a), TCF2 (Figure 4.34b) and TCF-F3 (Figure 4.34c) display consistent absorption band indicating the presence of metal oxide (TiO_2 and Fe_3O_4) and CS with a slight variation in their absorption intensities. The peak at 695 cm^{-1} is associated with metal-oxygen (Ti-O and Fe-O) stretching vibrations (Chen et al., 2012). The IR absorption band in range of 1072 cm^{-1} corresponds to C-H bending vibrations. Another absorption band observed ~1397 cm-^{1} corresponds to asymmetrical C-H bending of CH_2 group of CS (Kumirska et al., 2010). The peaks in the range of 1629 cm^{-1} is assigned to the characteristic N-H scissoring from primary ammine due to the presence of free amino groups in CS (Chen et al., 2012; Unsoy et al., 2012). The IR stretching vibrations of -CH_2 groups were observed at 2851cm^{-1} and 2925 cm^{-1} (Du et al., 2014). The prominent peak at 3408 cm^{-1} is due to the overlapping of the stretching vibrations of N-H and O-H groups (Du et al., 2014; Chen et al., 2012). There is no significant difference in the absorption intensities of all the three composite samples. They absorption peaks indicate the presence of metal oxide and CS, and the involvement of CS functional groups with metal oxides.

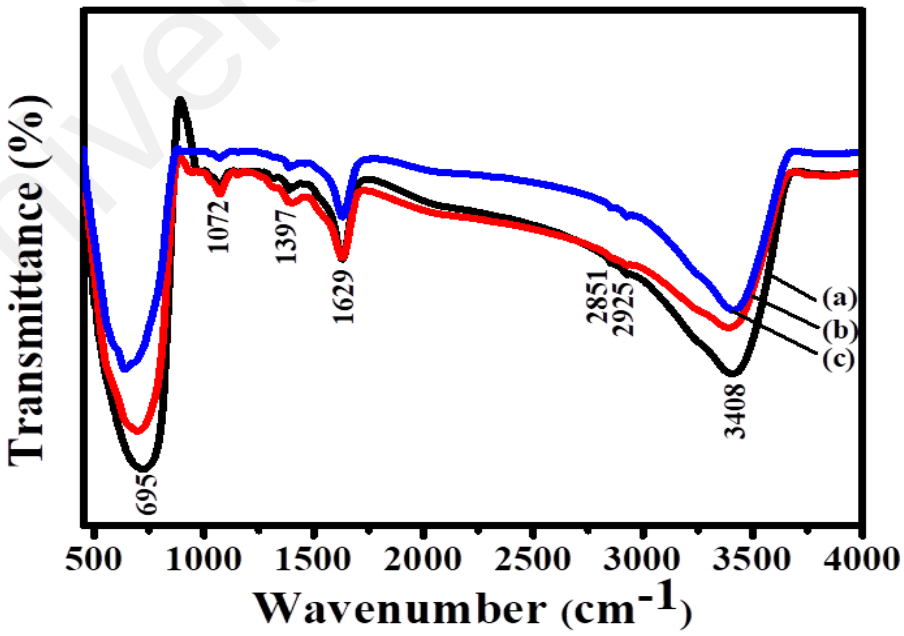

Figure 4.34: FTIR spectra of (a) TCF-F1 (b) TCF2 and (c) TCF-F3

4.3.3.5 Optical properties

PL emission spectroscopy was used to evaluate the fate of e^-– h^+ recombination in the composite samples prepared at varying Fe_3O_4 concentration and the results are presented in Figure 4.35. All the three samples, TCF-F1, TCF2 and TCF-F3, display prominent PL peaks with variation in their intensities. The PL peak at 415 nm indicates the self-trapped excitons (Yenchalwar et al., 2014). The PL peaks at 442, 496 and 519 nm are due to surface defects and oxygen vacancies (Memesa et al., 2011; Samsudin et al., 2016). Another prominent peak was observed at 663 nm, where a red PL is due to the migration of trapped electron (0.7eV-1.4eV) under CB to VB holes (Samsudin et al., 2015b).

As PL intensity is directly associated with the e^-– h^+ recombination, sample with high PL intensity possesses high rate of e^-– h^+ recombination (Zha et al., 2015). It is obvious from the PL spectra that the peak intensity of TCF-F1 and TCF-F3 are almost similar as the two samples have nearly same crystallite sizes. However, their PL intensity is significantly higher than TCF2. The lower PL intensity of TCF2 is due to its larger crystallite size as evidenced from the literature that increasing crystallite size cause a decrease in the PL intensity (Liqiang et al., 2006). It reveals that the recombination rate is considered minimum in TCF2 in comparison to all three composite samples. Hence, the concentration of Fe_3O_4 in TCF2 is considered as optimum and it is expected to show enhanced photocatalytic activity then TCF-F1 and TCF-F3.

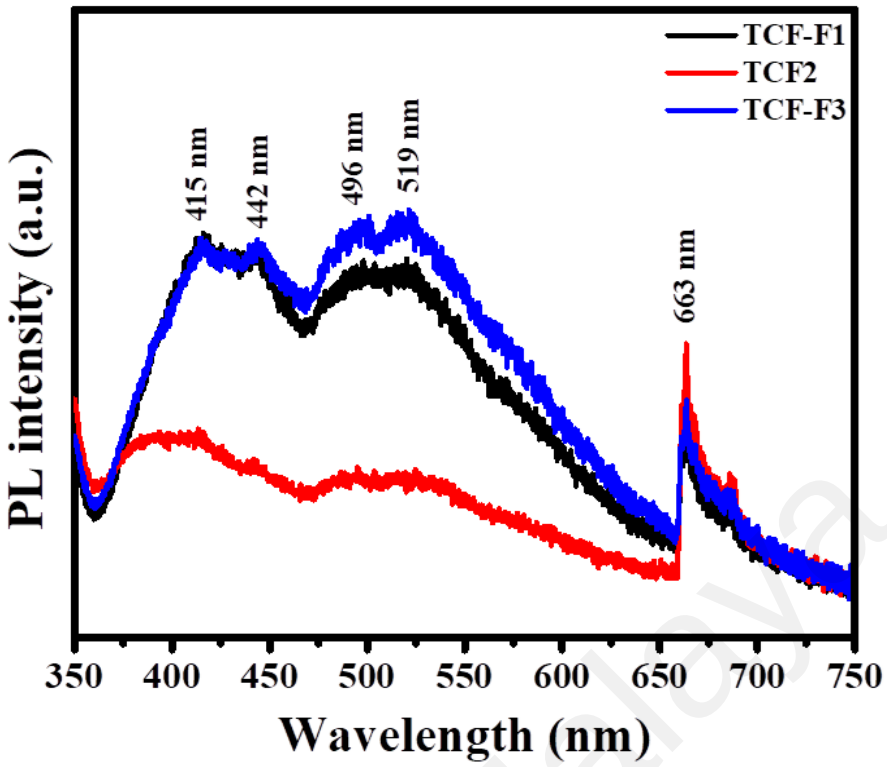

Figure 4.35: PL spectra showing effect of concentration of Fe_3O_4 on optical properties and respective e^+-h^- recombination of resultant nanocomposites

The band gap of the composite samples prepared by varying Fe_3O_4 content was determined by UV-vis diffuse reflectance spectroscopy. Both samples TCF-F1 and TCF-F3 display absorption in the entire UV-vis region (Fig 4.36). Tauc plot was used to calculate the band gap of the composite samples. It was observed that the variation in Fe_3O_4 content in the composite sample has impact on optical properties of the resultant composite and on their respective band gaps. This indicated that a high concentration of Fe_3O_4 is not favorable as it increased the band gap to larger extent. As mentioned earlier that smaller the crystallite size, the broader will be the band gap. TCF-F3 shows a smaller crystallite size in comparison to TCF-F1 and TCF-F2, hence it shows the broadening in band gap. By decreasing crystallite size, the electrons are confined and occupied less space hence VB and CB potentials shifted to more positive and negative edge respectively. It enhances the energy gap between the VB and CB (Kamarulzaman et al., 2016; Kamarulzaman et al., 2015; Koole et al., 2014). Thus, the

minimum concentration of Fe_3O_4 required in TCF composite system to shift its absorption in visible region of spectrum with enhanced photocatalytic performance was achieved in TCF2.

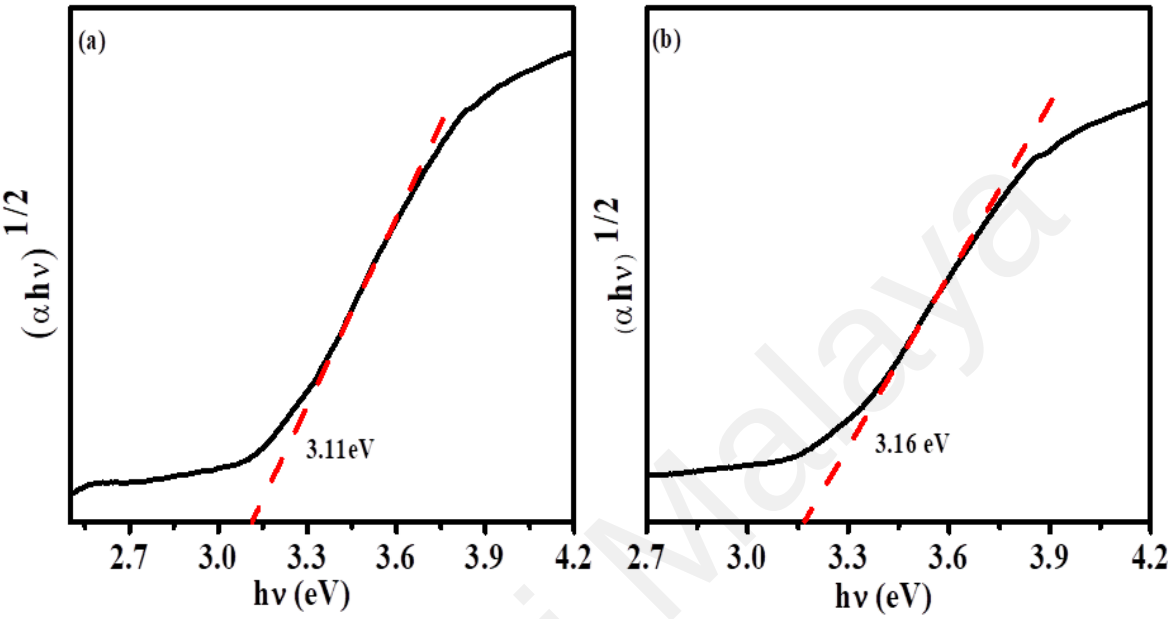

Figure 4.36: UV absorption spectra and calculated band gap of (a) TCF-F1 and (b) CF-F3

4.3.3.6 Photocatalytic degradation of ONP

The photocatalytic activity of TCF-F1 and TCF-F3 in comparison to TCF2 was then assessed by the degradation of ONP for 180 minutes under visible light irradiation. The results of the degradation are presented in Figure 4.37. It is obvious from the results that the concentrations of Fe_3O_4 greatly affect the overall photocatalytic performance of the composite system. At lower concentration of Fe_3O_4 (TCF-F1), 87% of ONP degradation was achieved within 180 min. However, at higher Fe_3O_4 concentration (TCF-F3) give only 72% degradation efficiency under the same experimental conditions. As evident from PL and UV-DR results, TCF2 has a small PL intensity and reduced band gap compared to TCF-F1 and TCF-F3 due to its larger crystallite size, hence it shows a better catalytic performance for ONP degradation.

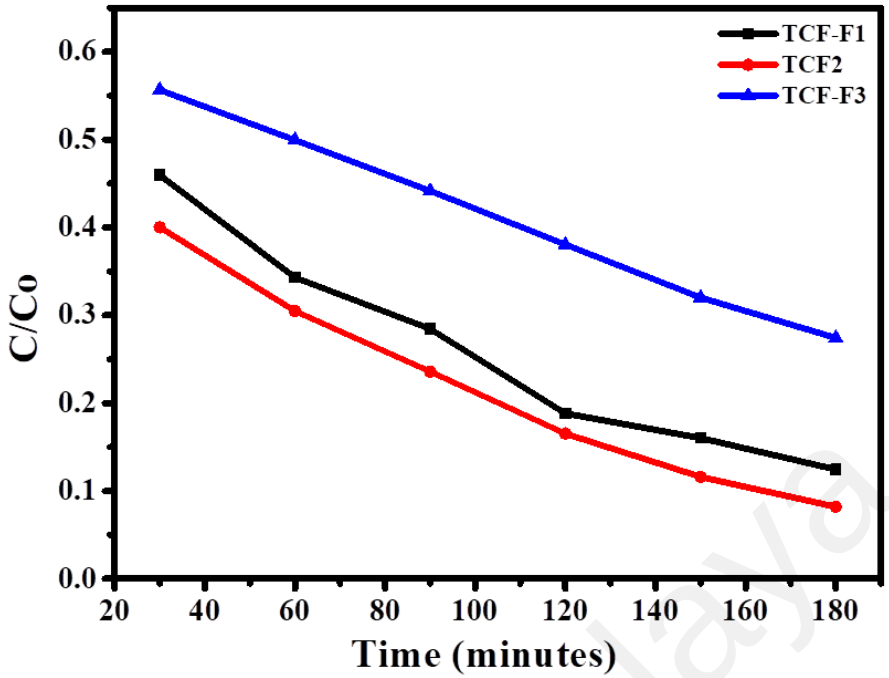

Figure 4.37: Photocatalytic activity of composites samples synthesized on varying concentration of Fe_3O_4 for ONP degradation.

Figure 4.38 shows the photocatalytic degradation kinetics of ONP with TCF-F1, TCF-F3 in comparison to TCF2. The degradation of ONP by all these three composites follows first order kinetic model (ln (Co/C) = kt) as evident from the linearity of the curves. Nearly straight lines are obtained from the concentration data of these three composite samples. The experimental data fitting to first order kinetics indicated that high degradation rates were observed for TCF2 as tabulated in Table 4.14. Hence, the highest photocatalytic degradation efficiency among TCF-F1, TCF2 and TCF-F3 was observed to be with TCF2. This enhanced photocatalytic activity is due to improved optical properties of TCF2 as it possesses the larger crystallite size. This large crystallite size facilitates the lowering of PL intensity and reduction of band gap. Therefore, TCF2 utilizes the solar spectrum more efficiently among all the composite samples. Hence, among all these three nanocomposites, the optimum concentration of Fe_3O_4 required in the synthesis of TCF composite system with improved optical properties and photocatalytic degradation activity was achieved in TCF2 composite.

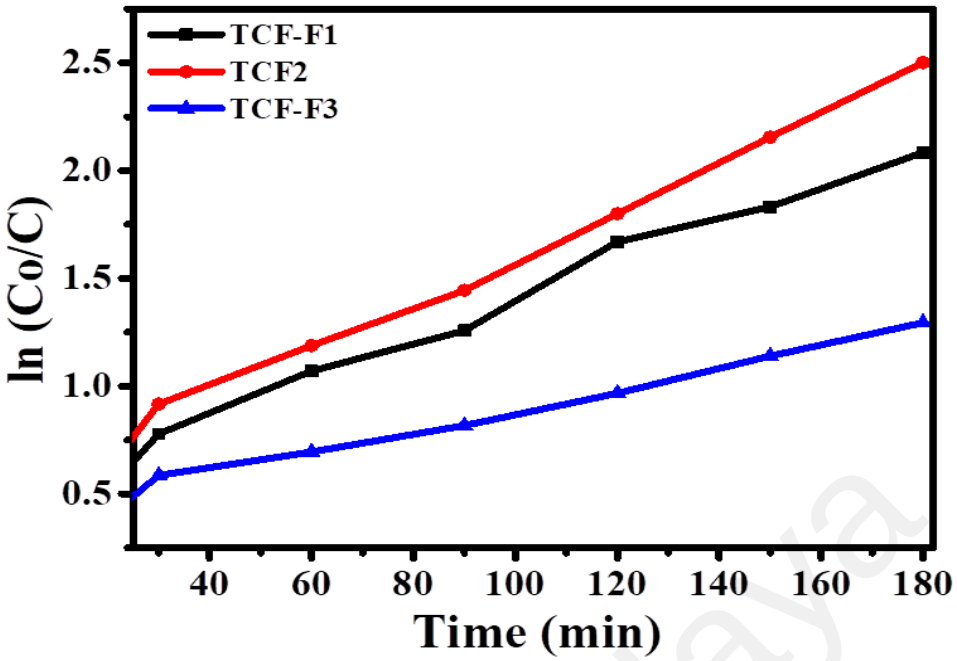

Figure 4.38: First order kinetics for the degradation of ONP by TCF nanocomposites synthesized on different concentrations of Fe_3O_4.

Table 4.14: Rate constants for the degradation of ONP by TCF nanocomposites synthesized on different concentrations of Fe_3O_4

Samples	Rate constant (K)	R^2
TCF-F1	0.0107	0.9121
TCF2	0.0139	0.9954
TCF-F3	0.0072	0.9931

4.4 Effect of operating parameters on photocatalytic degradation of ONP

The combination effects of operating parameters on the degradation rate of ONP were studied using CCD, which is widely used optimization technique because of its advantage in optimizing multifactor with a minimum number of experimental runs (Asghar et al., 2014). The combination effects of three operation parameters, namely catalyst (TCF2) dosage, ONP concentration and initial solution pH that yield optimum degradation rate of ONP were investigated. Other factors such as temperature, light intensity and oxygen supply were held constant. The ranges and levels of the operational parameter are tabulated in Table 4.15.

Table 4.15: Experimental ranges and levels of independent variables for photocatalytic degradation of ONP

Parameter	Unit	Symbol	Range		
			-1	0	+1
Catalyst loading	g	A	0.02	0.03	0.04
Initial concentration of Pollutant (ONP)	ppm	B	30	4	50
pH		C	3	6	9

A total of 20 runs with 8 factorial, 6 axial and 6 center points were suggested by the Design Expert software to optimize the degradation percentage of ONP as illustrated in Table 4.16.

Table 4.16: Experimental design matrix and location of points on CCD surface

Std	Run	Catalyst loading (g)	Pollutant concentration (ppm)	pH	Design location
1	13	0.02	30	3	Factorial
2	19	0.04	30	3	Factorial
3	7	0.02	50	3	Factorial
4	5	0.04	50	3	Factorial
5	6	0.02	30	9	Factorial
6	9	0.04	30	9	Factorial
7	11	0.02	50	9	Factorial
8	18	0.04	50	9	Factorial
9	17	0.02	40	6	Axial
10	15	0.04	40	6	Axial
11	14	0.03	30	6	Axial
12	2	0.03	50	6	Axial
13	3	0.03	40	3	Axial
14	8	0.03	40	9	Axial
15	4	0.03	40	6	Center
16	1	0.03	40	6	Center
17	12	0.03	40	6	Center
18	16	0.03	40	6	Center
19	10	0.03	40	6	Center
20	20	0.03	40	6	Center

Based on the proposed model, the following quadratic equation was developed to predict the degradation response in terms of the independent variables and their interactions (Equation. 4.1).

$$Y= b_o + b_1x_1 + b_2x_2 + b_3x_3 + b_{11}x_1^2 + b_{22}x_2^2 + b_{33}x_3^2 + b_{12}x_1x_2 + b_{13}x_1x_3 + b_{23}x_2x_3 \quad \textbf{(4.1)}$$

where Y is the response variable (% degradation efficiency), b_o is constant, b_1, b_2 and b_3 are coefficient for linear effects, b_{11}, b_{22} and b_{33} are quadratic coefficient and b_{12}, b_{13}, b_{23} are interaction coefficients (Can et al., 2006) respectively.

4.5 Model results for photocatalytic degradation of ONP

4.5.1 Model fitting and analysis of variance (ANOVA)

The photocatalytic experiments were performed under different conditions according to experimental runs as proposed by CCD model. Based on the experimental results, a second-order polynomial equation was derived in terms of coded factors, showing the interactions between the proposed independent variables (Equation 4.2).

$$Y\ (\%) = 90.55 - 2.66*A + 0.15*B - 12.55*C + 1.32*A^2 - 1.34*B^2 - 18.62*C^2 + 3.37*A*B - 0.80*A*C - 3.65*B*C \quad \textbf{(4.2)}$$

Where Y is the percentage degradation of ONP, A, B and C are terms for the coded values of TCF2 composite dosage, initial concentration of ONP and pH of solution, respectively. The positive sign in front of the terms in Equation.4.2 indicates synergistic effect in enhancing the removal percentage of ONP whereas the negative sign indicates antagonistic effect.

The experimental values of photocatalytic degradation of ONP are presented in Table 4.17. It can be seen that the degradation efficiency ranges from 55.58% to 95.77% under different experimental conditions. This indicate that the studied factors have strong influence on the percentage degradation of ONP. The observed values are in agreement with the predicted values as presented in the Figure 4.39.

Table 4.17: Central composite design with predictive values and experimental results

Run	Experimental ranges			ONP degradation	
	TCF2 loading (g)	Initial concentration of ONP (ppm)	pH	Experimental (%)	Predicted (%)
1	0.02	30	3	86.70	85.89
2	0.04	30	3	74.79	75.43
3	0.02	50	3	84.26	86.75
4	0.04	50	3	91.26	89.77
5	0.02	30	9	68.84	69.69
6	0.04	30	9	59.14	56.02
7	0.02	50	9	57.21	55.94
8	0.04	50	9	55.58	55.76
9	0.02	40	6	95.77	94.52
10	0.04	40	6	85.43	89.21
11	0.03	30	6	86.62	89.06
12	0.03	50	6	89.26	89.36
13	0.03	40	3	85.30	84.48
14	0.03	40	9	56.02	59.38
15	0.03	40	6	93.28	90.55
16	0.03	40	6	94.05	90.55
17	0.03	40	6	90.38	90.55
18	0.03	40	6	90.62	90.55
19	0.03	40	6	91.00	90.55
20	0.03	40	6	89.02	90.55

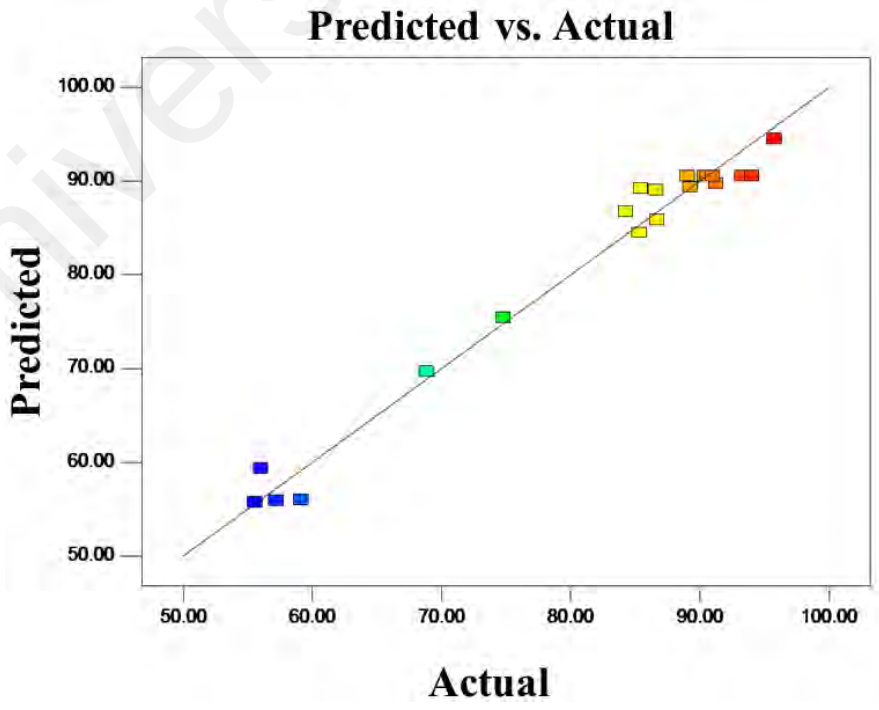

Figure 4.39: Predicted Vs Actual values for ONP degradation by TCF2

ANOVA is an integral part of the data analysis as the mathematical equation developed after fitting the function to the data may give misleading results and cannot explain the domain of the model adequately. Therefore, ANOVA is the more reliable way to evaluate the quality of the fitted model (Bezerra et al., 2008). The ANOVA for the degradation of ONP by TCF2 nanocomposite by evaluating the sum of square, degree of freedom, mean square, F-value and p-value and is tabulated in Table 4.18.

The model F-value of 51.52 implies the model is significant. There is only 0.01% chance that a "Model F-value" could occur due to noise. The quality of the developed model is high, as indicated by its R^2 value of 0.9789. This suggested that 97.89% of the variations for the degradation of ONP were explained by the independent variables within the studied range (Mun et al., 2015b). The lack of fit value is important criteria in describing the variation around the fitted model. In this case, the value of 3.31 shows the lack of fit is not significant relative to pure error when p value is 0.1077 (more than 0.05). The non-significant lack of fit shows good predictability of the model. Meanwhile, the significance of the model terms is proven by the small p-value (less than 0.0001). The coefficient of variation (C.V=3.43) is low, indicating high precision and good reliability of the experimental values. Adequate precision measures the signal to noise ratio (Mun., et al., 2015a). The adequate precision of 19.696, which is well above 4 indicates an adequate signal. Considering the ANOVA results, it can be concluded that model well explained the reaction and is a reliable approach to explain the findings of photocatalytic degradation of ONP.

Table 4.18: Analysis of variance (ANOVA) for derived quadratic model

Source	Sum of squares	DF	Mean square	F value	p-value	Remark
Model	3592.48	9	399.16	51.52	< 0.0001	Significant
A	70.67	1	70.67	9.12	0.0129	
B	0.22	1	0.22	0.029	0.8691	
C	1575.85	1	1575.85	203.41	< 0.0001	
A^2	4.78	1	4.78	0.62	0.4503	
B^2	4.95	1	4.95	0.64	0.4428	
C^2	953.36	1	953.36	123.06	< 0.0001	
AB	90.90	1	90.90	11.73	0.0065	
AC	5.14	1	5.14	0.66	0.4342	
BC	106.69	1	106.69	13.77	0.0040	
Residual	77.47	10	7.75			
Lack of fit	59.48	5	11.90	3.31	0.1077	Not significant
Pure error	17.99	5	3.60			
Core total	3669.95	19				
R^2	0.9789					
Adjusted R^2	0.9599					
Predicted R^2	0.8198					
C.V.	3.43					
Adeq Precision	19.696					

4.6 Response surface and 3D contour plots for the photocatalytic degradation of ONP

4.6.1 Effect of catalyst loading

Figure 4.24a shows the three-dimensional (3D) response surface of the influence of TCF2 loading and initial ONP concentration on the degradation efficiency of ONP. It is evident that the removal percentage of ONP was high at low catalyst loading (0.02g). The degradation efficiency slightly decreases by increasing TCF2 loading from 0.02 to 0.03g, and further decline by increasing TCF2 loading up to 0.04g. The negative effect of high TCF2 loading (0.04g) on the ONP degradation was due to the fact that high TCF2 loadings facilitate particle agglomeration, leading to a reduction in catalyst surface area and active sites available for light absorption and ONP adsorption, which in

turn, reduced the photocatalytic efficiency. Furthermore, the turbidity of the reaction mixture increased at higher catalyst loadings, which inhibit the penetration of light into the solution due to screening effect and hence hindered the generation of ˙OH on the catalyst surface. Thus, the overall photocatalytic activity decreases at high catalyst loading and optimum degradation efficiency was obtain at lower TCF2 loading (0.02g) (Liao & Wang, 2009). It can also be seen from the plots that with increasing ONP concentration, an increase in catalyst loading had a proportional effect on the degradation efficiency. Nevertheless, at low ONP concentration and high catalyst loading, a scavenging aspect of OH˙ was observed which caused a decrease in the overall photocatalytic performance (Asghar et al., 2017; Asghar et al., 2014).

4.6.2 Effect of initial ONP concentration

The effect of initial concentration of ONP was studied on its varying concentration from 30 to 50 mg/L under visible light irradiation. Photocatalytic degradation efficiency decreased with increasing initial concentration of ONP (Figure. 4.40a.). At higher concentration of ONP, large number of the ONP molecules adsorb onto the surface of TCF2 catalyst. This will make the approach of photons onto the TCF2 surface difficult hence the active sites on TCF2 surface will become inactivate. This will in turn retard the generation of OH˙, which are the main oxidant in photocatalytic reactions and consequently, the overall photocatalytic efficiency of the catalyst decreased. A much longer time needed to reach to the complete degradation process at higher pollutant (ONP) concentration. Furthermore, the intermediates formed during the degradation process will compete with ONP molecules for OH˙ at higher concentration of ONP, which decreased the degradation rate of ONP (Mun, et al., 2015b; Sin et al., 2012; Liao & Wang, 2009). Hence 30 mg/L of ONP concentration was considered as optimum for this study.

It can also be seen from the plots that there is an increase in degradation efficiency at high ONP concentration, with the increase in catalyst loading. The reason for this increasing trend is that the produced $OH^{\bullet}$ is reactive enough for ONP degradation at high values of catalyst loading and higher concentrations of $OH^{\bullet}$ is available to react with the high concentration of pollutant (ONP) (Asghar et al., 2017; Asghar et al., 2014).

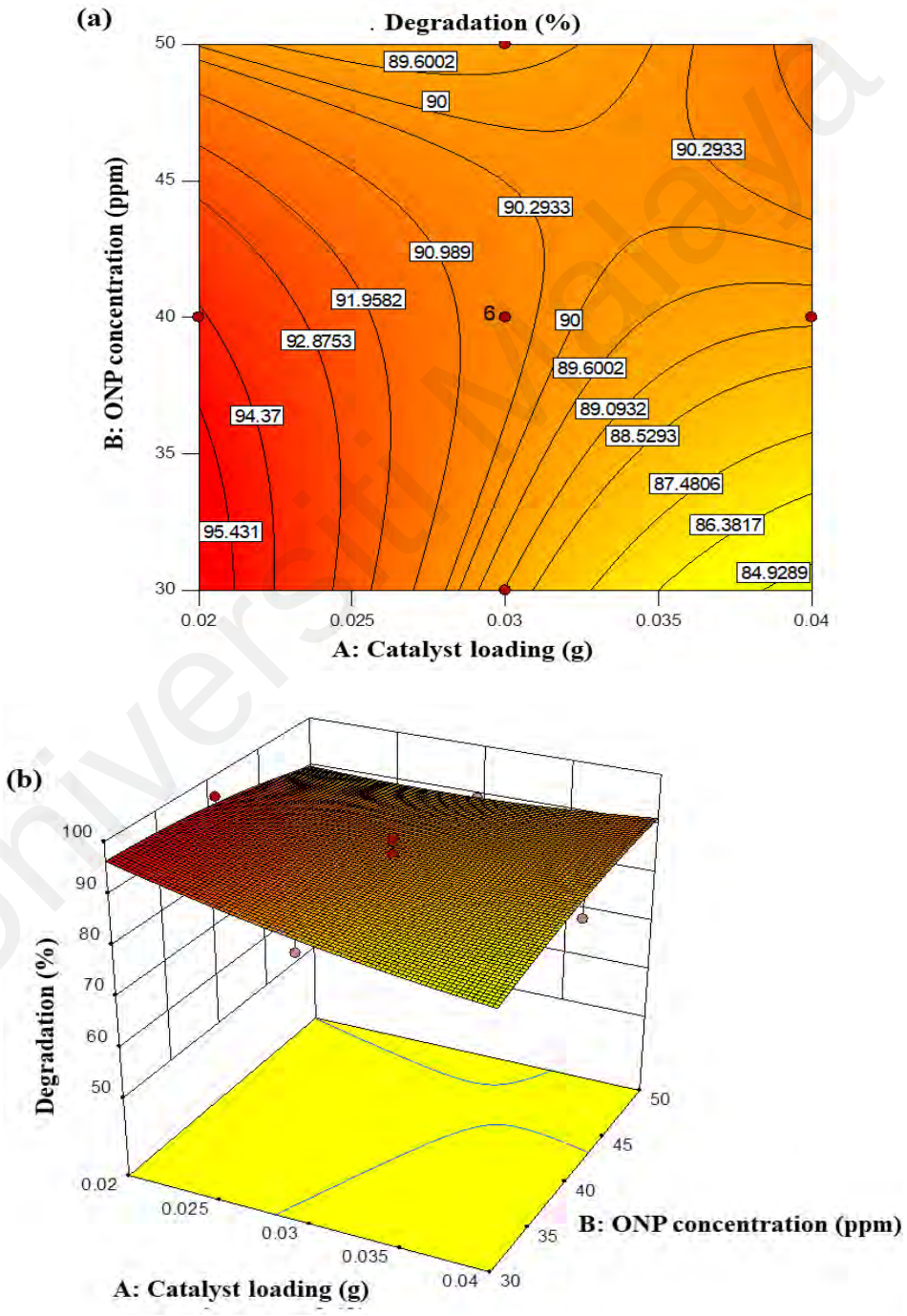

Figure 4.40: (a) 2D and (b) 3D contours for the degradation of ONP showing combined effects of catalyst (TCF2) loading and ONP concentration

4.6.3 Effect of pH

The pH of the reaction medium is an important criterion in controlling the photocatalytic degradation of ONP as surface properties of photocatalyst play an important role. The IEP of TiO_2 (P25) was reported to be approximately 6.2. In water, the surface of TiO_2 nanoparticles is generally covered by hydroxyl group as shown in Equation 4.1.

$$TiO_2 + H_2O \rightarrow Ti^{IV} - OH + H^+ + O_2 \quad \textbf{(4.1)}$$

It is found that when the pH is higher than pH_{pzc} (pH_{IEP}), the surface of TiO_2 is negatively charged and it is positively charged when pH is less than pH_{pzc} (pH_{IEP}) as expressed in Equations below.

$$Ti^{IV} - OH + OH^- \rightarrow Ti^{IV} - O^- + H_2O \ (pH > pH_{pzc}) \quad \textbf{(4.2)}$$

$$Ti^{IV} - OH + H^+ \rightarrow Ti^{IV} - OH_2^+ \ (pH < pH_{pzc}) \quad \textbf{(4.3)}$$

The interaction effects of TCF2 loadings and ONP concentration with pH of the reaction mixture is presented in Figure. 4.41b. From the response surface, it can be seen that the degradation of ONP increased as the pH reaches to an optimum value and at lower catalyst loading. Similarly, the interacting effects of pH and ONP concentration show that among these interacting effects, pH shows its significant role on the degradation of ONP (Figure 4.41c). The degradation efficiency of TCF2 was observed to be low at alkaline pH and at higher ONP concentration. As the concentration of $^{\bullet}OH$ at alkaline pH is high, it induces columbic repulsions with negatively surface charged TiO_2 and hence, reduces the rate of degradation. The rate of $^{\bullet}OH$ formation by TCF2 is also suppressed at alkaline pH (Mun et al., 2015b), which in turn reduced the degradation rate of ONP.

Another prospect of lower degradation rates under alkaline pH is that the ONP molecule becomes negatively charged by the deprotonation of its hydroxyl group. Thus the

possibility of being attacked by ˙OH is reduced which consequently reduced the overall degradation efficiency. The highest degradation rates are observed at pH 6, which is the optimum for the degradation of ONP by the nanocomposite.

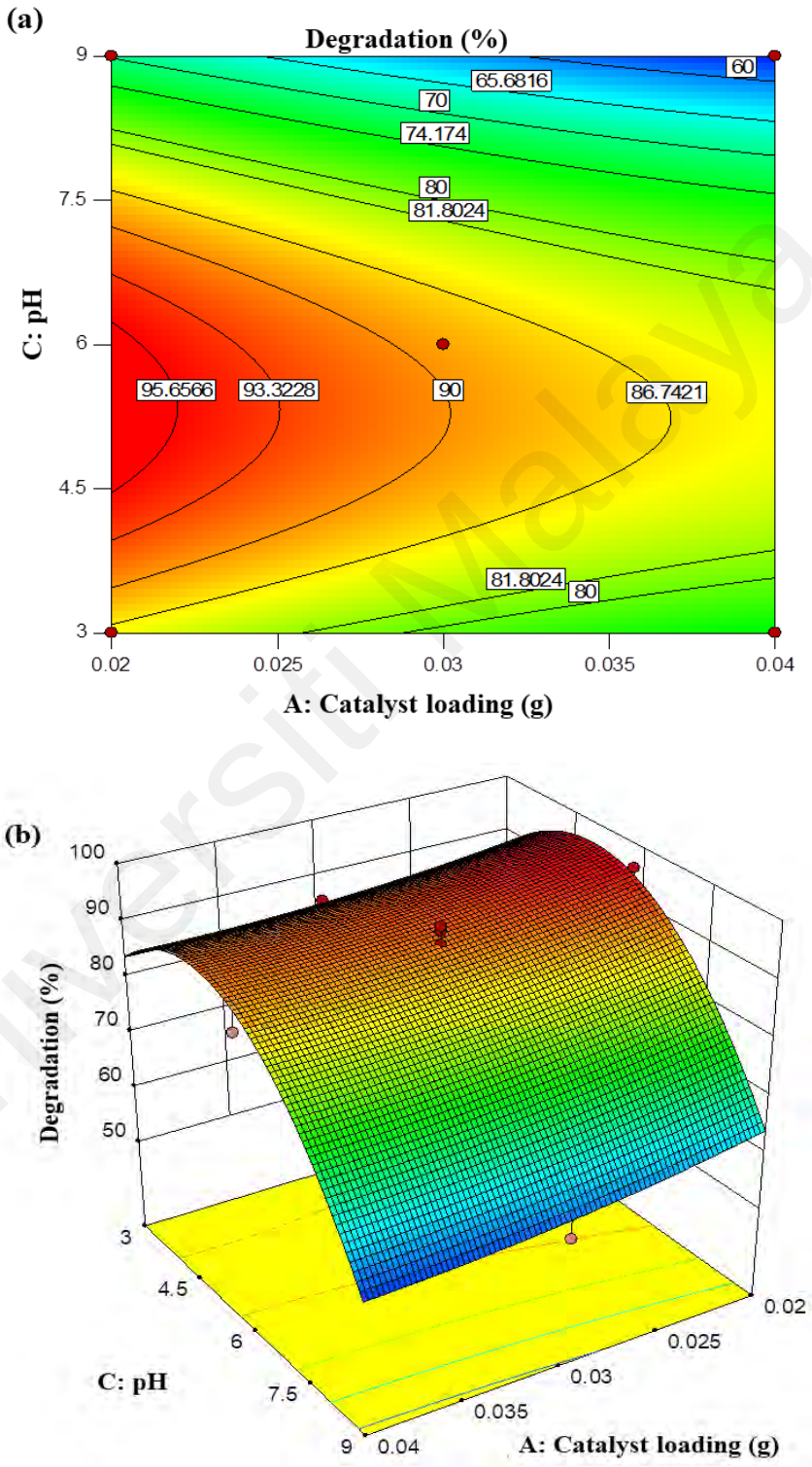

Figure 4.41: (a,c) 2D and (b,d) 3D contours for the degradation of ONP showing combined effects of catalyst (TCF2) loading and ONP concentration on pH respectively

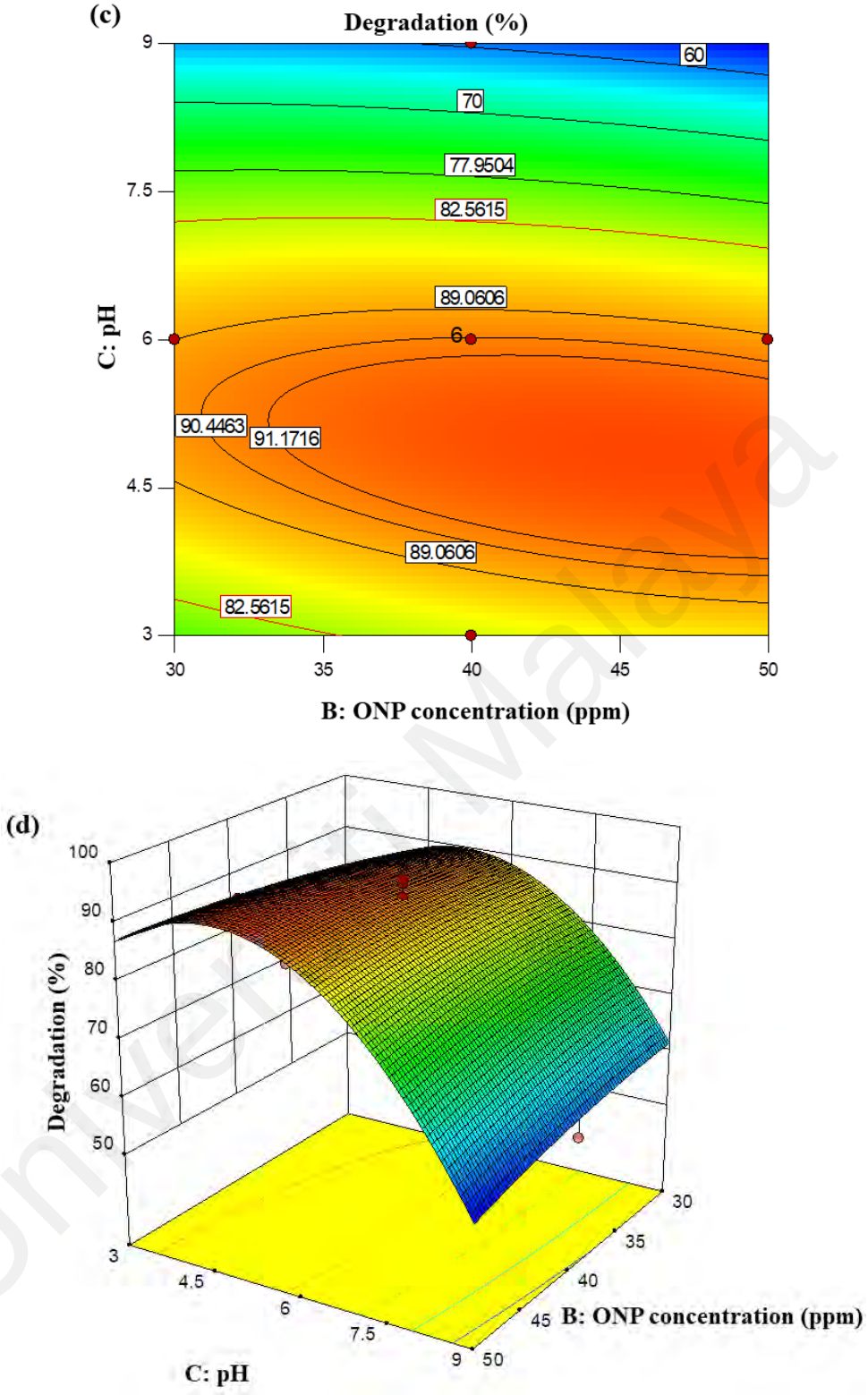

Figure 4.41: Continued

Figure 4.42 shows the perturbation plot for the ONP degradation. The perturbation plots compare the effects of all factors at a particular point in the design space. A steep slope or curvature in a factor shows that the response is sensitive to that factor. A relatively

flat line shows insensitivity to changes in that particular factor. In this case, the perturbation is plotted at the center point of the design space. From Figure 4.42, it can be seen that the ONP degradation is most sensitive to pH. The perturbations of catalyst loading (TCF2 concentration) and ONP concentration were slightly tilted, indicating that they also affect the overall degradation process.

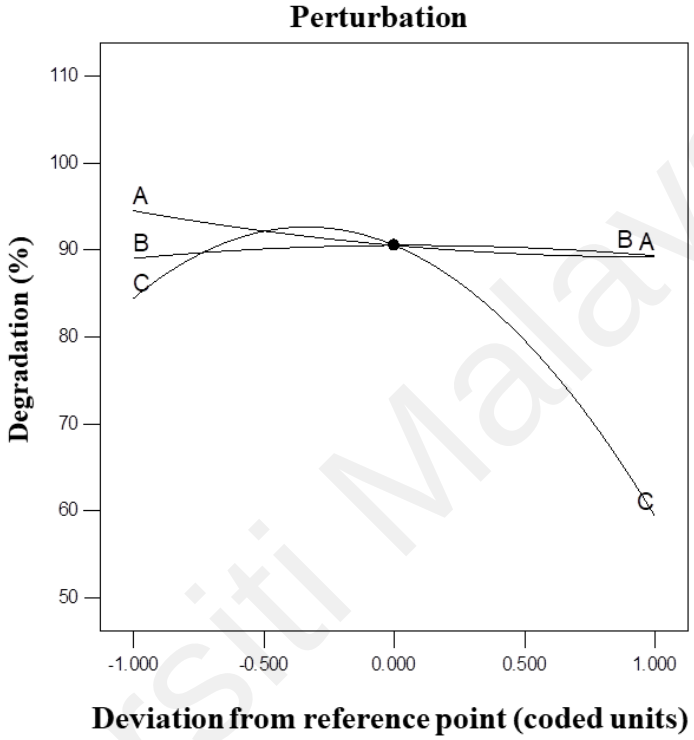

Figure 4.42: Perturbation plot for ONP degradation (a) catalyst loading, (b) ONP concentration and (c) pH.

4.7 Confirmation studies

The optimization of the experimental results was performed by keeping all responses in desired ranges in order to validate the developed RSM model. In the present studies, pH was targeted to (pH= 6) and other variables (catalyst loading and ONP concentration) were kept at minimum. Based on Table 4.19, three experimental runs were conducted to validate the optimized conditions. It can be seen that the degradation of ONP was 96.40% with 0.02g of TCF2 loading, 30 ppm initial concentration of ONP and solution pH of 6 under the predicted conditions. The experimental results of the degradation

showed 93.73%, which is very close to the predicted values (less than 2%). This indicates a good agreement between the experimental and predicted results under optimized conditions. Hence, it can be concluded that the CCD design based on RSM is a feasible and reliable approach to optimize the degradation of ONP.

Table 4.19: Experimental values for model verification conducted at predicted conditions from CCD

Number	A: Catalyst loading	B: ONP concentration	C: pH	Predicted values	Experimental values
1	0.02	30	6	96.41	93.73
2	0.02	30	6	96.41	92.37
3	0.02	30	6	96.34	92.02

4.8 Reusability of TCF nanocomposite

To evaluate the performance of the TCF2 nanocomposite for environmental applications, the reusability test was performed for four catalytic cycles and the results are presented in Figure 4.43. After the completion of degradation of ONP, the TCF2 nanocomposite sample was collected and utilized for the next cycle under the same experimental conditions. The reusability results indicated that after four consecutive runs, the removal of ONP by TCF2 composite sample still reached 89% within 180 min of visible light exposure, indicating that there is a slight reduction in the catalytic activity of the TC2 composite. The interactions between constituent elements in TCF2 are strong enough, which sustain its morphological and optical characteristics during the degradation process. Hence, the composite sample can be effectively utilized for the treatment of wastewater.

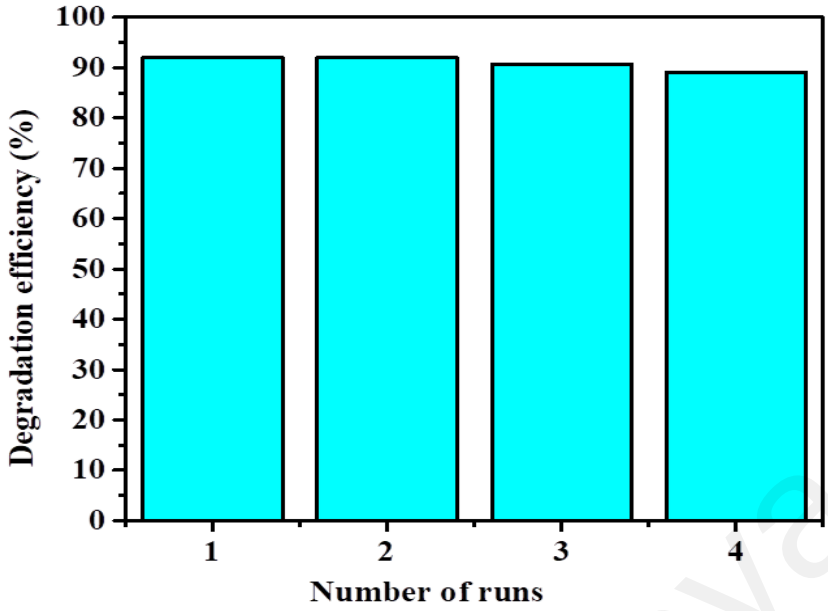

Figure 4.43: Reusability data over TCF2 nano composite in degradation of ONP in visible light

All the TCF2 composite samples utilized during four consecutive catalytic runs were collected and further investigated based on their magnetic properties to see if any loss in their magnetism occurs during the photocatalytic degradation process. It was observed that during the four catalytic runs, the Ms was still 19.24 emu/g and the decrease is only 2.14 emu/g from first run. This indicates that the loss of magnetism even after four successive runs is very little and the catalyst can be easily recycled after photocatalytic degradation process. The XRD patterns of TCF2 samples after four catalytic runs clearly indicate the presence of TiO_2 and Fe_3O_4 in the composite and the absence of any peaks in the range of 2θ angle of 20° to 30° which corresponds to maghemite verified the purity of Fe_3O_4 and durability of the composite (Appendix C). However slight decline in crystallinity after four successive runs might be due to loss of some TiO_2 coating from the composite surface which can be restored by repeating the coating of TiO_2.

The possible photodegradation mechanism of ONP by TCF2 nanocomposite proposed is illustrated in Figure 4.44. Under visible light, an electron was exited from the valence

band of TiO_2 to the CB creating e^-– h^+ pairs. This e^-– h^+ pairs undergo continuous charge transfer to the surface adsorbed pollutant molecules, causing its degradation into harmless species (CO_2 and H_2O). The catalyst can be recovered after photocatalytic process under the influence of magnetic field.

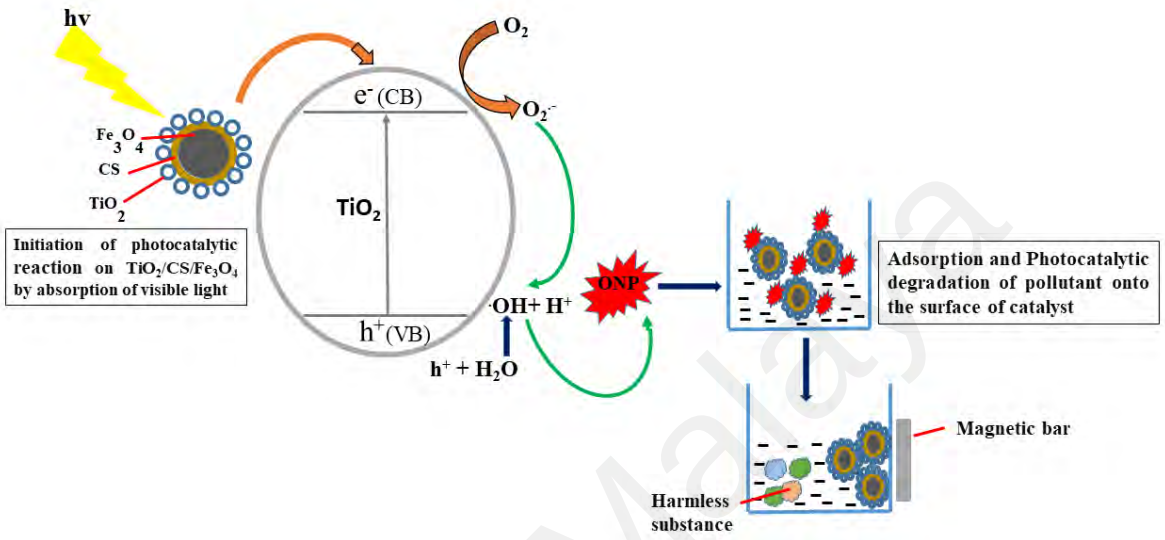

Figure 4.44: Schematic illustration of photocatalytic degradation of ONP by TiO_2/CS/Fe_3O_4 core-shell nanocomposite under visible light

4.9 Photocatalytic degradation intermediates and degradation pathway of ONP

The identification of the degraded products during photocatalytic degradation of ONP is of great interest as it provides information about the conversion of toxic pollutant in to variety of intermediates and ultimately, to the nontoxic end products. In the present work, the photodegradation pathway of ONP was analyzed using LC-MS and the reaction pathway was proposed. The LC-MS chromatograms of intermediate products from ONP degradation are shown in Appendix D.

During TiO_2 photocatalysis, different reactive species are produced namely, $OH^{\bullet}$, $O_2^{\bullet-}$ and H_2O_2 which are directly or indirectly responsible for the degradation of ONP. However, the $OH^{\bullet}$ is considered as the primary oxidant in the photocatalytic process. By referring to LC-MS analysis, two pathways are proposed based on the generated

intermediates, which are hydroxylation and denitration (Table 4.20). The intermediates IM1, IM2 and IM5 were observed in the first 30min of degradation. IM6 was appeared at 60 min, whereas, IM3 and IM4 were observed within 90 min. After 120 min no prominent peak observed except IM4 signal with very low intensity.

It was indicated that the first step in the degradation process is hydroxylation in which hydroxyl group addition occurs to the aromatic ring of ONP molecule. This hydroxyl group addition leads to the formation of IM1, IM2, IM3 and IM4. However, the de-nitration reaction was initiated at 60 min, with the loss of nitro group from the aromatic ring to form IM5 and IM6. Similar findings were also reported in the literature (Cañizares et al., 2004; Tijani et al., 2017) in which benzene derivatives such as phenol and hydroquinone as oxidation by-products during the degradation of NPs were identified. Moreover, the oxidation of IM6 would lead to the formation of carbonyl compounds and carboxylic acid because of ring cleavage, which further mineralized into CO_2 and H_2O.

Therefore, it is postulated that photodegradation of the ONP occurs in two steps: the first step is the fast step that destroys the aromatic group and, followed by second step that involves slow oxidation of the aliphatic chains. This consequence step indicates hydroxylation of the aromatic ring is the most important process where the addition of $OH^{\bullet}$ to the benzene ring produces dihydroxynitrobenzene isomers (IM1) (Figure 4.46). Similar observations were reported in literature for the degradation of NPs in which hydroxylation reaction is considered as the first step during degradation of ONP through advance oxidation technologies (Quiroz et al., 2014; Wei et al., 2011; Di Paola et al., 2003).The electrophilic attack of $OH^{\bullet}$ on the aromatic ring of ONP is activated by the presence of the two substituents: the phenolic –OH group (electron-donating) and $–NO_2$ group (electron-withdrawing). The electron-donating substituents increased the electron

density at the ortho and para positions, while the electron-withdrawing substituents are meta-directing. When both –OH and $–NO_2$ are present, the electrophilic attack ($OH^•$) will occur favorably in ortho and para positions with respect to the –OH group. In ONP, the $OH^•$ may enter in the ortho- and para- positions to form 3-nitrocatechol and nitrohydroquinone respectively (Fig 4.45)

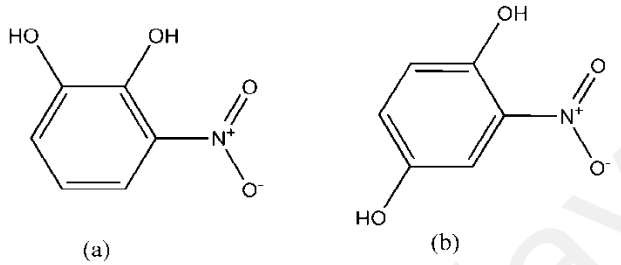

Figure 4.45: (a) 3-nitrocatechol (b) nitrohydroquinone

Table 4.20: Possible photocatalytic degradation intermediate products of ONP

Compounds	Molecular Formula	Actual Molecular weight (g/mol)	Observed Molecular weight (m/z) (g/mol)	Proposed pathway
ONP	$C_6H_5NO_2$	139.11	140	
IM1	$C_6H_5NO_4$	155.10	154.9	Hydroxylation
IM2	$C_6H_5O_3$	125.10	125	
IM3	$C_6H_5NO_5$	171.11	171	
IM4	$C_6H_3NO_4$	153.09	153	
IM5	$C_6H_6O_2$	110.11	109	Denitration
IM6	C_6H_5OH	94.11	93	

Previous literature also reported similar observations during the oxidative degradation of ONP by electro Fenton process (Ammar et al., 2007). The mineralization of ONP in water by applying Fenton and photo-Fenton process has also been studied in literature with the identification of nitrodihydroxylbenzene and nitro-p-benzoquinone as intermediate compounds (Kavitha & Palanivelu, 2005). Wei et al. (2011) carried out electrochemical oxidation of p-nitrophenol and identified tetra hydroxyl benzene as one of the intermediates. The carboxylic acids such as oxalic acid, acetic acid and malonic acid previously detected during photodegradation of ONP (Liu et al., 2008c; Ammar et

al., 2007; Kavitha & Palanivelu, 2005;), were not detected in this study. This might be attributed to a stronger competition between ONP and various intermediates for the free reactive species. Furthermore, some of the intermediates such as IM4 were resistant to further oxidation.

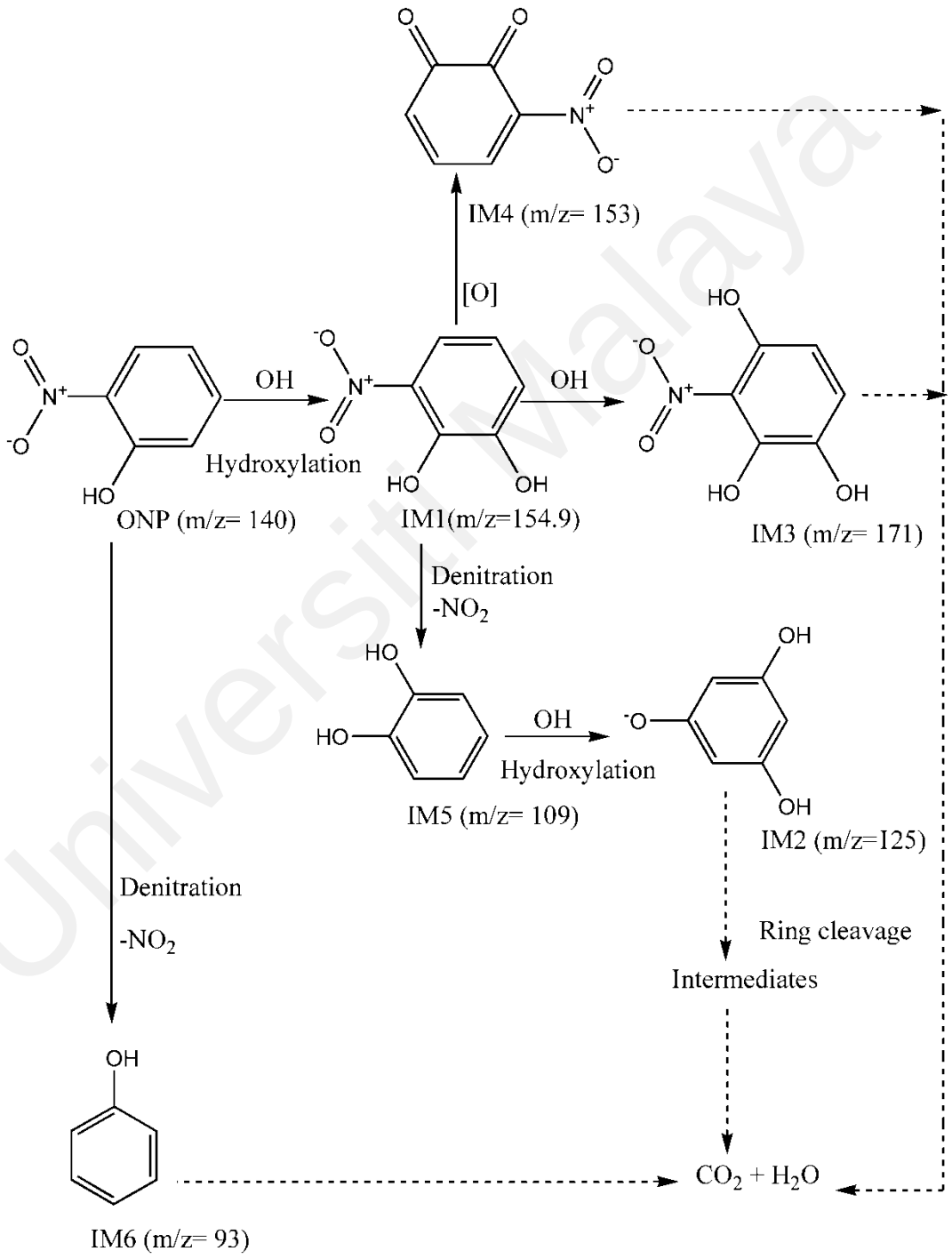

Figure 4.46: Proposed degradation pathway of ONP. Dotted arrows show undefined pathways

4.10 Mineralization of ONP

The total organic carbon (TOC) analysis is an important parameter to investigate the extent of mineralization of ONP, in addition to photodegradation. Figure 4.47 shows the removal percentage of TOC with respect to irradiation time. It was observed that TOC removal efficiency is directly proportional to irradiation time, with maximum removal efficiency of 81% after 180 min of visible light irradiation. This could be attributed to the hydrolysis and oxidation of ONP to the lower molecular weight compounds (Ammar et al., 2007). The photocatalytic degradation results show 92% of ONP degradation under the same experimental conditions. This indicated that some organic intermediates produced during ONP degradation were still present at the end of the photodegradation process. Similar finding was reported in literature for the mineralization of 2, 3 and 4-nitrophenol under sun light by W^{6+} impregnated ZnO (Hameed et al., 2014).

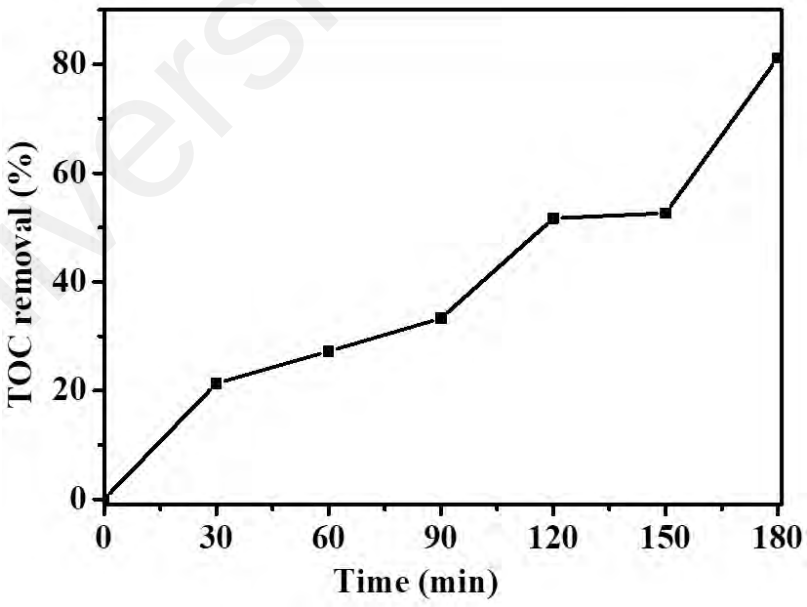

Figure 4.47: Percentage removal of TOC of ONP by TCF2 nanocomposite

CHAPTER 5: CONCLUSION AND FUTURE RECOMMENDATIONS

5.1 Conclusion

In this study, a ternary composite system, titania/chitosan/magnetite (TCF), was successfully synthesized and effectively utilized for the photocatalytic degradation of ONP. Degradation of ONP (92%) was achieved using minimum amount of catalyst (0.02 g) within 180 minutes of visible light irradiation. The inclusion of Fe_3O_4/CS with TiO_2 brought beneficial effects on the photocatalytic performance of TiO_2, such as improvement in adsorption properties, lowering the band gap energy and enhancement in charge separation. Additionally, the composite catalyst can be recycled after the photodegradation process by applying an external magnet.

The improved performance of TCF2 compared to bare TiO_2 can be related to its modification with Fe_3O_4/CS. As the band edge positions in TiO_2 and Fe_3O_4 are different in the composite, once the e^-– h^+ pairs are formed on TiO_2, the holes accumulate on the VB of TiO_2 because of a less positive band edge and the electrons accumulate near the CB of Fe_3O_4 because of the positive band edge. This improves the charge carrier separation. Similarly, the energy levels of iron in Fe_3O_4 are such that they are closer to the energy levels of TiO_2 conduction as well as VB. Therefore, they are capable of capturing both e^- and h^+ and hence, improve the charge separation. The presence of CS layer on Fe_3O_4 also facilitates charge separation as it behaves as an electron shuttle between TiO_2 and dioxygen molecule (produced during photocatalysis). This improvement in charge separation enhanced the overall photocatalytic performance of TCF composite compared to the bare TiO_2.

Fe_3O_4/CS played a remarkable role in shifting the activity of the composite to visible light region due to its positive influence on the optical properties of TiO_2, which

reduced the band gap in TCF2 (2.85 eV) compared to the bare TiO_2 (3.19 eV). Moreover, the composite can be recycled easily after photocatalytic process. This property is unique and make the composite system more advantegeous than the conventional catalytic systems, which may give a good photocatalytic performance but can not be recycled once the degradation process is done.

The optimization of the TCF composite was done by varying the concentration of TiO_2, CS and Fe_3O_4. The characterization and photocatalytic degradation results revealed that the optimum concentration of all these three components was achieved in TCF2, which has the smallest band gap (2.8 eV), lowest PL intensity and highest degradation rates (92%). An interesting observation from these results is that the optimum degradation results were obtained when TiO_2 and Fe_3O_4 content in the composite are almost in the same concentration. This occurs in TCF2. Similarly, the lower concentrations of Fe_3O_4 lowered the Ms and also affects on its optical properties.

CS behaved as a linker and support to prevent photodissolution of Fe_3O_4 and also improve the optical and photocatalytic properties of the composite. By increasing or decreasing CS concentration, enhancement in PL intensity, increased in crystallite size and broadening in band gaps were observed.

The optimized TCF2 composite was further investigated to assess the effect of operating parameters (catalyst loading, ONP concentration and pH) on ONP degradation rate using RSM. The highest degradation efficiency was observed at the lowest catalyst loading (0.02 g), pH 6 and minimal concentration of ONP (30 ppm) within 180 minutes of visible light exposure. It was found that degradation efficiency decreased with increasing TCF2 loading as high catalyst loading deactivate the catalyst surface area available for light absorption and adsorption of pollutant molecules. The

degradation rates were observed to be very low at alkaline pH because of the columbic repulsions between negatively charged TiO_2 surface and high concentration of OH.

The possible IMP during the degradation of ONP were analysed by using LC-MS. The nature of the intermediate compounds suggested that ONP degradation can be proceeded mainly via hydroxylation and denitration routes, where hydroxylation is the most prominent pathway with hydroxyl radical being the main oxidant in the photodegradation process.

5.2 Suggestions and Recommendations

The current study detailed extensively the properties of TCF composite system, however, a number of challenges still remain and need the attention of future work. The following suggestions for future studies can be deduced:

- The underlying mechanism of the enhancement of the photocatalytic performance of TCF2 needs further understanding to provide guidelines for photocatalytic treatment of wastewater in the future. This enhancement of photocatalytic performance may depend on the type of bonding between constituent elements, phase of TiO_2 and Fe_3O_4, surface properties and so forth.
- In this study, TiO_2-P25 were used and its modifications was done by Fe_3O_4/CS. However, the synthesis of composite based on the in-situ generation of TiO_2 nanoparticles along with Fe_3O_4/CS by using TiO_2 precursors can be a good suggestion.
- Optimization of TCF composite is done on the basis of concentration of each individual component (TiO_2, CS and Fe_3O_4) which can be extended by using other variables such as reaction temperature, pH and others.

- Three operating parameters namely catalyst loading, ONP concentration and pH were optimized to study the degradation rates. This can also be extended for other operating parameters such as irradiation time and the intensity of light.
- As CS possesses antimicrobial activity and iron oxide is commonly used in photo Fenton reactions, the scope of the applications of the designed composite system can be extended by combining it with other technologies including biological and electrodynamic.

5.3 Significance of Research

Most of the previous literature focus only on the photocatalytic degradation of ONP using catalysts such αBi_2O_3 (Hameed et al., 2015), ZnO (Assi et al., 2015), V_2O_5 (Aslam et al., 2015), CoO/CoS (Pouretedal & Kiyani, 2014), TiO_2-ionic liquid (Dai et al., 2014), Copper oxide Alumina (Atta et al., 2012), and TiO_2-P25 (Di Paola et al., 2003). Although these catalytic systems performed well and showed good photocatalytic activity, but the post treatment and recovery hurdle still persist. Thus, a photocatalytic system which combines the advantages of high photocatalytic efficiency in the visible light region and recycling after treatment is achieved in the present work. The effectiveness of the synthesized TCF2 nanocomposite has also been evaluated on a low concentration ONP (5ppm). The composite shows remarkable results, with 93% ONP degradation within 90 min of visible light irradiation.

REFERENCES

Abd Aziz, A., Harng Yau, Y., Li Puma, G., Fischer, C., Ibrahim, S., & Saravanan, P. (2014). Highly efficient magnetically separable TiO_2–graphene oxide supported $SrFe_{12}O_{19}$ for direct sunlight-driven photoactivity. *The Chemical Engineering Journal, 235*: 264-274.

Abdeen, Z. (2016). Adsorption efficiency of poly(ethylene glycol)/chitosan/CNT blends for maltene fraction separation. *Environmental Science and Pollution Research, 23*(11), 11240–11246.

Afzal, S., Samsudin, E. M., Mun, L. K., Julkapli, N. M., & Hamid, S. B. A. (2017). Room temperature synthesis of TiO_2 supported chitosan photocatalyst: Study on physicochemical and adsorption photo-decolorization properties. *Materials Research Bulletin, 86*: 24-29.

Ahmed, M., Parvatheeswara R, B., Venu, R., & Kim, C. (2014). Fe_3O_4/TiO_2 core/shell nanocubes: Single-batch surfactantless synthesis, characterization and efficient catalysts for methylene blue degradation. *Ceramics International, 40*(7), 11177-11186.

Ajmal, A., Majeed, I., Malik, R. N., Iqbal, M., Nadeem, M. A., Hussain, I., Yousaf, S., Zeshan., Mustafa, G., Zafar, M. I., & Nadeem, M. A. (2016). Photocatalytic degradation of textile dyes on Cu_2O-CuO/TiO_2 anatase powders. *Journal of Environmental Chemical Engineering, 4*(2), 2138-2146.

Ali, A., Hira Zafar, M. Z., ul Haq, I., Phull, A. R., Ali, J. S., & Hussain, A. (2016). Synthesis, characterization, applications, and challenges of iron oxide nanoparticles. *Nanotechnology, science and applications, 9*: 49-67.

Ali, I. (2012). New Generation Adsorbents for Water Treatment. *Chemical Reviews, 112*(10), 5073-5091.

Amir, M. N. I., N., Julkapli, N. M., Bagheri, S., & Yousefi, A. T. (2015). TiO_2 hybrid photocatalytic systems: impact of adsorption and photocatalytic performance. *Reviews in Inorganic Chemistry, 35*(3), 151-178.

Amir, N. I., Muhd Julkapli, N., & Hamid, S. B. A. (2017). Effective adsorption and photodegradation of methyl orange by TiO_2-chitosan supported glass plate photocatalysis. *Materials Technology, 32*(4), 256-264.

Ammar, S., Oturan, N., & Oturan, M. (2007). Electrochemical oxidation of 2-nitrophenol in aqueous medium by using electro-Fenton technology. *Journal of Environmental Engineering and Management, 17*: 89-96.

Anandan, S., Ikuma, Y., & Niwa, K. (2010). An Overview of Semi-Conductor Photocatalysis: Modification of TiO_2 Nanomaterials. *Solid State Phenomena, 162*: 239-260.

Ananpattarachai, J., Seraphin, S., & Kajitvichyanukul, P. (2016). Formation of hydroxyl radicals and kinetic study of 2-chlorophenol photocatalytic oxidation using C-doped TiO2, N-doped TiO2, and C,N Co-doped TiO_2 under visible light. *Environmental Science and Pollution Research, 23*(4), 3884-3896.

Aqil, A., El Kadib, A., Aqil, M., Bousmina, M., Elidrissi, A., Detrembleur, C., & Jerome, C. (2014). Nitroaldol condensation catalyzed by topologically modulable cooperative acid-base chitosan-TiO_2 hybrid materials. *RSC Advances, 4*(63), 33160-33163.

Arami-Niya, A., Wan Daud, W. M. A., S. Mjalli, F., Abnisa, F., & Shafeeyan, M. S. (2012). Production of microporous palm shell based activated carbon for methane adsorption: Modeling and optimization using response surface methodology. *Chemical Engineering Research and Design, 90*(6), 776-784.

Asghar, A., Abdul Raman, A. A., & Daud, W. M. A. W. (2014). A Comparison of Central Composite Design and Taguchi Method for Optimizing Fenton Process. *The Scientific World Journal,* 2014: 1-14.

Asghar, A., Raman, A. A. A., & Daud, W. M. A. W. (2017). In situ production of hydrogen peroxide in a microbial fuel cell for recalcitrant wastewater treatment. *Journal of Chemical Technology & Biotechnology, 92*(7), 1825-1840.

Aslam, M., Ismail, I. M. I., Salah, N., Chandrasekaran, S., Qamar, M. T., & Hameed, A. (2015). Evaluation of sunlight induced structural changes and their effect on the photocatalytic activity of V_2O_5 for the degradation of phenols. *Journal of Hazardous Materials, 286*: 127-135.

Assi, N., Mohammadi, A., Sadr Manuchehri, Q., & Walker, R. B. (2015). Synthesis and characterization of ZnO nanoparticle synthesized by a microwave-assisted combustion method and catalytic activity for the removal of ortho-nitrophenol. *Desalination and Water Treatment, 54*(7), 1939-1948.

Atta, A. Y., Jibril, B. Y., Al-Waheibi, T. K., & Al-Waheibi, Y. M. (2012). Microwave-enhanced catalytic degradation of 2-nitrophenol on alumina-supported copper oxides. *Catalysis Communications, 26*: 112-116.

Bae, H., Ahmad, T., Rhee, I., Chang, Y., Jin, S.-U., & Hong, S. (2012). Carbon-coated iron oxide nanoparticles as contrast agents in magnetic resonance imaging. *Nanoscale Research Letters, 7*(44), 1-5.

Banisharif, A., Elahi, S. H., Firooz, A. A., Khodadadi, A. A., & Mortazavi, Y. (2013). TiO_2/Fe_3O_4 Nanocomposite Photocatalysts for Enhanced Photo-Decolorization of Congo Red Dye. *International Journal of Nanoscience and Nanotechnology, 9*(4), 193-202.

Bezerra, M. A., Santelli, R. E., Oliveira, E. P., Villar, L. S., & Escaleira, L. A. (2008). Response surface methodology (RSM) as a tool for optimization in analytical chemistry. *Talanta, 76*(5), 965-977.

Byrne, J., Dunlop, P., Hamilton, J., Fernández-Ibáñez, P., Polo-López, I., Sharma, P., & Vennard, A. (2015). A Review of Heterogeneous Photocatalysis for Water and Surface Disinfection. *Molecules, 20*(4), 5574-5615.

Can, M. Y., Kaya, Y., & Algur, O. F. (2006). Response surface optimization of the removal of nickel from aqueous solution by cone biomass of Pinus sylvestris. *Bioresource Technology, 97*(14), 1761-1765.

Cañizares, P., Sáez, C., Lobato, J., & Rodrigo, M. A. (2004). Electrochemical treatment of 2,4-dinitrophenol aqueous wastes using boron-doped diamond anodes. *Electrochimica Acta, 49*(26), 4641-4650.

Chen, A., Zeng, G., Chen, G., Hu, X., Yan, M., Guan, S., . . & Xie, G. (2012). Novel thiourea-modified magnetic ion-imprinted chitosan/TiO_2 composite for simultaneous removal of cadmium and 2,4-dichlorophenol. *Chemical Engineering Journal, 191*: 85-94.

Chen, R., Han, J., Yan, X., Zou, C., Bian, J., Alyamani, A., & Gao, W. (2011). Photocatalytic activities of wet oxidation synthesized ZnO and ZnO–TiO_2 thick porous films. *Applied Nanoscience, 1*(1), 37-44.

Chen, W., Xiao, H., Xu, H., Ding, T., & Gu, Y. (2015). Photodegradation of Methylene Blue by TiO_2-Fe_3O_4-Bentonite Magnetic Nanocomposite. *International Journal of Photoenergy, 2015*: 1-7.

Cheng, J. P., Ma, R., Li, M., Wu, J. S., Liu, F., & Zhang, X. B. (2012). Anatase nanocrystals coating on silica-coated magnetite: Role of polyacrylic acid treatment and its photocatalytic properties. *Chemical Engineering Journal, 210*: 80-86.

Chiou, C.-H., Wu, C.-Y., & Juang, R.-S. (2008). Influence of operating parameters on photocatalytic degradation of phenol in UV/TiO_2 process. *Chemical Engineering Journal, 139*(2), 322-329.

Choi, W., Termin, A., & Hoffmann, M. R. (1994). The Role of Metal Ion Dopants in Quantum-Sized TiO2: Correlation between Photoreactivity and Charge Carrier Recombination Dynamics. *The Journal of Physical Chemistry, 98*(51), 13669-13679.

Chong, M. N., Jin, B., Chow, C. W. K., & Saint, C. (2010). Recent developments in photocatalytic water treatment technology: A review. *Water Research, 44*(10), 2997-3027.

Chowdhury, P., Moreira, J., Gomaa, H., & Ray, A. K. (2012). Visible-Solar-Light-Driven Photocatalytic Degradation of Phenol with Dye-Sensitized TiO_2: Parametric and Kinetic Study. *Industrial & Engineering Chemistry Research, 51*(12), 4523-4532.

Condon, J. B. (2006). *Surface Area and Porosity Determinations by Physisorption*. Amsterdam: Elsevier Science.

Daghrir, R., Drogui, P., & Robert, D. (2013). Modified TiO_2 For Environmental Photocatalytic Applications: A Review. *Industrial & Engineering Chemistry Research, 52*(10), 3581-3599.

Dahl, M., Liu, Y., & Yin, Y. (2014). Composite Titanium Dioxide Nanomaterials. *Chemical Reviews, 114*(19), 9853-9889.

Dai, J., He, R., Yuan, Y., Wang, W., & Fang, D. (2014). TiO_2 nanoparticles: low-temperature hydrothermal synthesis in ionic liquids/water and the photocatalytic degradation for o-nitrophenol. *Environmental Technology, 35*(2), 203-208.

Delmar, K., & Bianco-Peled, H. (2015). The dramatic effect of small pH changes on the properties of chitosan hydrogels crosslinked with genipin. *Carbohydrate Polymers, 12*: 28-37.

Di Paola, A., Augugliaro, V., Palmisano, L., Pantaleo, G., & Savinov, E. (2003). Heterogeneous photocatalytic degradation of nitrophenols. *Journal of Photochemistry and Photobiology A: Chemistry, 155*(1), 207-214.

Di Paola, A., Marcì, G., Palmisano, L., Schiavello, M., Uosaki, K., Ikeda, S., & Ohtani, B. (2002). Preparation of Polycrystalline TiO_2 Photocatalysts Impregnated with Various Transition Metal Ions: Characterization and Photocatalytic Activity for the Degradation of 4-Nitrophenol. *The Journal of Physical Chemistry B, 106*(3), 637-645.

Djebaili, K., Mekhalif, Z., Boumaza, A., & Djelloul, A. (2015). XPS, FTIR, EDX, and XRD Analysis of Al_2O_3 Scales Grown on PM2000 Alloy. *Journal of Spectroscopy, 2015*: 1-16.

Dong, H., Zeng, G., Tang, L., Fan, C., Zhang, C., He, X., & He, Y. (2015). An overview on limitations of TiO_2-based particles for photocatalytic degradation of organic pollutants and the corresponding countermeasures. *Water Research, 79*: 128-146.

Du, Y., Pei, M., He, Y., Yu, F., Guo, W., & Wang, L. (2014). Preparation, Characterization and Application of Magnetic Fe_3O_4-CS for the Adsorption of Orange I from Aqueous Solutions. *PLOS ONE, 9*(10), e108647.

Echavia, G. R. M., Matzusawa, F., & Negishi, N. (2009). Photocatalytic degradation of organophosphate and phosphonoglycine pesticides using TiO_2 immobilized on silica gel. *Chemosphere, 76*(5), 595-600.

Fagan, R., Mc Cormack, D. E., Dionysiou, D. D., & Pillai, S. C. (2016). A review of solar and visible light active TiO2 photocatalysis for treating bacteria, cyanotoxins and contaminants of emerging concern. *Materials Science in Semiconductor Processing, 42*: 2-14.

Faraji, M., Yamini, Y., & Rezaee, M. (2010). Magnetic nanoparticles: Synthesis, stabilization, functionalization, characterization, and applications. *Journal of the Iranian Chemical Society, 7*(1), 1-37.

Feilizadeh, M., Delparish, A., Bararpour, T., Abedini Najafabadi, H., Mohammad Esmaeil Zakeri, S., & Vossoughi, M. (2015). Photocatalytic removal of 2-nitrophenol using silver and sulfur co-doped TiO2 under natural solar light. *Water Science and Tachnology, 72*(3), 339-346.

Flores, A., Valenzuela, M., López, J., de la Luz, A. D., Muñoz, L., Méndez-Hernández, M., & Sosa-Sanchez, J. (2017). Synergetic Enhancement of the Photocatalytic Activity of TiO 2 with Visible Light by Sensitization Using a Novel Push-Pull Zinc Phthalocyanine. *International Journal of Photoenergy,* 2017: (1-9).

Fu, M. (2014). Preparation of core-shell structured Fe3O4/chitosan nanocomposite and its adsorption performance of Pb(II). *Journal of Chemical, Biological and Physical Sciences, 4*(4), 3025-3032.

Gaffour, H., & Mokhtari, M. (2016). Photocatalytic degradation of 4-nitrophenol using TiO2 + Fe2O3 and TiO2/Fe2O3-supported bentonite as heterogeneous catalysts. *Research on Chemical Intermediates, 42*(6), 6025-6038.

Gnanaprakasam, A., Sivakumar, V. M., & Thirumarimurugan, M. (2015). Influencing Parameters in the Photocatalytic Degradation of Organic Effluent via Nanometal Oxide Catalyst: A Review. *Indian Journal of Materials Science, 2015*: 1-16.

Govan, J., Gun, & ko, Y. (2014). Recent Advances in the Application of Magnetic Nanoparticles as a Support for Homogeneous Catalysts. *Nanomaterials, 4*(2), 222-241.

Gupta, S. M., & Tripathi, M. (2011). A review of TiO2 nanoparticles. *Chinese Science Bulletin, 56*(16), 1639-1657.

Gupta. P., & Ramrakhiani, M. (2009). Influence of the Particle Size on the Optical Properties of CdSe Nanoparticles. *The Open Nanoscience Journal, 3*: 15-19.

Gurkan, Y. Y., Kasapbasi, E., & Cinar, Z. (2013). Enhanced solar photocatalytic activity of TiO2 by selenium(IV) ion-doping: Characterization and DFT modeling of the surface. *Chemical Engineering Journal, 214*: 34-44.

Haldorai, Y., & Shim, J.-J. (2014). Novel chitosan-TiO2 nanohybrid: Preparation, characterization, antibacterial, and photocatalytic properties. *Polymer Composites, 35*(2), 327-333.

Hameed, A., Aslam, M., Ismail, I. M. I., Chandrasekaran, S., Kadi, M. W., & Gondal, M. A. (2014). Sunlight assisted photocatalytic mineralization of nitrophenol isomers over W6+ impregnated ZnO. *Applied Catalysis B: Environmental, 160-161*: 227-239.

Hameed, A., Aslam, M., Ismail, I. M. I., Salah, N., & Fornasiero, P. (2015). Sunlight induced formation of surface Bi2O4−x–Bi2O3 nanocomposite during the photocatalytic mineralization of 2-chloro and 2-nitrophenol. *Applied Catalysis B: Environmental, 163*: 444-451.

He, Q., Zhang, Z., Xiong, J., Xiong, Y., & Xiao, H. (2008). A novel biomaterial — Fe3O4:TiO2 core-shell nano particle with magnetic performance and high visible light photocatalytic activity. *Optical Materials, 31*(2), 380-384.

Hernández-Alonso, M. D., Fresno, F., Suárez, S., & Coronado, J. M. (2009). Development of alternative photocatalysts to TiO2: Challenges and opportunities. *Energy & Environmental Science, 2*(12), 1231-1257.

Herrmann, J. M. (1999). Heterogeneous photocatalysis: fundamentals and applications to the removal of various types of aqueous pollutants. *Catalysis Today, 53*: 115-129.

Hong, R. Y., Li, J. H., Zhang, S.-Z., Li, H.-Z., Zheng, Y., Ding, J.-m., & Wei, D. G. (2009). Preparation and characterization of silica-coated Fe3O4 nanoparticles used as precursor of ferrofluids. *Applied Surface Science, 255*(6), 3485-3492.

Hu, L., Wang, J., Zhang, J., Zhang, Q., & Liu, Z. (2014). An N-doped anatase/rutile TiO2 hybrid from low-temperature direct nitridization: enhanced photoactivity under UV-/visible-light. *RSC Advances, 4*(1), 420-427.

Hu, X., Yang, J., & Zhang, J. (2011). Magnetic loading of TiO2/SiO2/Fe3O4 nanoparticles on electrode surface for photoelectrocatalytic degradation of diclofenac. *Journal of Hazardous Materials, 196*: 220-227.

Huang, L., Yu, Y., Fu, C., Guo, H., & Li, X. (2017). Photocatalytic degradation of imidazolium ionic liquids using dye sensitized TiO2/SiO2 composites. *RSC Advances, 7*(51), 32120-32125.

Hui, C., Shen, C., Tian, J., Bao, L., Ding, H., Li, C., . . .Gao, H.-J. (2011). Core-shell Fe3O4@SiO2 nanoparticles synthesized with well-dispersed hydrophilic Fe3O4 seeds. *Nanoscale, 3*(2), 701-705.

Iida, H., Takayanagi, K., Nakanishi, T., & Osaka, T. (2007). Synthesis of Fe3O4 nanoparticles with various sizes and magnetic properties by controlled hydrolysis. *Journal of Colloid and Interface Science, 314*(1), 274-280.

Ilyas, H., Qazi, I. A., Asgar, W., Awan, M. A., & Khan, Z.-u.-d. (2011). Photocatalytic Degradation of Nitro and Chlorophenols Using Doped and Undoped Titanium Dioxide Nanoparticles. *Journal of Nanomaterials, 2011*: 1-8.

Ing, L. Y., Zin, N. M., Sarwar, A., & Katas, H. (2012). Antifungal Activity of Chitosan Nanoparticles and Correlation with Their Physical Properties. *International Journal of Biomaterials, 2012*: 1-9.

Ishiki, R. R., Mitsugu I. H., & Takashima, K. (2005). Photocatalytic degradation of imazethapyr herbicide at TiO2/H2O interface. *Chemosphere, 58*(10), 1461-1469.

Isley, S. L., & Penn, R. L. (2006). Relative Brookite and Anatase Content in Sol−Gel-Synthesized Titanium Dioxide Nanoparticles. *The Journal of Physical Chemistry B, 110*(31), 15134-15139.

Janczak, C. M., & Aspinwall, C. A. (2012). Composite nanoparticles: the best of two worlds. *Analytical and Bioanalytical Chemistry, 402*(1), 83-89.

Jin, Z., Duan, W., Duan, W., Liu, B., Chen, X., Yang, F., & Guo, J. (2016). Indium doped and carbon modified P25 nanocomposites with high visible-light sensitivity for the photocatalytic degradation of organic dyes. *Applied Catalysis A: General, 517*: 129-140.

Jingtao Dai, R. H., Yuan Yuan, Wei Wang & Dong Fang. (2014). TiO2 nanoparticles: low-temperature hydrothermal synthesis in ionic liquids/water and the photocatalytic degradation for o-nitrophenol. *Environmental Technology, 5*(2), 203-208.

Jinzhang, G., Lumei, P., Wu, Y., Jie, Y., & Yan, L. (2004). Oxidative Degradation of Nitrophenols in Aqueous Solution Induced by Plasma with Submersed Glow Discharge Electrolysis. *Plasma Processes and Polymers, 1*(2), 171-176.

Kabra, K., Chaudhary, R., & Sawhney, R. L. (2004). Treatment of Hazardous Organic and Inorganic Compounds through Aqueous-Phase Photocatalysis: A Review. *Industrial & Engineering Chemistry Research, 43*(24), 7683-7696.

Kalan, R. E., Yaparatne, S., Amirbahman, A., & Tripp, C. P. (2016). P25 titanium dioxide coated magnetic particles: Preparation, characterization and photocatalytic activity. *Applied Catalysis B: Environmental, 187*: 249-258.

Kamarulzaman, N., Kasim, M. F., & Chayed, N. F. (2016). Elucidation of the highest valence band and lowest conduction band shifts using XPS for ZnO and Zn0.99 Cu0.01O band gap changes. *Results in Physics, 6*: 217-230.

Kamarulzaman, N., Kasim, M. F., & Rusdi, R. (2015). Band Gap Narrowing and Widening of ZnO Nanostructures and Doped Materials. *Nanoscale Research Letters, 10*(1), 346-358.

Kang, K., Jang, M., Cui, M., Qiu, P., Park, B., Snyder, S. A., & Khim, J. (2014). Preparation and characterization of magnetic-core titanium dioxide: Implications for photocatalytic removal of ibuprofen. *Journal of Molecular Catalysis A: Chemical, 390*: 178-186.

Kaplan, D., Gong, Y., Mills, K., Swaminathan, V., Ajayan, P. M., Shirodkar, S., & Kaxiras, E. (2016). Excitation intensity dependence of photoluminescence from monolayers of MoS2 and WS2 /MoS2 heterostructures. *2D Materials, 3*(1), 015005.

Kavitha, V., & Palanivelu, K. (2005). Degradation of nitrophenols by Fenton and photo-Fenton processes. *Journal of Photochemistry and Photobiology A: Chemistry, 170*(1), 83-95.

Khan, M. M., Adil, S. F., & Al-Mayouf, A. (2015). Metal oxides as photocatalysts. *Journal of Saudi Chemical Society, 19*(5), 462-464.

Kharisov, B. I., Kharissova, O. V., & Ortiz-Mendez, U. (2015). *CRC Concise Encyclopedia of Nanotechnology*. Taylor and Francis Group.

Kim, W., Tachikawa, T., Majima, T., & Choi, W. (2009). Photocatalysis of Dye Sensitized TiO2 Nanoparticles with Thin Overcoat of Al2O3: Enhanced Activity for H2 Production and Dechlorination of CCl4. *The Journal of Physical Chemistry C, 113*(24), 10603-10609.

Koole, R., Groeneveld, E., Vanmaekelbergh, D., Meijerink, A., & de Mello Donegá, C. (2014). *Nanoparticles: Workhorses of Nanoscience*. Berlin, Heidelberg: Springer Berlin Heidelberg.

Krajewska, B. (2004). Application of chitin- and chitosan-based materials for enzyme immobilizations: a review. *Enzyme and Microbial Technology, 35*(2), 126-139.

Kumar, A., Guo, C., Sharma, G., Pathania, D., Naushad, M., Kalia, S., & Dhiman, P. (2016). Magnetically recoverable ZrO2/Fe3O4/chitosan nanomaterials for enhanced sunlight driven photoreduction of carcinogenic Cr(vi) and dechlorination & mineralization of 4-chlorophenol from simulated waste water. *RSC Advances, 6*(16), 13251-13263.

Kumar, K. S., Kumar, V. B., & Paik, P. (2013). Recent Advancement in Functional Core-Shell Nanoparticles of Polymers: Synthesis, Physical Properties, and Applications in Medical Biotechnology. *Journal of Nanoparticles, 2013*: 1-24.

Kumirska, J., Czerwicka, M., Kaczyński, Z., Bychowska, A., Brzozowski, K., Thöming, J., & Stepnowski, P. (2010). Application of Spectroscopic Methods for Structural Analysis of Chitin and Chitosan. *Marine Drugs, 8*(5), 1567-1636.

Kyzas, G., & Bikiaris, D. (2015). Recent Modifications of Chitosan for Adsorption Applications: A Critical and Systematic Review. *Marine Drugs, 13*(1), 312-337.

Lan, Y., Lu, Y., & Ren, Z. (2013). Mini review on photocatalysis of titanium dioxide nanoparticles and their solar applications. *Nano Energy, 2*(5), 1031-1045.

Lee, H.-G., Sai-Anand, G., Komathi, S., Gopalan, A.-I., Kang, S.-W., & Lee, K.-P. (2015a). Efficient visible-light-driven photocatalytic degradation of nitrophenol by using graphene-encapsulated TiO2 nanowires. *Journal of Hazardous Materials, 283*: 400-409.

Lee, J. S., Lee, E. J., & Hwang, H. J. (2012). Synthesis of Fe3O4-coated silica aerogel nanocomposites. *Transactions of Nonferrous Metals Society of China, 22*: 702-706.

Lee, M., Chen, B.-Y., & Den, W. (2015b). Chitosan as a Natural Polymer for Heterogeneous Catalysts Support: A Short Review on Its Applications. *Applied Sciences, 5*(4), 1272-1283.

Lee, S.-Y., & Park, S.-J. (2013). TiO2 photocatalyst for water treatment applications. *Journal of Industrial and Engineering Chemistry, 19*(6), 1761-1769.

Li, Q., Tang, G., Xiong, X., Cao, Y., Chen, L., Xu, F., & Tan, H. (2015). Carbon coated magnetite nanoparticles with improved water-dispersion and peroxidase-like activity for colorimetric sensing of glucose. *Sensors and Actuators B: Chemical, 215*: 86-92.

Li, Y., Sun, S., Ma, M., Ouyang, Y., & Yan, W. (2008). Kinetic study and model of the photocatalytic degradation of rhodamine B (RhB) by a TiO2-coated activated carbon catalyst: Effects of initial RhB content, light intensity and TiO2 content in the catalyst. *Chemical Engineering Journal, 142*(2), 147-155.

Li, Z.-D., Wang, H.-L., Wei, X.-N., Liu, X.-Y., Yang, Y.-F., & Jiang, W.-F. (2016). Preparation and photocatalytic performance of magnetic Fe3O4@TiO2 core–shell microspheres supported by silica aerogels from industrial fly ash. *Journal of Alloys and Compounds, 659*: 240-247.

Liao, W., & Wang, P. (2009). Microwave-assisted photocatalytic degradation of dimethyl phthalate using a microwave discharged electrodeless lamp. *Journal of the Brazilian Chemical Society, 20*(5), 866-872.

Lim, C., Ho Ryu, J., Kim, D. H., Cho, S. Y., & Oh, W. C. (2010). Reaction morphology and the effect of pH on the preparation of TiO2 nanoparticles by a sol-gel method. *Journal of Ceramic Processing Research,* 11(6),736-741.

Lin, Y., Geng, Z., Cai, H., Ma, L., Chen, J., Zeng, J.,. . .Wang, X. (2012). Ternary Graphene–TiO2–Fe3O4 Nanocomposite as a Recollectable Photocatalyst with Enhanced Durability. *European Journal of Inorganic Chemistry, 2012*(28), 4439-4444.

Liqiang, J., Yichun, Q., Baiqi, W., Shudan, L., Baojiang, J., Libin, Y.,. . . Jiazhong, S. (2006). Review of photoluminescence performance of nano-sized semiconductor materials and its relationships with photocatalytic activity. *Solar Energy Materials and Solar Cells, 90*(12), 1773-1787.

Liu, C., Tang, X., Mo, C., & Qiang, Z. (2008a). Characterization and activity of visible-light-driven TiO2 photocatalyst codoped with nitrogen and cerium. *Journal of Solid State Chemistry, 181*(4), 913-919.

Liu, R., Zhao, Y., Huang, R., Zhao, Y., & Zhou, A. H. (2010). Shape Evolution and Tunable Properties of Monodisperse Magnetite Crystals Synthesized by a Facile Surfactant-Free Hydrothermal Method. *European Journal of Inorganic Chemisty*, *2010*(28), 4499–4505.

Liu, W., Zhong. W., & Du. Y. W. (2008b). Magnetic Nanoparticles with Core/Shell Structures. *Journal of Nanoscience and Nanotechnology 8*(6), 2781–2792.

Liu, Y., Liu, H., & Li, Y. (2008c). Comparative study of the electrocatalytic oxidation and mechanism of nitrophenols at Bi-doped lead dioxide anodes. *Applied Catalysis B: Environmental, 84*(1), 297-302.

López, R., & Gómez, R. (2012). Band-gap energy estimation from diffuse reflectance measurements on sol–gel and commercial TiO2: a comparative study. *Journal of Sol-Gel Science and Technology, 61*(1), 1-7.

Lu, J., Deng, C., Zhang, X., & Yang, P. (2013). Synthesis of Fe3O4/Graphene/TiO2 Composites for the Highly Selective Enrichment of Phosphopeptides from Biological Samples. *ACS Applied Materials & Interfaces, 5*(15), 7330-7334.

Luan, Y., Feng, Y., Cui, H., Cao, Y., & Jing, L. (2014). Enhanced Photocatalytic Activity of P25 TiO2 after Modification with Phosphate-Treated Porous SiO2. *ChemPlusChem, 79*(9), 1271-1277.

Majidi, S., Sehrig, F. Z., Farkhani, S. M., Goloujeh, M. S., & Akbarzadeh, A. (2014). Current methods for synthesis of magnetic nanoparticles. *Artificial Cells, Nanomedicine, and Biotechnology*, *44*(2), 722-734.

Mansoor, M. A., Huang, N. M., McKee, V., Peiris, T. A. N., Wijayantha, K. G. U., Arifin, Z.,. . . Mazhar, M. (2015). Single phased MnZnO3 solid solution thin films for solar energy harvesting applications. *Solar Energy Materials and Solar Cells, 137*: 258-264.

Mansoori, G. A., Bastami, T. R., Ahmadpour, A., & Eshaghi, Z. (2008). *Annual Review of Nano Research (Volume 2),* Singapore ; Hackensack, N.J. : World Scientific Pub. Co.

Marbán Calzón, G., Valdés-Solís Iglesias, T., & Vu, T. T. (2014). High surface area stainless steel wire mesh-supported TiO2 prepared by sacrificial template accelerated hydrolysis. A monolithic photocatalyst superior to P25 TiO2. *Journal of Environmental Chemical Engineering, 2*: 2229-2235.

Memesa, M., Lenz, S., Emmerling, S. G. J., Nett, S., Perlich, J., Müller-Buschbaum, P., & Gutmann, J. S. (2011). Morphology and photoluminescence study of titania nanoparticles. *Colloid and Polymer Science, 289*(8), 943-953.

Michałowicz. J., Duda. W. (2007). Phenols – Sources and Toxicity. *Polish Journal of Environmental Studies, 16*(3), 347-362.

Mohamed S.A. Darwish, N. A. N., AlenaŠevcR, andIvanStibor. (2015). Functionalized Magnetic Nanoparticles and Their Effect on Escherichia coli and Staphylococcus aureus. *Journal of Nanomaterials, 2015*: 1-10.

Mohseni-Bandpi, A., Kakavandi, B., Kalantary, R. R., Azari, A., & Keramati, A. (2015). Development of a novel magnetite–chitosan composite for the removal of fluoride from drinking water: adsorption modeling and optimization. *RSC Advances, 5*(89), 73279-73289.

Morant C., Torres. R., Jimenez I., Sanz, J. M., & Elizalde, E. (2009). Characterization of nitrogen-doped carbon nanotubes by atomic force microscopy, X-ray photoelectron spectroscopy and X-ray absorption near edge spectroscopy. *J Nanosci Nanotechnol, 9*(6), 3633-3638.

Mun, L. K., Abd Hamid, S. B., & Lai, C. W. (2015a). Mechanism and Kinetics Study for Photocatalytic Oxidation Degradation: A Case Study for Phenoxyacetic Acid Organic Pollutant. *Journal of Nanomaterials, 2015*: 1-10.

Mun, L. K., Abdul Hamid, S. B., & Lai, C. W. (2015b). Multivariate analysis of photocatalytic-mineralization of Eriochrome Black T dye using ZnO catalyst and UV irradiation. *Materials Science in Semiconductor Processing, 39*: 40-48.

Mun, L. K., Lai, C. W., Ngai, K. S., & Juan, J. C. (2016). Recent developments of zinc oxide based photocatalyst in water treatment technology: A review. *Water Research, 88*: 428-448.

Nechita, P. (2017). Applications of Chitosan in Wastewater Treatment. *In Shalaby, E* (Eds). *Biological activities and applications of mrine polysaccharide*. London, United Kingdom. Intech Open Limited.

Nevim San, A. H., & glu, G. K., Zekiye Çınar. (2002). Photocatalytic degradation of 4-nitrophenol in aqueous TiO2 suspensions: Theoretical prediction of the intermediates. *Journal of Photochemistry and Photobiology A: Chemistry, 146*: 189-197.

Nguyen, V. C., Nguyen, N. L. G., & Pho, Q. H. (2015). Preparation of magnetic composite based on zinc oxide nanoparticles and chitosan as a photocatalyst for removal of reactive blue 198. *Advances in Natural Sciences: Nanoscience and Nanotechnology, 6*(3), 035001-035008.

Nie, C., Shao, N., Wang, B., Yuan, D., Sui, X., & Wu, H. (2016). Fully solar-driven thermo- and electrochemistry for advanced oxidation processes (STEP-AOPs) of 2-nitrophenol wastewater. *Chemosphere, 154*: 604-612.

Nithya, A., & Jothivenkatachalam, K. (2015). Chitosan assisted synthesis of ZnO nanoparticles: an efficient solar light driven photocatalyst and evaluation of antibacterial activity. *Journal of Materials Science: Materials in Electronics, 26*(12), 10207-10216.

Nithya, A., Jothivnkatachalam, K., Prabhu, S., & Kulandaivel, J. (2014). Chitosan Based Nanocomposite Materials as Photocatalyst – A Review. *Materials science forum, 781*: 79-94.

Ohno, T., Akiyoshi, M., Umebayashi, T., Asai, K., Mitsui, T., & Matsumura, M. (2004). Preparation of S-doped TiO2 photocatalysts and their photocatalytic activities under visible light. *Applied Catalysis A: General, 265*(1), 115-121.

Ozer, R. R., & Ferry, J. L. (2001). Investigation of the Photocatalytic Activity of TiO2−Polyoxometalate Systems. *Environmental Science & Technology, 35*(15), 3242-3246.

Pang, S. C., Kho, S. Y., & Chin, S. F. (2012). Fabrication of Magnetite/Silica/Titania Core-Shell Nanoparticles. *Journal of Nanomaterials, 2012*: 1-6.

Paola, A. D., Augugliaro, V,. .Palmisano, L,. Pantaleo, G., & Savinov, E. (2003). Heterogeneous photocatalytic degradation of nitrophenols. *Journal of Photochemistry and Photobiology A: Chemistry, 155*: 207-214.

Pasandideh, E. K., Kakavandi, B., Nasseri, S., Mahvi, A. H., Nabizadeh, R., Esrafili, A., & Kalantary, R. R. (2016). Silica-coated magnetite nanoparticles coreshell spheres (Fe_3O_4@SiO_2) for natural organic matter removal. *Journal of Environmental Health Science & Engineering, 14*(21), 1-13.

Pattanaik, P., & Sahoo, M. K. (2014). TiO2 photocatalysis: progress from fundamentals to modification technology. *Desalination and Water Treatment, 52*(34-36), 6567-6590.

Pelaez, M., Nolan, N. T., Pillai, S. C., Seery, M. K., Falaras, P., Kontos, A. G., Dunlop, P.S.M., Hamilton,J. W. J., Byrne, J. A., O'Shea, K., Entezari, M. H., Dionysiou, D. D. (2012). A review on the visible light active titanium dioxide photocatalysts for environmental applications. *Applied Catalysis B: Environmental, 125*: 331-349.

Pouretedal, H. R., & Kiyani, M. (2014). Photodegradation of 2-nitrophenol catalyzed by CoO, CoS and CoO/CoS nanoparticles. *Journal of the Iranian Chemical Society, 11*(1), 271-277.

Qourzal, S., Barka, N., Tamimi, M., Assabbane, A., Nounah, A., Ihlal, A., & Ait-Ichou, Y. (2009). Sol–gel synthesis of TiO2–SiO2 photocatalyst for β-naphthol photodegradation. *Materials Science and Engineering: C, 29*(5), 1616-1620.

Quiroz, M. A., Sánchez-Salas, J. L., Reyna, S., Bandala, E. R., Peralta-Hernández, J. M., & Martínez-Huitle, C. A. (2014). Degradation of 1-hydroxy-2,4-dinitrobenzene from aqueous solutions by electrochemical oxidation: Role of anodic material. *Journal of Hazardous Materials, 268*: 6-13.

Qureshi, A. L., Mahessar, A. A., Leghari, M. E., Lashari, B. K., & Mari, F. M. (2015). Impact of Releasing Wastewater of Sugar Industries into Drainage System of LBOD, Sindh, Pakistan. *International Journal of Environmental Science and Development, 6*(5), 381-386.

Reza, K. M., Kurny, A., & Gulshan, F. (2017). Parameters affecting the photocatalytic degradation of dyes using TiO2: a review. *Applied Water Science, 7*(4), 1569-1578.

Rockafellow, E. M., Stewart, L. K., & Jenks, W. S. (2009). Is sulfur-doped TiO2 an effective visible light photocatalyst for remediation?, *Applied Catalysis B: Environmental, 91*(1), 554-562.

Samsudin, E. M., Abd Hamid, S. B., Juan, J. C., Basirun, W. J., Kandjani, A. E., & Bhargava, S. K. (2015a). Controlled nitrogen insertion in titanium dioxide for optimal photocatalytic degradation of atrazine. *RSC Advances, 5*(55), 44041-44052.

Samsudin, E. M., Hamid, S. B. A., Juan, J. C., & Basirun, W. J. (2015b). Influence of triblock copolymer (pluronic F127) on enhancing the physico-chemical properties and photocatalytic response of mesoporous TiO2. *Applied Surface Science, 355*: 959-968.

Samsudin, E. M., Hamid, S. B. A., Juan, J. C., Basirun, W. J., & Kandjani, A. E. (2015c). Surface modification of mixed-phase hydrogenated TiO2 and corresponding photocatalytic response. *Applied Surface Science, 359*: 883-896.

Samsudin, E. M., Hamid, S. B. A., Juan, J. C., Basirun, W. J., Kandjani, A. E., & Bhargava, S. K. (2016). Effective role of trifluoroacetic acid (TFA) to enhance the photocatalytic activity of F-doped TiO2 prepared by modified sol–gel method. *Applied Surface Science, 365*: 57-68.

San, N., Hatipoğlu, A., Koçtürk, G., & Çınar, Z. (2002). Photocatalytic degradation of 4-nitrophenol in aqueous TiO2 suspensions: Theoretical prediction of the intermediates. *Journal of Photochemistry and Photobiology A: Chemistry, 146*(3), 189-197.

Saravanan, R., Aviles, J., Gracia, F., Mosquera, E., & Gupta, V. K. (2018). Crystallinity and lowering band gap induced visible light photocatalytic activity of TiO2/CS (Chitosan) nanocomposites. *International Journal of Biological Macromolecules, 109*: 1239-1245.

Satheesh, B., Tshai, K. Y., & Warrior, N. A. (2014). Effect of Chitosan Loading on the Morphological, Thermal, and Mechanical Properties of Diglycidyl Ether of Bisphenol A/Hexamethylenediamine Epoxy System. *Journal of Composites, 2014*: 1-8.

Shaker, S., Zafarian, S., Shilpa Chakra, C., & Rao, K. (2013). Preparation and characterization of magnetite nanoparticles by Sol-Gel method for water treatment. *International Journal of Innovative Research in Science, Engineering and Technology, 2*(7), 2969-2973.

Shamar, J. M. (2013). Determination of Some Phenols in Tigris River by HPLC. *Ibn Al-Haitham Journal for Pure & Applied Science, 26*(1), 250-258.

Shang, J., Zhao, F., Zhu, T., & Li, J. (2011). Photocatalytic degradation of rhodamine B by dye-sensitized TiO2 under visible-light irradiation. *Science China Chemistry, 54*(1), 167-172.

Shirsath, D. S., & Shrivastava, V. S. (2015). Photocatalytic Removal of O- Nitro Phenol from Wastewater by Novel an Eco-friendly Magnetic Nanoadsorbent. *International Journal of Environmental Researcg, 9*(1), 363-372.

Shokri, A. (2015). Degradation of 2-nitrophenol from petrochemical wastewater by ozone. *Russian Journal of Applied Chemistry, 88*(12), 2038-2043.

Sin, J.-C., Lam, S.-M., Mohamed, A. R., & Lee, K.-T. (2012). Degrading Endocrine Disrupting Chemicals from Wastewater by TiO2 Photocatalysis: A Review. *International Journal of Photoenergy, 2012*: 1-23.

Sobana, N., & Swaminathan, M. (2007). The effect of operational parameters on the photocatalytic degradation of acid red 18 by ZnO. *Separation and Purification Technology, 56*(1), 101-107.

Stefan, M., Pana, O., Leostean, C., Bele, C., Silipas, D., Senila, M., & Gautron, E. (2014). Synthesis and characterization of Fe3O4–TiO2 core-shell nanoparticles. *Journal of Applied Physics, 116*(11), 114312.

Stefan, M., Pana, O., Leostean, C., Bele, C., Silipas, D., Senila, M., & Gautron, E. (2014). Synthesis and characterization of Fe3O4–TiO2 core-shell nanoparticles. *Journal of Applied Physics, 116*(11), 1-10.

Stefanakis, A. I., & Thullner, M. (2016). Fate of Phenolic Compounds in Constructed Wetlands Treating Contaminated Water. In A. A. Ansari, S. S. Gill, R. Gill, G. R. Lanza & L. Newman (Eds.), *Phytoremediation: Management of Environmental Contaminants, Volume 4*. Cham: Springer International Publishing.

Sugiyama, T., Dabwan, A., Katsumata, H., Suzuki, T., & Knaeco, S. (2014). Optimization of Conditions for the Photocatalytic Degradation of EDTA in Aqueous Solution with Fe-Doped Titanium Dioxide. *Open Journal of Inorganic Non-Metallic Materials, 04*: 28-34.

Szymańska, E., & Winnicka, K. (2015). Stability of Chitosan—A Challenge for Pharmaceutical and Biomedical Applications. *Marine Drugs, 13*(4), 1819-1846.

Talat-Mehrabad, J., Khosravi, M., Modirshahla, N., & Behnajady, M. A. (2016). Sol-gel preparation and characterization of Ag and Mg co-doped nan TiO2:efficient photocatalytic degradation of C.I Acid Red 27. *Research on Chemical Iintermidiates,42*(2), 595-609.

Talebi, S., Chaibakhsh, N., & Moradi-Shoeili, Z. (2017). Application of nanoscale ZnS/TiO2 composite for optimized photocatalytic decolorization of a textile dye. *Journal of Applied Research and Technology, 15*(4), 378-385.

Tan, G. H., & Chong, C. L. (1993). Trace monitoring of water-borne phenolics in the Klang River Basin. *Environmental Monitoring and Assessment, 24*(3), 267-277.

Tayyebi, A., Outokesh, M., Moradi, S., & Doram, A. (2015). Synthesis and characterization of ultrasound assisted "graphene oxide–magnetite" hybrid, and investigation of its adsorption properties for Sr(II) and Co(II) ions. *Applied Surface Science, 353*: 350-362.

Teixeira, S., Mora, H., Blasse, L.-M., Martins, P. M., Carabineiro, S. A. C., Lanceros-Méndez, S., . . .Cuniberti, G. (2017). Photocatalytic degradation of recalcitrant micropollutants by reusable Fe3O4/SiO2/TiO2 particles. *Journal of Photochemistry and Photobiology A: Chemistry, 345*: 27-35.

Teng, X., Black, D., Watkins, N. J., Gao, Y., & Yang, H. (2003). Platinum-Maghemite Core−Shell Nanoparticles Using a Sequential Synthesis. *Nano Letters, 3*(2), 261-264.

Tijani, J. O., Mouele, M. E. S., Tottito, T. C., Fatoba, O. O., & Petrik, L. F. (2017). Degradation of 2-Nitrophenol by Dielectric Barrier Discharge System: The Influence of Carbon Doped TiO2 Photocatalyst Supported on Stainless Steel Mesh. *Plasma Chemistry and Plasma Processing, 37*(5), 1343-1373.

Tseng, D.-H., Juang, L.-C., & Huang, H.-H. (2012). Effect of Oxygen and Hydrogen Peroxide on the Photocatalytic Degradation of Monochlorobenzene in Aqueous Suspension. *International Journal of Photoenergy, 2012*: 1-9.

Tu, W., Zhou, Y., Liu, Q., Yan, S., Bao, S., Wang, X., . . . Zou, Z. (2013). An In Situ Simultaneous Reduction-Hydrolysis Technique for Fabrication of TiO2-Graphene 2D Sandwich-Like Hybrid Nanosheets: Graphene-Promoted Selectivity of Photocatalytic-Driven Hydrogenation and Coupling of CO2 into Methane and Ethane. *Advanced Functional Materials, 23*(14), 1743-1749.

Unsoy, G., Yalcin, S., Khodadust, R., Gunduz, G., & Gunduz, U. (2012). Synthesis optimization and characterization of chitosan-coated iron oxide nanoparticles produced for biomedical applications. *Journal of Nanoparticle Research, 14*(11), 964-968.

Vallack, H., J. Bakker, D., Brandt, I., Broström-Lundén, E., Brouwer, A., Bull, K., CGough, C., . . . Weavers, N, G. (1998). Controlling persistent organic pollutants—What next?. *Environmental Toxicology and Pharmacology, 6*: 143-175.

Vashist, S. K. (2013). Magnetic Nanoparticles-Based Biomedical and Bioanalytical Applications. *Journal of nanomedicine and nanotechnology, 4*(2), e130

Vuong Hoan, N. T., Anh Thu, N. T., Duc, H. V., Cuong, N. D., Quang Khieu, D., & Vo, V. (2016). Fe3O4/Reduced Graphene Oxide Nanocomposite: Synthesis and Its Application for Toxic Metal Ion Removal. *Journal of Chemistry, 2016*: 1-10.

Wang, D., Yang, J., Li, X., Wang, J., Zhai, H., Lang, J., & Song, H. (2017a). Effect of thickness and microstructure of TiO2 shell on photocatalytic performance of magnetic separable Fe3O4/SiO2/mTiO2 core-shell composites. *physica status solidi (a), 214*(3), 1-8.

Wang, G., Xu, L., Zhang, J., Yin, T., & Han, D. (2012). Enhanced Photocatalytic Activity of TiO2 Powders (P25) via Calcination Treatment. *International Journal of Photoenergy, 2012*: 1-9.

Wang, H., Wang, H.-L., Jiang, W.-F., & Li, Z.-Q. (2009a). Photocatalytic degradation of 2,4-dinitrophenol (DNP) by multi-walled carbon nanotubes (MWCNTs)/TiO2 composite in aqueous solution under solar irradiation. *Water Research, 43*(1), 204-210.

Wang, J., Chen, Y., Liu, G., & Cao, Y. (2017b). Synthesis, characterization and photocatalytic activity of inexpensive and non-toxic Fe2O3−Fe3O4 nano-composites supported by montmorillonite and modified by graphene. *Composites Part B: Engineering, 114*, 211-222.

Wang, K.-H., Hsieh, Y.-H., Chou, M.-Y., & Chang, C.-Y. (1999). Photocatalytic degradation of 2-chloro and 2-nitrophenol by titanium dioxide suspensions in aqueous solution. *Applied Catalysis B: Environmental, 21*(1), 1-8.

Wang, X., Liu, Y., & Zheng, J. (2016). Removal of As(III) and As(V) from water by chitosan and chitosan derivatives: a review. *Environmental Science and Pollution Research, 23*(14), 13789-13801.

Wang, Y., He, Y., Lai, Q., & Fan, M. (2014). Review of the progress in preparing nano TiO2: An important environmental engineering material. *Journal of Environmental Sciences, 26*(11), 2139-2177.

Wang, Y., Li, B., Zhou, Y., & Jia, D. (2009b). In Situ Mineralization of Magnetite Nanoparticles in Chitosan Hydrogel. *Nanoscale Research Letters, 4*(9), 1041-1046.

The United Nations World Water Development Report (WWDR). (2017). *Facts and Figures, Wastewater the untapped resource*. Colombella, Perugia, Italy.

Wei Wu, Z. W., Taekyung Yu, Changzhong Jiang and Woo-Sik Kim. (2015). Recent progress on magnetic iron oxide nanoparticles: synthesis, surface functional strategies and biomedical applications. *Science and Technology of Advanced Materials, 16*: 1-43.

Wei, H., Yang, W., Xi, Q., & Chen, X. (2012). Preparation of Fe3O4@graphene oxide core–shell magnetic particles for use in protein adsorption. *Materials Letters, 82*, 224-226.

Wei, L., Zhu, H., Mao, X., & Gan, F. (2011). Electrochemical oxidation process combined with UV photolysis for the mineralization of nitrophenol in saline wastewater. *Separation and Purification Technology, 77*(1), 18-25.

Wu, W., He, Q., & Jiang, C. (2008). Magnetic Iron Oxide Nanoparticles: Synthesis and Surface Functionalization Strategies. *Nanoscale Research Letters, 3*(11), 397-415.

Wulandari, I., Santjojo, D., Shobirin, R., & Sabarudin, A. (2017). Characteristics and magnetic properties of chitosan-coated Fe_3O_4 nanoparticles prepared by ex-situ co-precipitation method. *Rasayan Journal Of Chemistry, 10*(4), 1348-1358.

Xia, H., Wan, Y., Yuan, G., Fu, Y., & Wang, X. (2013). Fe3O4/carbon core–shell nanotubes as promising anode materials for lithium-ion batteries. *Journal of Power Sources, 241*, 486-493.

Xiao, L., Youji, L., Feitai, C., Peng, X., & Ming, L. (2017). Facile synthesis of mesoporous titanium dioxide doped by Ag-coated graphene with enhanced visible-light photocatalytic performance for methylene blue degradation. *RSC Advances, 7*(41), 25314-25324.

Xiao, W., Xu, J., Liu, X., Hu, Q., & Huang, J. (2013). Antibacterial hybrid materials fabricated by nanocoating of microfibril bundles of cellulose substance with titania/chitosan/silver-nanoparticle composite films. *Journal of Materials Chemistry B, 1*(28), 3477-3485.

Xin, T., Ma, M., Zhang, H., Gu, J., Wang, S., Liu, M., & Zhang, Q. (2014). A facile approach for the synthesis of magnetic separable Fe3O4@TiO_2, core–shell nanocomposites as highly recyclable photocatalysts. *Applied Surface Science*, *288*: 51-59.

Xing, B., Shi, C., Zhang, C., Yi, G., Chen, L., Guo, H., . . . Cao, J. (2016). Preparation of TiO2/Activated Carbon Composites for Photocatalytic Degradation of RhB under UV Light Irradiation. *Journal of Nanomaterials, 2016*: -1-0.

Yan, Y., Hao, B., & Chen, G. (2011). Biomimetic synthesis of titania with chitosan-mediated phase transformation at room temperature. *Journal of Materials Chemistry, 21*(29), 10755-10760.

Yang, D., Li, J., Jiang, Z., Lu, L., & Chen, X. (2009). Chitosan/TiO2 nanocomposite pervaporation membranes for ethanol dehydration. *Chemical Engineering Science, 64*(13), 3130-3137.

Yang, Y., Xu, L., Wang, H., Wang, W., & Zhang, L. (2016). TiO2/graphene porous composite and its photocatalytic degradation of methylene blue. *Materials & Design, 108*: 632-639.

Yao, H., Fan, M., Wang, Y., Luo, G., & Fei, W. (2015). Magnetic titanium dioxide based nanomaterials: synthesis, characteristics, and photocatalytic application in pollutant degradation. *Journal of Materials Chemistry A, 3*(34), 17511-17524.

Yenchalwar, S. G., Azhagan, V. K., & Shelke, M. V. (2014). Enhanced photoluminescence and photoactivity of plasmon sensitized nSiNWs/TiO2 heterostructures. *Physical Chemistry Chemical Physics, 16*(33), 17786-17791.

Yoo, J. B., Yoo, H. J., Jung, H. J., Kim, H. S., Bang, S., Choi, J., . . . Hur, N. H. (2016). Titanium oxynitride microspheres with the rock-salt structure for use as visible-light photocatalysts. *Journal of Materials Chemistry A, 4*(3), 869-876.

Yoon, Y., Park, W. K., Hwang, T.-M., Yoon, D. H., Yang, W. S., & Kang, J.-W. (2016). Comparative evaluation of magnetite–graphene oxide and magnetite-reduced graphene oxide composite for As(III) and As(V) removal. *Journal of Hazardous Materials, 304*: 196-204.

Yu, Y., Yu, J. C., Chan, C.-Y., Che, Y.-K., Zhao, J.-C., Ding, L., . . . Wong, P.-K. (2005). Enhancement of adsorption and photocatalytic activity of TiO2 by using carbon nanotubes for the treatment of azo dye. *Applied Catalysis B: Environmental, 61*(1), 1-11.

Yuan Liu, H. L., & , Y. L. (2008). Comparative study of the electrocatalytic oxidation and mechanism of nitrophenols at Bi-doped lead dioxide anodes. *Applied Catalysis B: Environmental, 84*: 297-302.

Zainal, Z., Hui, L. K., Hussein, M. Z., Abdullah, A. H., & Hamadneh, I. R. (2009). Characterization of TiO2–Chitosan/Glass photocatalyst for the removal of a monoazo dye via photodegradation–adsorption process. *Journal of Hazardous Materials, 164*(1), 138-145.

Zha, R., Nadimicherla, R., & Guo, X. (2015). Ultraviolet photocatalytic degradation of methyl orange by nanostructured TiO2/ZnO heterojunctions. *Journal of Materials Chemistry A, 3*(12), 6565-6574.

Zhang, C., Chen, H., Ma, M., & Yang, Z. (2015). Facile synthesis of magnetically recoverable Fe3O4/Al2O3/molecularly imprinted TiO2 nanocomposites and its molecular recognitive photocatalytic degradation of target contaminant. *Journal of Molecular Catalysis A: Chemical, 402*: 10-16.

Zhang, L., Wu, X., Zheng, T., & Ju, M. (2013). Green nanotechnology: aqueous photocatalytic degradation of persistent organic pollutants using nanostructured materials. *Nanotechnology and Precision Engineering, 11*: 511-517.

Zhang, X., Zhao, X., & Su, H. (2011). Degradation characteristic of TiO2-chitosan adsorbent on Rhodamine B and purification of industrial wastewater. *Korean Journal of Chemical Engineering, 28*(5), 1241-1246.

Zhao, B., Mele, G., Pio, L., Li, J., Palmisano, L., & Vasapollo, G. (2010). Degradation of 4-nitrophenol (4-NP) using Fe–TiO2 as a heterogeneous photo-Fenton catalyst. *Journal of Hazardous Materials, 176*(1), 569-574.

Zheng, Y.-h., Cheng, Y., Bao, F., & Wang, Y.-s. (2006). Synthesis and magnetic properties of Fe_3O_4 nanoparticles. *Materials Research Bulletin, 41*(3), 525-529.